Author:
Alevropoulos-Borrill, Alanna

Title:
Exploring the Suitability of the CMIP5 Ensemble for Forcing the BISICLES Ice Sheet Model in the Amundsen Sea, West Antarctica

Exploring the Suitability of the CMIP5 Ensemble for Forcing the BISICLES Ice Sheet Model in the Amundsen Sea, West Antarctica

Alanna Vanessa Alevropoulos-Borrill

A dissertation submitted to the University of Bristol in accordance with the requirements for award of the degree of Master of Science (by research) in the Faculty of Science.

Geographical Sciences

November 2018

Word Count:

27 200

Abstract

The Amundsen Sea, West Antarctica, contains some of the fastest retreating ice streams in the world. Studies have proposed that the ice streams in the region could be subject to unabated and irreversible retreat, given that large extents of the region are grounded on retrograde bedrock, below sea level and thus could be susceptible to marine ice sheet instability. Ocean forced basal melting of ice shelves, determined predominantly by the temperature of the water masses interacting with the ice shelves, is the primary mode of mass loss from the region; given that melt induced thinning impacts the stability and position of the grounding line. Understanding the dynamic ice sheet response to changes in local ocean temperature offers a means to explore the projected mass loss contribution to sea level rise, under a warming climate.

Performance metrics for 27 CMIP5 AOGCMs have been calculated in order to identify a subset of models that best reproduce observations of ocean temperature in the Southern Ocean. Projected ocean temperature in the ASE over the 21st century, as produced by the subset, have been used to calculate a projected melt rate forcing for ASE glaciers. Melt rate forcings have been applied to the BISICLES ice sheet model to project the response of the ASE to changing climate. Accounting for the uncertainties associated with the model set-up, two sets of values for the ice stiffening factor and basal traction coefficient were used. Projected sea level contribution from ASE glaciers ranges between -0.02 and 12.3 cm by the end of the 21st century. Sea level rise estimates are found to be more sensitive to chosen parameter sets than the range of projected melt rate forcings, indicating that ice sheet model internal uncertainty exceeds the uncertainties associated with the choice of AOGCM.

Acknowledgements

Firstly, I would like to thank Tony Payne for supervising me throughout this project. Despite having an unbelievably busy schedule, Tony has always made time to help me and I appreciate that more than I can say.

Thank you to Victoria Lee and Claire Donnelly for helping me with BISICLES. I now understand that modelling is far from simple. Victoria especially was fundamental in the completion of this project and has taken a huge amount of her time to help me, which I am extremely grateful for. I would also like to thank Isabel Nias for her unwavering support, putting up with my persistent essay-length emails and allowing me to have access to every single script she'd written in order to make my own project. If it weren't for her own PhD Thesis, this project would not were possible.

Finally, and most importantly, I would like to thank Laura Devitt for keeping me sane this year. I couldn't have done it without you.

Author’s Declaration

I declare that the work in this dissertation was carried out in accordance with the requirements of the University's *Regulations and Code of Practice for Research Degree Programmes* and that it has not been submitted for any other academic award. Except where indicated by specific reference in the text, the work is the candidate's own work. Work done in collaboration with, or with the assistance of, others, is indicated as such. Any views expressed in the dissertation are those of the author.

SIGNED: .....  ..... DATE: 28/11/2018

Table of Contents

List of Figures

List of Tables

Chapter 1 : Introduction

1.1 Aims and Significance

The aim of this investigation is to explore the projected evolution of the glaciers in the Amundsen Sea Embayment (ASE), West Antarctica, over the 21st century. Projected temperature from a subset of models from the Climate Model Intercomparison Project Phase 5 (CMIP5) (Collins et al., 2013) will be used to provide a forcing for the BISICLES ice sheet model (Cornford et al., 2013). The results of this study provide a novel insight into the projected evolution of ASE glaciers associated with specific future emissions scenarios.

Rising sea level, in response to anthropogenic climate change, is to have global and extreme consequences (Jevrejeva et al., 2014). The relative contribution of ice sheets to global mean sea level rise is expected to increase in the future, with ice sheets becoming the largest, and most uncertain, contributor to rising sea level (Meehl et al., 2007; Rignot et al., 2011; Church et al., 2013). Large portions of the ASE have bedrock situated below sea level, meaning that these marine terminating glaciers could be susceptible to rapid and widespread retreat through the marine ice sheet instability theory (Ritz et al., 2015; Schoof, 2010). Using projections of ocean temperature to force numerical ice flow models provides a means by which we can explore the modelled evolution of ice streams under a changing climate (Nowicki et al., 2016; Naughten et al., 2017). Estimations of the projected ice sheet contribution to sea level rise, as output from ice sheet models, is invaluable for governments to plan for adaptation to climate change.

1.2 Objectives

The following objectives were defined in order to meet these aims:

1. **Evaluate CMIP5 model simulations of ocean temperature in the Southern Ocean.** To achieve this, performance metrics for 27 of the CMIP5 models will be calculated by comparing their output with observed ocean potential temperature in the Southern Ocean over the period 1979 to 2016.
2. **Investigate projections of ocean temperature from 2017 to 2100.** For a subset of models that best reproduced observed temperatures (objective 1), 21st century temperature projections over the Southern Ocean forced with RCP2.6 and RCP8.5

will be explored. Furthermore, the 21st century projected temperature averaged over the Amundsen Sea will then be investigated to understand local temperature forcing.

3. **Determine the projected evolution of ASE glaciers, and their contributions to sea level rise, from 2017 to 2100 under a changing climate.** To do this, BISICLES will be forced with melt rates parameterised from three CMIP5 model projections of ocean temperature in the ASE. Two variations of the parameters obtained in the initialisation procedure will be used, in order to assess some of the internal model uncertainty.

1.3 Thesis Structure

The above objectives will form the basis of the thesis structure. To begin with, Chapter 2 will consist of a discussion of the existing literature surrounding the Amundsen Sea Embayment; including a commentary of the geographical region, observed changes to the glaciers in the embayment and the climatological controls on ice dynamics in the region. The use of numerical modelling of climate and ice sheets will be discussed. In Chapter 3, by assessing the performance of the CMIP5 models at reproducing observations, a subset of best performing models will be identified. In Chapter 4, the projected ocean temperature produced by the subset of best performing models will be investigated. Finally, Chapter 5 will use a number of these projected temperatures to parameterise a melt rate forcing for the BISICLES ice sheet model. Resulting projections of ASE evolution will thus the response of the ASE glaciers to projected future climate under the RCP8.5 forcing scenario. Finally, Chapter 6 will address the main conclusions to each of the three objectives.

Chapter 2 : Literature Review

2.1 Introduction

The Amundsen Sea Embayment (ASE) contains some of the fastest retreating glaciers in Antarctica. As the region is grounded on retrograde (deepening inland) bedrock largely situated below sea level, grounding line retreat could lead to extensive mass loss.

This chapter will firstly provide background of the focus region, the ASE, discussing some of the recent observed changes to the condition of the drainage basins and further consider the physical mechanisms behind these changes. Ice-ocean interactions in the region will then be described, with a focus on ocean driven melting mechanisms and heat delivery toward the ice sheet. The final section will discuss the use of numerical models for understanding ice-ocean interactions and the way in which models can be utilised to provide projections of ice sheet evolution when forced using climate model simulations.

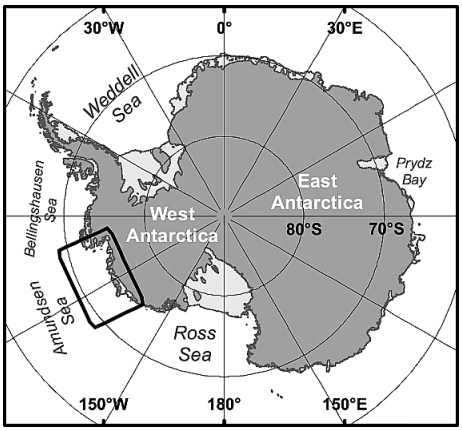

Figure 2.1: *Map of Antarctica. Black box shows location of the ASE (Nitsche et al., 2007; figure 1).*

2.2 Amundsen Sea Embayment (ASE)

The ASE is a focal region for Antarctic ice sheet mass loss (Mcmillan et al., 2014; Shepherd et al., 2012), contributing 10% of present global mean sea level rise (Mouginot et al., 2014). The region is situated west of the Antarctic Peninsula, along the Pacific coast of the West Antarctic Ice Sheet (WAIS) between 118^{o}W and 102^{o}W. The ASE constitutes a number of pure and topographic ice streams, in

three catchments; where these ice streams flow at velocities faster than surrounding ice (Pritchard et al., 2012). The ASE glaciers are situated on a retrograde bed, grounded below sea level (Vaughan, 2008; Gudmundsson, 2013), thus making the region susceptible to unstable and rapid retreat under the marine ice sheet instability feedback (Schoof, 2007). Recent literature proposes that this instability feedback may have already been initiated (Favier et al., 2014; Joughin et al., 2014; Parizek et al., 2013), such that could result in a contribution of up to 1.2 - 1.5 m of global sea level rise (Rignot, 2008; Vaughan, 2008).

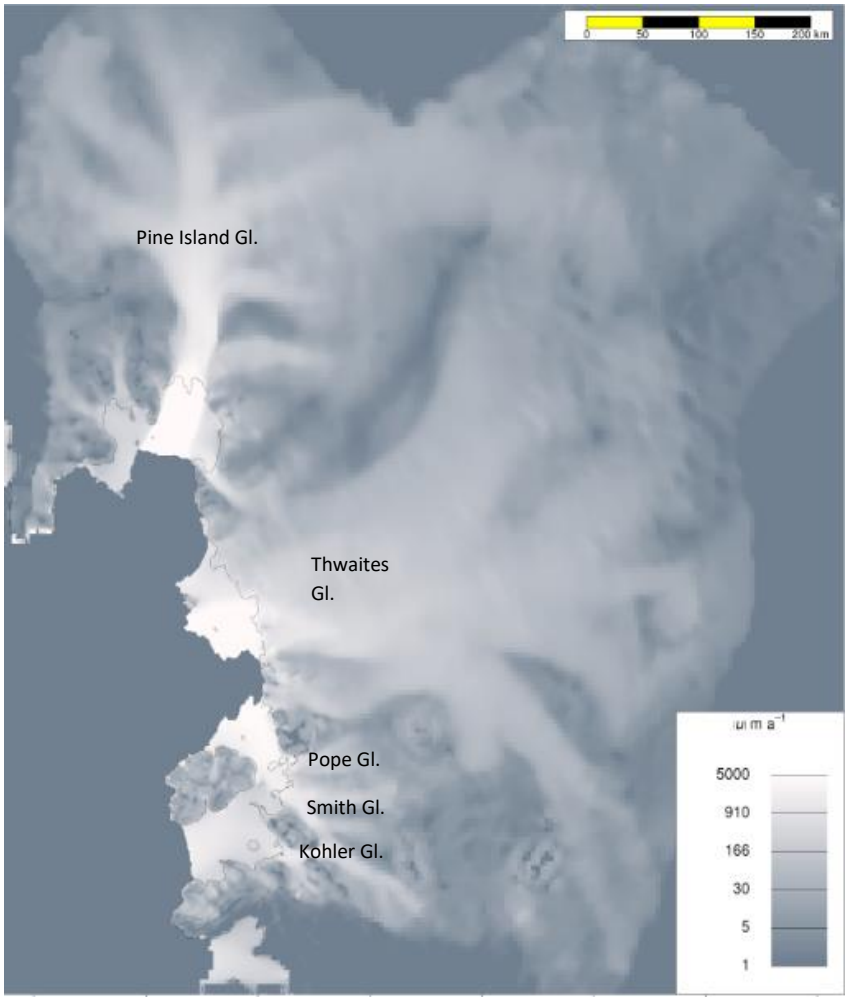

Figure 2.2: *Map of the ASE with glaciers labelled.*

2.2.1. Pine Island Glacier (PIG)

Pine Island Glacier, the "weak underbelly" of WAIS (Hughes, 1981), is presently accountable for ~20% of the ice flux from the West Antarctic Ice Sheet (Wingham et al., 2009; Rignot et al., 2008). PIG is made up of nine tributary glaciers that merge into one primary, central trunk (Turner et al., 2017). The glacier expels ice into the 55 km long and 30 km wide Pine Island Ice Shelf (PIIS), which is topographically constrained by a narrow embayment; acting as a lateral buttress to ice shelf advance.

The marginal shielding that this topographic confinement provides is essential in determining the level of exposure the ice has to forcing from the surrounding ocean, thus playing a crucial role in preventing unstable grounding line retreat.

2.2.2. Thwaites Glacier

Thwaites Glacier is situated to the west of PIG. Broader than its neighbour, the central trunk of Thwaites Glacier feeds into two separate counterparts: a floating ice tongue with a width of 50 km and the eastern ice shelf (Konrad et al., 2017), both with differing flow speeds (Mouginot et al., 2014). The grounding line of the floating ice tongue is retreating at 4 km yr^{-1} which contrasts with the eastern shelf which flows at 0.8 km yr^{-1} (Tinto and Bell, 2011). The slow flow of the eastern shelf is attributed to a bathymetric pinning point beneath the ice shelf resulting in crumping of the ice inducing longitudinal stresses and therefore buttressing (ibid.). As the ice shelf is unconfined by topography at its periphery, it provides little longitudinal stress through buttressing, and therefore flow of the ice from the glacier is relatively insensitive to oceanic forcing given that there is no substantial reduction in the resistive force offsetting outward flow (Parizek et al., 2013; Nias, 2017; Konrad et al., 2017).

2.2.3. Pope, Smith and Kohler (PSK) Glaciers

The remaining smaller ice streams, Pope, Smith and Kohler glacier (PSK), lie to the far west of the embayment. These smaller streams merge upstream, flowing together through a narrow trench that lies >2 km below sea level (Holt et al., 2006). Pope and Smith Glaciers drain into the Crosson Ice Shelf whilst the Kohler glacier drains into the Dotson Ice Shelf. Kohler is situated on the western boundary of the embayment with Smith and Pope Glaciers neighbouring to the east (Scheuchl et al., 2016). Whilst exposed to equivalent atmospheric forcing due to their geographical proximity, the differing dynamics of these ice streams indicates that their sensitivities to forcing differs, largely attributable to their varying bed and ice shelf geometries (Nias, 2017).

2.3 Observed Changes to ASE Glaciers

The use of remote sensing techniques to monitor changes to the ASE glaciers is crucial for understanding the magnitude and patterns of recent changes in the region; in addition to providing data with which researchers can establish and run numerical ice sheet models (Scheuchl et al., 2016). A satellite record of velocity was available since 1992 where Inferometric Synthetic Aperture Radar (InSAR) sensors are used track the movement of surface features. With the exception of the eastern Thwaites and Dotson ice shelves, every ice stream and floating shelf in the ASE has exhibited acceleration between 1996 and 2008 (Mouginot et al., 2014).

2.3.1. Pine Island Glacier

Thinning of PIG, through analysis of marine sediment cores, was initiated in the 1940s when incursion of water beneath the grounded glacier occurred, forming a cavity, and resulting in its eventual ungrounding from a topographic ridge on the Antarctic continental shelf in the 1970s (Smith et al., 2017; Jenkins et al., 2010). Thinning since was observed directly, beginning in the 1980s, where it has accelerated largely due to enhanced ocean forced melting (Pritchard et al., 2012). Altimeter measurements indicate an increased surface lowering of PIG at the grounding line from 1 m yr^{-1} in 1992, to 5 m yr^{-1} by 2010 (Konrad et al., 2017). Moreover, rapid grounding line retreat occurred during a period of extreme mass loss from 2002 to 2008; where rates of retreat surpassed 1 km yr^{-1} (Mouginot et al., 2014; Park et al., 2013). In light of these changes, a modelling study by Katz and Worster (2010) infers that PIG has surpassed a threshold of retreat, indicating continual and unabated retreat is underway. However, Kondrad et al. (2017) presented that more recently, from 2010-2015, the rate of lowering at the grounding line has slowed, which could indicate a period of stability, which would contradict the findings of Katz and Worster (2010).

2.3.2. Thwaites Glacier

Thwaites glacier has experienced both spatially and temporally varying retreat rates, illustrating the complexity of its dynamics. The onset of thinning began in the early 1990s, where a rate of 1-2 m yr^{-1} was observed at the grounding line (Konrad et al., 2017), which increased to 4m yr^{-1} in 2015. Drawdown of the glacier surface, in response to this initial thinning at the grounding line, did not spread to the interior until 2000 when thinning then slowed; causing temporary stability (*ibid.)*. Acceleration of both the glacier and the floating ice tongue has been observed from 2007, where an increase in the velocity of the glacier was detected up to 100 km upstream (Mouginot et al., 2014). However, a slowdown of the eastern ice shelf over this period was observed. This slowdown was believed to be due to a decoupling of the ice shelf in the east from the fast-flowing western ice tongue, given the reduction in shear stresses acting on the shelf (ibid.). Rignot et al. (2014) found that over the period from 2000 to 2011, the whole extent of the grounding line has undergone retreat, with the greatest extent of this reaching up to 17 km.

2.3.3. Pope, Smith and Kohler Glaciers

PSK glaciers have experienced the greatest degree of thinning, acceleration and grounding line retreat of the glaciers in the embayment (Rignot et al., 2014; Scheulchl et al., 2016). It is believed that the initiation of retreat observed in the PSK catchment began at the grounding line prior to the altimeter

record. Over the satellite period, PSK has exhibited large rates of surface lowering with rates of over 3m yr^{-1} occurring toward the beginning of the 1990s with an acceleration to 7m yr^{-1} in 2015 (Konrad et al., 2017). Observations of surface lowering were found further upstream from the grounding line, indicating a propagation of the thinning signal. Propagation occurs in PSK to less of an extent than PIG and Thwaites, however, which is likely attributable to the ice streams and tributaries residing in small narrow troughs, resisting the speed up (Flament and Remy, 2012).

Each of the glaciers in the basin have experienced different rates and timings of retreat. Smith accelerated by 83% from 1996 to 2007 and since 2008 has continued to speed up (Scheuchl et al., 2016). In contrast, Pope reached peak velocity in 2010, experiencing an 11 km retreat from 1996 to 2014. Whilst Kohler experienced peak velocity in in 2008, there was an advance of its grounding line where it currently resides at the point at which it was grounded in 1992 (*ibid*).

2.4 Amundsen Sea Ice Dynamics

In the ASE, there are complex responses to external climate forcings taking place, with each ice stream exhibiting different rates of thinning and retreat over the satellite record. Given the dependence of ice sheet mass balance on glacier dynamics, understanding the processes by which glaciers and ice sheets lose mass is an important component for predicting future change (Rignot et al., 2008). This section will briefly outline mass loss dynamics in the region to provide background understanding of observed behaviour so that the causes of these changes can determined.

2.4.1 Ocean Forced Thinning

Ocean forced basal melting of floating ice shelves, was found to be the greatest driver of mass loss from ice shelves, exceeding mass lost from iceberg calving (Depoorter et al., 2013; Rignot et al., 2013), largely due to the subsequent acceleration of grounding line retreat in response to this thinning (Pritchard et al., 2012; De Rydt et al., 2014; Rignot, 2008). The grounding line describes the region over which ice transitions from being grounded on bedrock to floating, as an ice shelf or tongue. Melting of mass at the grounding line causes thinning, leading to ungrounding and subsequent retreat of the grounding line. As an increased quantity of ice becomes ungrounded, the area of bedrock in contact with ice decreases, resulting in decreased basal traction and thus an increase in ice flow (Konrad et al., 2017; Joughin et al., 2010). This glacier speed-up, once initiated at the terminus, can propagate up to 100 km upstream (Payne et al., 2004). This propagation results from a process whereby local thinning at the grounding line causes an increased thickness gradient upstream and therefore increased gravitational driving stress (Payne et al., 2004). Thus, the response of the ice

stream to thinning at the terminus is an increased velocity of flow downstream in addition to a surface lowering over much of the glacier trunk. This has been observed over much of the ASE.

The rate at which melt induced thinning occurs along the base of the ice shelf has a large variability in response to thermal forcing. Melting is dictated partially as a function of local oceanic temperature and the local ice thickness at point of ocean contact (Assmann et al., 2013). Observed melt rates are variable across ice shelves in the ASE, with domain averaged melt rates of 15-18m yr^{-1} for PIG, Thwaites and the Crosson Ice Shelf. Melting of these glaciers is particularly large in comparison to other Antarctic ice shelves (Shepherd et al., 2004; Depoorter et al., 2013; Rignot et al., 2013).

Due to the challenges associated with accessing ice shelf cavities, observational melt rates of ice shelves are sparse. Therefore, melt rates can be parameterised in a number of ways (De Rydt et al., 2017). Parameterisations are most commonly defined as a function of depth (Joughin et al., 2010; Favier et al., 2014). Due to the depression of the melting point with depth (Foldvik and Kvinge, 1974), these parameterisations assume that melting is highest at the grounding line, which is located at the thickest, and therefore deepest, part of the shelf (Pritchard et al., 2012). Payne et al. (2007) found rates exceeding 100m yr^{-1} over ice in close proximity to the grounding line. However, more recent studies have argued that melt rates are not necessarily highest at the grounding line, but rather a distance from, or adjacent to, the grounding line (Jenkins, 2011; Galton-Fenzi, 2009; Parizek and Walker, 2010; Gladstone et al., 2017; De Rydt et al., 2016).

2.4.2 Marine Ice Sheet Instability (MISI)

Numerical modelling studies have suggested that a number of the ASE glaciers have experienced, or are currently experiencing, marine ice sheet instability (MISI) (Ritz et al., 2015). Church et al. (2013) argue that this internal, positive, feedback is a fundamental process contributing to the large uncertainties associated with projections of future sea level rise (SLR). Should MISI be initiated in the region of the ASE, rapid and widespread mass loss could occur having a large impact on SLR, making it an important feedback for ice sheet models to capture.

The theory states an ice sheet grounded below sea level on a retrograde bed is inherently unstable and likely to be subject to accelerated retreat (Weertman, 1974), if the ice is exposed to surrounding warmer ocean (Gudmundsson, 2013). The mathematical basis for this instability being that the volume of ice that crosses the grounding line increases as a function of thickness, given that a retrograde bed deepens inland, ice thickness at the grounding line increases upstream (ibid.).

Instability will be initiated if a stable grounding line is perturbed by an oceanic forcing sufficient to unground the ice from its stable position (Schoof, 2007). Furthermore, once retreat is initiated, retreat will continue, unabated, even if the initial perturbation is removed (Pattyn et al., 2013). Retreat will end when the grounding line reaches a new stabilised position on a local topographic maxima or prograde bed (Katz and Worcester, 2010).

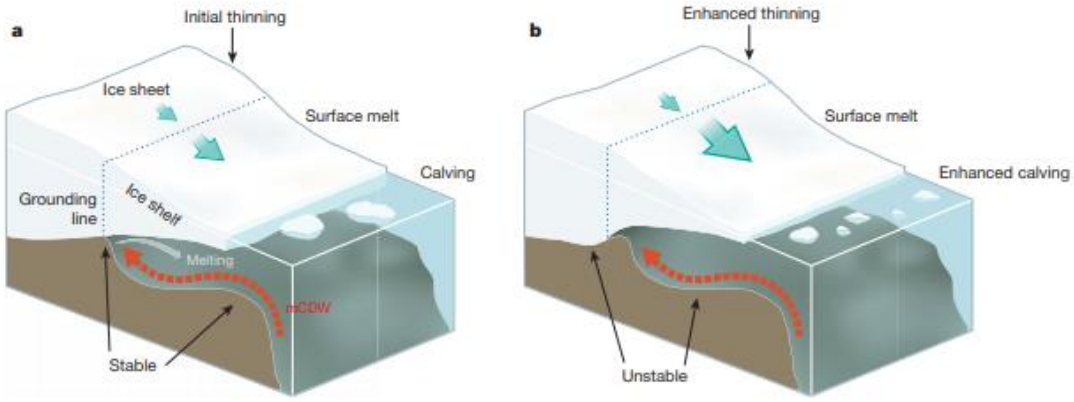

Figure 2.3: *Diagram illustrating stable (a) and unstable (b) grounding lines of two marine terminating glaciers. (From Hanna et al., 2013, Figure 3).*

Modelling studies have demonstrated that an upward sloping, prograde, bed provides stability and will be less susceptible to retreat under perturbations (Ritz et al., 2015; Jenkins et al., 2016; Jacobs et al., 2011; Goldberg et al., 2009). Local topographic maxima, which manifest as local regions of prograde bed, can provide intermittent periods of stability for a retreating grounding line (Joughin et al., 2010; Schoof, 2010). Though ocean forcing of a grounding line on prograde bed can cause retreat, modelling studies have shown that once this applied perturbation is removed, the grounding line will advance to its previous stable position (Pattyn et al., 2012).

The MISI feedback can be limited by the presence of an ice shelf which acts to laterally, in two horizontal dimensions, resist outward flowing forces of an ice stream, buttressing flow (De Rydt et al., 2015; Gudmundsson et al., 2013); through shear stress at the intersection between the ice sheet and ice shelf. As ice flux across the grounding line is a function of its thickness, grounding line retreat upstream, where ice is thicker, results in an increased volume of ice crossing the grounding line and subsequently contributing to sea level rise (Dupont and Alley, 2005). Buttressing, however, acts to stabilise the position of the grounding line and thus reduce this increase in mass flux (Goldberg et al., 2009; Gudmundsson, 2013; Jenkins et al., 2016). The overall retreat of a grounding line is therefore a sum of the two opposing feedbacks: basal melting acting to accelerate retreat and buttressing acting to prevent retreat when the ice stream is in equilibrium (Arthern and Williams, 2017).

2.5 Oceanographic Forcing

Ocean driven basal melting is responsible for the majority of mass loss in the ASE (Dinnimann et al., 2016; Jenkins et al., 2011; Pritchard et al., 2012), where the temperature of the water masses situated on the 400-1200 m deep continental shelf range from -2°C to >1.5°C (Jenkins et al., 2016), thus providing heat sufficient to melt the undersides of ice shelves in the region.

2.5.1. Antarctic Circumpolar Current

The Southern Ocean denotes the large body of water that surrounds Antarctica, extending from the continent's coast to ~30^{o}S and includes the Atlantic, Indian and Pacific Oceans. The wind and buoyancy driven Antarctic Circumpolar Current (ACC) is the world's largest ocean current (Orsi et al., 1995). Situated at 45-65^{o}S, ACC acts as a barrier to climate further north of its bounds allowing the ice sheet to remain isolated within its own climate (Downes and Hogg, 2013). Given the effect of the Coriolis force on circulation, the ACC travels eastward around the continent, with geostrophic winds travelling at right angles, thus being driven south toward the Antarctic continent making the current a factor in determining the prevailing winds interacting with the ice sheet (Meijers et al., 2012; Orsi et al., 1995). Transporting approximately ~130Sv of water within its current (Rintoul et al., 2001), the ACC dominates oceanic circulation in the Southern Ocean, with particular influence on the circulation of water masses that interact with the Antarctic Ice Sheet (Talley et al., 2011). Though the ACC encapsulates the entire Antarctic continent, it has the greatest southern reach in the Pacific Ocean sector, meaning the current lies in relatively close proximity to WAIS and thus the ASE. As a result, the current is largely responsible for heat delivery to the region (Thoma et al., 2008; Walker et al., 2008; Little and Urban, 2015).

2.5.2. Modes of Basal Melting

Several studies have proposed differing mechanisms of melting that are responsible for the high rates of retreat observed in the ASE (Dinnimann et al., 2016; Jacobs et al., 2011; Depoorter et al., 2013). These modes are broadly categorised into three different behaviours, first proposed by Jacobs et al (1992). The first mode describes delivery of high salinity, cold shelf water, formed through brine rejection, which mixes with surrounding freshwater to form ice shelf water (SW). This water enters cavities where the freezing point decreases with depth, and therefore the SW causes basal melting. Mode 2 describes the incursion of warm, >4°C above the in situ freezing point, Circumpolar Deep Water (CDW) on shelf. Finally, Mode 3 involves Antarctic Surface Water (AASW) entering the cavity. AASW has a cold core but also an upper layer that warms seasonally. AASW has a temperature near

the surface freezing point, which, when entering the cavities at depth, lies above the in *situ* freezing point, causing basal melting. Mode 2 was identified as the most prominent mode of ocean forced basal melting in the ASE and will be discussed in the following sections.

2.5.3. Circumpolar Deep Water

CDW is the largest mass of water of the ACC (Orsi et al., 1995) and is composed of a mixture of deep-water masses from all oceans. CDW is defined by Whitworth et al. (1987) as the water mass in the Southern Ocean that has a density of between 28.00 to 28.27kgm^{-3}. Renowned for its relatively warm core temperature, CDW can reach up to 4°C above the in situ freezing point. As the current travels eastward around the continent, a limb of the Ross sea gyre bifurcates, with one stream of flow travelling southeast-ward toward the ASE (Orsi et al., 1995), bringing warm water toward the continental shelf (Rodriguez et al., 2016).

The absolute temperature maximum of this water has of yet exceeded 1.5°C on shelf (Assmann et al., 2013), however these temperatures are indicating a warming trend, present since the end of the 20th century. Schmidkto et al. (2014) propose that a warming of 0.1 to 0.3°C per decade has occurred since the 1990s as illustrated in observational data. The CMIP5 ensemble project that CDW warming will occur over the 21st century resulting in an increase in its core temperature of 0.33-0.41°C (Sallée et al., 2013).

2.5.4. CDW Delivery to the ASE

Around much of the Antarctic Continent, CDW is blocked from the coast due to the presence of near freezing surface waters which depress the thermocline at around 300-700m (Schmidtko et al., 2014, Assmann et al., 2013; De Rydt et al., 2014; Dutrieux et al., 2014; Jenkins et al., 2016). Furthermore, the continental shelf acts as a barrier to the upward sloping CDW from accessing the grounding line around much of the continent (Pritchard et al., 2012). In the ASE, the continental shelf break at ~500-600m depth, acts as a barrier to onshore flow of deep water, given that the depth of CDW off-shelf lies below the topography (Walker et al., 2007; Wåhlin et al., 2012) However, observations indicate that a thin layer of this warm water remains permanently on shelf (Walker et al., 2007), with shoaling increasing with at rates exceeding -50±18m decade^{-1} (Schmidkto et al., 2014), changing the overall ocean temperature on shelf in the embayment (Turner et al., 207; Webber et al., 2017).

With troughs of ~700 m depth at the continental shelf break (Wåhlin et al., 2012), a number of mechanisms act to drive this warm water mass, that resides at depths below ~1000 m, onto the ASE

shelf (Schmidkto et al., 2014; Smith et al., 2017). Martinson and McKee (2012) propose four differing modes of transport, with eddies being the dominant mechanism followed by upwelling (St-Laurent et al., 2003; Dinniman and Klinck 2004). Arguably the most discussed mechanism of on shelf flow is wind driven Ekman upwelling (Wåhlin et al., 2012; Wåhlin et al., 2013; Dutrieux et al., 2014). However, there remains some uncertainty as to the exact mechanisms that are resulting in incursion of warm water on shelf in the ASE (Webber et al., 2017), particularly given the scarcity of observations (Wåhlin et al., 2013). Regardless, this observed incursion of CDW has been established as the dominant driver of grounding line retreat and subsequent mass loss observed in the ASE (Jenkins et al., 2010; Hellmer et al., 2012; Dinniman et al., 2016).

Beneath the floating ice shelves in the ASE lies a complex bedrock of bathymetric irregularities, subglacial ridges and dendritic troughs formed from past glacial flow (Assmann et al., 2013). Once on shelf, routing of CDW onto the inner depths of the continental shelf is generally dictated by the trough system (Nitsche et al., 2007; Nitsche et al., 2013). Transport of CDW into Pine Island Bay occurs predominantly through the central and eastern troughs at 113°W and 102-108°W respectively (Webber et al., 2017; Wåhlin et al., 2010, Thoma et al., 2008; Assmann et al., 2013). Warmer waters are delivered into Pine Island Bay through the eastern trough whilst denser, cooler waters are transported through the central trough (Assmann et al., 2013). Once CDW has entered these topographic lows, the warmest, densest waters will sink to the bottom and be routed into ice shelf cavities (Nitsche et al., 2007), accelerating melting of the glaciers (Pritchard et al., 2012; Thoma et al., 2008).

2.5.5. Obtaining Basal Melt Rates

Basal melt rates can be calculated using several different methods; given that direct measurements at the base of floating ice shelves, where melt is highest, are not yet easily attainable. There are differing methods of estimating basal melt rates. For example Rignot and Jacobs (2002) use mass conservation to calculate basal melting between the grounding line and a flux gate downstream, by attributing observed thinning to basal melting, assuming steady state conditions. Alternative methods involve using thickness change rates combined with velocity to estimate the mass budget, without the assumption of steady state ice shelf. This was performed by Depoorter et al., (2013) and Rignot et al. (2013).

In contrast, basal melt rates can be estimated by assuming an observed relationship with temperature. Recent studies have utilised either constant or temperature dependent values of

melting to capture the velocity related heat exchange at the ice interface, the resultant melt rates are therefore either linear or quadratically related to temperature (Lazeroms et al., 2018). Holland et al. (2008) discuss a number of these relationships, which differ substantially. MacAyeal (1984), in a simple modelling study, determined a "power 2 relationship" of melting when considering deep water temperatures. In contrast, Rignot and Jacobs (2002) used satellite observations to plot a linear relationship between basal melting and temperature. Moreover, Holland et al. (2008) use a full ocean GCM in their modelling study and obtain a quadratic relationship between melt and temperature which manifested as a result of the expression of velocity to depend linearly on ocean mixing, which is also linearly related to temperature (Lazeroms et al., 2018).

2.6. Atmospheric Forcing

Atmospheric forcing, generally in the form of winds, has a substantial control on delivery of water masses toward the ice shelves in the ASE (Jenkins et al., 2016; Pritchard et al., 2012; Walker et al., 2007; Thoma et al., 2008; Wåhlin et al., 2010).

2.6.1. Atmospheric Circulation

Over the West Antarctic, westerly winds travelling along the continental shelf break lead to south-eastward movement of CDW toward the troughs in Pine Island Bay (Thoma et al., 2008; Walker et al., 2007). Low pressure over the continental shelf drives weak easterly and westerly winds resulting in an upward sloping of isopycnals, including CDW (Schmidkto et al., 2014; Bintanja et al., 2013). Therefore, the location of low pressure systems has an influence on regional ocean circulation. These westerly winds over the Southern Ocean have experienced a poleward migration, in addition to a strengthening, since the 1950s (Spence et al., 2014). This trend is expected to increase in the future, resulting in increased delivery of heat toward the ASE, potentially causing a warming of 200-700m deep coastal waters in the West Antarctic of over 2°C (ibid.).

Rodriguez et al. (2016) propose that delivery of CDW on shelf in the ASE is driven by the local wind stress curl as opposed to the wind stress which was proposed by Thoma et al. (2008). This was supported by Dutrieux et al. (2014) who found that periods of decreased basal melting of ice shelves coincided with a weakened wind stress curl that was causing a depression of the thermocline. Stronger westerlies could also be associated with increased presence and activities of eddies which also result in enhanced CDW flow (Hogg et al., 2008). However, the complex relationship between basal melt, CDW volume intrusion and the strengthening of polar westerlies are not yet fully understood (Dinniman et al., 2012).

2.6.2. Seasonal Variability

Seasonal changes to the strength and position of westerlies in the Southern Ocean were associated with changes in CDW thickness on shelf in the ASE (Bracegirdle et al., 2008; Thoma et al., 2008; Walker et al., 2008). This seasonal and interannual variability of hydrographic conditions in the ASE were observed (Webber et al., 2017; Wåhlin et al., 2013). However, given limited observational datasets in the region, there is a large discrepancy between findings. For example, Wåhlin et al., (2013) found the thickness of a warm layer of water on shelf in the ASE to be at its maximum from March-May (Autumn), coinciding with a peak in the temperature of the bottom warmest waters (Arneborg et al., 2012). Indicating an increased transport of CDW on shelf during these months. In contrast, a deeper winter mixed layer between September- November (Spring) resulted in a thinner layer of deep water on shelf, likely due to the suppression of the thermocline and increased mixing with cooler waters. These findings are consistent with a study by Mallet et al. (2018), with the use of a seal tag dataset, who found a thicker CDW layer on shelf in late Winter/Spring (August-October) compared with late Summer/Autumn (February-April) in the eastern shelf. Also confirmed by Schodlok et al. (2012) and Arneborg et al. (2012). In contrast, Thoma et al. (2008) proposed a temperature maximum over the eastern shelf from Winter to Spring (June-November), as a result of maximum CDW onshore flow, and a minimum from Summer to Autumn (December-May); also supported by Steig et al. (2012). Thus, though the timing of these changes are not fully agreed on, a seasonal cycle in CDW thickness and thus ASE ocean temperature has been widely recognised.

2.6.3. Amundsen Sea Low (ASL)

The Amundsen Sea Low (ASL) is a low-pressure system situated at ~150°E in the Southern Ocean (Turner et al., 2013) which dominates circulation patterns over much of the western ice sheet, in addition to being responsible for the large seasonal variability in climate observed in the ASE (Connolley, 1997). The location of the system's low-pressure centre migrates as part of an annual cycle, moving westward from 110°W during austral summer to 150°W in winter (Turner et al., 2017). Additionally, this longitudinal migration varies, with a 20° standard deviation in summer that reaches 35° in winter. Furthermore, the ASL migrates poleward by 1-2° between summer and winter. Whilst there is some understanding behind these patterns and the controlling features, the irregularity of the variability on both seasonal and monthly timescales makes understanding the changes to the position of the ASL complex (Turner et al., 2013).

The depth and position of the ASL was shown to partially control the delivery of CDW to the ASE, Thoma et al. (2008) demonstrated in their modelling study that a deepened ASL resulted in a strengthening of westerly winds, this in turn leading to a strengthening of the eastward flowing CDW toward the shelf. The seasonal cycle modelled indicates on shelf flow to be at a maximum during winter and weakened during the summer in response to the seasonal migration and deepening of the ASL (Turner et al., 2017).

2.6.4. Southern Annular Mode (SAM)

The Southern Annular Mode (SAM) is a dominant mode of variability in climate at high southern latitudes (Turner et al., 2013) and influences much of the climate over the western ice sheet and surrounding ocean. The SAM describes the pressure gradient between low and high latitudes which is responsible for defining the strength of the resulting circumpolar winds. The SAM oscillates seasonally between positive and negative phases. When the SAM is in its positive phase, atmospheric pressure in the high latitudes is lower, causing stronger westerlies over the continental shelf which in turn drive the onshore flow of water masses toward the ice sheet (Turner et al., 2017; Marshall 2003; Jacobs, 2006). Decreased CDW delivery on shelf is therefore associated with the weak westerlies and easterlies that manifest during a negative SAM phase.

Over the last 30 years, as a response to anthropogenic emission of aerosols and the resulting loss of stratospheric ozone, the SAM has become increasingly positive (Gille, 2008). This positive SAM phase has resulted in a shift of the ACC toward the poles, such that was projected to continue in the future (Turner et al., 2017). Associated with this positive phase, a strengthening and poleward movement of westerlies are projected (Dinniman et al., 2012). Consequences of the SAM migration include a migration of the ASL and further alterations to local atmospheric and oceanic circulation in the ASE (Miller et al., 2006). It has been suggested that this trend is responsible for increased durations of CDW upwelling onto the continental shelf (Gille, 2002), and therefore increased CDW delivery would be expected to occur in the future, should this trend continue.

2.6.5. El Nino Southern Oscillation (ENSO)

There is a strong correlation over the observational record that ENSO correlates with the westerly winds in the ASE (Rodriguez et al., 2016; Fogt and Bromwich, 2006) ENSO was found to substantially influence the location and depth of the ASL, associated with the prominent teleconnections between climate in the West Antarctic and tropical climate in the Pacific (Ding et al., 2011; Turner et al., 2017). During El Nino years, the ASL weakens due to the Rossby waves travelling from the tropics (Turner,

2004). As the ASL weakens, the westerlies transporting warm CDW toward the continental shelf also weaken, meaning El Nino is associated with reduced CDW delivery. In contrast, El Nina years' experience a deepening of the ASL, thus causing increases strength westerlies thus stronger delivery of CDW toward the ASE (Turner et al., 2017). In relation to the ASE glaciers, the initial retreat of PIG, which initiated in the 1940s, was attributed to infiltration of warm CDW that coincided with an El Nino event (Smith et al., 2017), likely La Nina, whereby westward travelling winds intensified encouraging movement of CDW toward the shelf.

2.7. Climate Modelling

Climate modelling provides a means by which to recreate physical processes at the earth's surface and produce forecasts for periods where there is no available observational data. Atmosphere-ocean general circulation models (AOGCMs) are the primary models used for running simulations projecting future climates under various forcing scenarios (Little and Urban, 2016).

2.7.1. CMIP5 Ensemble

The CMIP5 ensemble, produced by the World Climate Research Program (WCRP), constitutes 50 atmosphere-ocean general circulation models (AOGCMs) and earth system models (ESMs) from 21 modelling groups (Taylor et al., 2012). The output from the ensemble of models is featured heavily in the Intergovernmental Panel on Climate Change (IPCC) Fifth Assessment Report (AR5) (Collins et al., 2013). The ensemble run projections of climate under four difference anthropogenic forcing scenarios, from a scenario where climate change modest due to mitigation (RCP2.6) and an extreme, business as usual, scenario of extensive climate change (RCP8.5). The variance between models within the ensemble, specifically their projections, are the sum of a number of components including configuration of each model, grid resolutions, internal variability and finally an interaction term describing the different response of each model to each climate forcing scenario used (Little et al., 2015; Taylor et al., 2012).

One of the primary aims of the CMIP5 ensemble was to establish reasons for substantial differences in model simulations, despite identical forcing scenarios. This was discussed at length by Taylor et al. (2012). Each model is comprised of separate modelling components representing ocean, atmosphere, land, sea ice and in some cases for the ESMs, representation of atmospheric chemistry and similar biogeochemical cycles are included, meaning that each model is representing different physics and has different formulations and resolutions.

2.7.2. Climate Modelling Biases in the Southern Ocean

Climate model performance can be assessed through comparison with measured observations to establish model errors and biases (Meijers et al., 2014). Calculating model errors provides a means to assess the uncertainty of projections, assuming that models that are poor at representing observed climate in the past will produce unreliable estimates for the future (Knutti and Sedlacek, 2013). The following are some examples of studies that have explored the performance of the CMIP5 ensemble in representing the Southern Ocean climate, by validating output against observations.

Little and Urban (2016) performed an analysis of a subset of the CMIP5 ensemble and compared results with observations of ocean temperature data. Findings suggested models had errors in their representation of the 400-600m layer in the Southern Ocean of ~1°C. As a result of these large biases, the study suggests future work should exclude outlier models when using the dataset for exploring projections. The multi-model mean bias for the ensemble was -0.31°C though this was spatially variable, with alternating cold and warm biases. The analysis indicated that the largest coastal biases in the Southern Ocean were found in the ASE which were suggested to be associated with inadequate representation of bathymetry which influences the simulated onshore flow of CDW in the ASE.

Deficiencies in CMIP5 model simulations were found to be associated with the coarse resolution of the models. St Laurent et al. (2013) performed a modelling study of CDW routing in the ASE and determined that models require a resolution of <1 km in order to fully recreate the processes involved in routing water onto the continental shelf in the region, concurrent with the conclusion of Little and Urban (2015). This high resolution was particularly important for correctly representing the bathymetry, namely, the troughs through which water is routed toward the ice sheet. Asay-Davis et al. (2017) suggest that CMIP5 are unable to fully resolve topography and therefore coastal processes.

Given the dependence of heat delivery to the ASE on atmospheric and oceanic forcing, representation of large-scale climatological patterns is important given its prominent influence on delivery of water masses to the region. A study by Hosking et al. (2013) explores the ability of CMIP5 models to reproduce the dominant circulation patterns in the Pacific Sector of the Southern Ocean, with a focus on depth and position of the ASL. The study concludes that the majority of the CMIP5 ensemble are unable to fully replicate observations of climate, with statistically significant biases that are systematic. Furthermore, a study by Bracegirdle (2013) who compared model simulations of sea level pressure to the ERA-Interim dataset also come to this conclusion, where most models are simulating weaker than observed westerly winds with an equatorward bias. Bracegirdle (2013) evaluated model

performance of ACC representation using the CMIP5 ensemble and found the representation of the westerly wind jet by the multi-model mean to be shifted toward the equator by 3.3°±1.9°. Given the importance of the ACC and ASL in controlling ocean circulation patterns, inability to simulate these could result in poor representation of on shelf ocean temperatures, and CDW delivery, in the ASE.

2.8. Using Climate Model Projections to Force Ice Sheet Models

Ice sheet modelling began in the early 2000s as a means to understand the dynamic changes observed over the satellite period, recreate the interactions between glaciers and climate and be able to quantify projected changes to ice sheets in the future under a changing climate (Gladstone et al., 2012). Numerical ice sheet models capture the force balance between resistive buttressing and drag and the outward flow dominated by basal sliding, providing a means by which to physically represent fast flowing glaciers and the surrounding inert ice (Favier et al., 2014; Pattyn et al., 2012).

Given the dependence and sensitivity of ice dynamics in response to interaction with climate, applying a climate forcing to an ice sheet model can provide a simulation of potential future changes to an ice stream or region under a changing climate (Cornford et al., 2015). Use of AOGCM projections, such as the CMIP5 ensemble, is beneficial given the association of projections to a particular future emissions scenario. For example, use of the "business as usual" RCP8.5 scenario provides an upper limit on sea level rise estimates when used to force a standalone ice sheet model. Levermann et al. (2014) performed a multi-model comparison using five different ice sheet models (UMISM, PISM, SCIOPOLIS and PennState-3D) with melt rates parameterised from subsurface ocean temperature projections as produced by the CMIP5 ensemble. This parameterisation of melt rate used temperatures simulated at the average depth of the ice shelves in each drainage basin considered, this is around ~300m for the ASE. The investigation also found that the greatest uncertainties in projecting future sea level was that associated with the physical climate system and therefore the climate model output used to parameterise the ice sheet forcing. The investigation projected a range of sea level contributions from the whole of the Antarctic ice sheet of between -0.04 cm to 0.21 cm by 2100.

However, despite the notable advantages of using AOGCM output to force ice sheet models, given the errors discussed in Section 2.7.2, it is evident that there are some uncertainties. Donat-Magnin et al. (2017) discuss the use of the CMIP5 ensemble for parameterising a melt rate with which to apply to a dynamic ice sheet model. Given that the AOGCMs in the CMIP5 ensemble are unable to capture the ice-ocean feedbacks occurring when ocean forced melting occurs beneath the ice shelves,

realistic changes to the properties of coastal waters are not sufficiently captured. Most notably, the input of cold, fresh, meltwater from ice shelves is likely to modify the overall temperature and circulation of the coastal waters that are driving ice melt processes. Thus, models are likely to be overestimating temperature, given that this additional water mass, if modelled, would be acting to cool local ocean temperatures and thus reduce thermal forcing.

2.8.1. BISICLES

Numerical ice sheet models vary substantially in terms of their representation of physics, parameterisations, dimensions and resolutions. For example, the most complex models such as Elmer Ice (Favier et al., 2014), include the full stokes equations, which are of high complexity and thus computationally demanding to solve. In contrast, simple flowline models (Gladstone et al., 2012) simplify the equations by integrating equations, resulting in a 1HD model.

In terms of its complexity, BISICLES lies somewhere in between. BISICLES is based on the vertically integrated flow model described by Schoof and Hindmarsh (2010). The flow model includes longitudinal and lateral stresses, in addition to a simplification of vertical shear stress which is better applied to ice shelves and streams (Cornford et al., 2013; Cornford et al., 2015). The advantages of the model lies with its capability of resolving the grounding line to resolutions of up to 250 m. Due to the adaptive mesh refinement (AMR) grid, BISICLES is able to capture the complex dynamics of fast ice at the grounding line, whilst keeping the resolution of the slow moving ice in the interior, coarse. As forcing is applied to the grounding line, it retreats, and the adaptive mesh grid modifies so that it retains high resolution around the new grounding line position. As a result, the model is a valuable tool for investigating the stability of the grounding line and therefore the occurrence of MISI.

2.8.2. Ice Sheet Modelling of the ASE Using BISICLES

Nias (2017) used the BISICLES ice sheet model to explore ice dynamics in the ASE. The study investigated the sensitivity of the BISICLES ice sheet model to changes in the parameters obtained in the initialisation procedure. An ensemble of parameters were created that described a range of values for the coefficients of ice stiffening and basal traction, and also explored a range of initial basal melt rates. The study proceeds to use this ensemble to project the range in ice response to an additional simplified melt rate forcing (Gladstone et al., 2012) that was calculated from the projected ocean temperature simulated by a regional ocean model (Timmermann et al., 2002; Hellmer, 2004) under the SRES A1B scenario. Findings indicated a range of contributions to global mean SLR that were parameter dependent, with an upper bound of 12 cm by 2100. The investigation focussed on

the model equations and dynamics, exploring the sensitivity within the BISICLES ice sheet model. However, the study proceeded to state that future work exploring the potential range in melt rate forcings, using a range of model projected temperatures, would be the next step to establish a more realistic projection of the future contribution to global sea level rise.

BISICLES was used to project the future evolution of WAIS in a study by Cornford et al. (2015). Cornford et al. (2015) used two projections scenarios described in the IPCC AR4 (Meehl et al., 2007b) which illustrate a modest mitigation scenario (E1) and a balanced scenario (A1B). Their results show an estimated range of between 1.5 to 4.0 cm contribution from the ASE to sea level rise through mass loss between 2000 to 2100. Given the use of two modest mitigation scenarios, the study did not explore the upper bound of projected future climate scenarios. Furthermore, more recent emissions scenarios have since been defined, demonstrating the need to perform a similar investigation using the updated future climate scenarios described in the IPCC AR5 (Collins et al., 2013).

2.9 Summary

With the large observed changes to the marine terminating glaciers in the ASE over the satellite period and the potential for the region to contribute large quantities of mass to global mean SLR, the ASE has become a focal region of interest. As delivery of CDW toward the grounding lines of these glaciers has been identified as the main driver of basal melting and subsequent mass loss in the region, recent studies have looked to use observations and models to understand the climatological controls of this heat delivery. Whilst the exact mechanism of upwelling of warm water onto the shelf is not yet known, it is well documented that that patterns of atmospheric circulation, namely westerly winds along the coast, are partially responsible for this heat delivery.

Investigations into the performance of the CMIP5 ensemble to reproduce climate in the Southern Ocean have been carried out, the majority of which indicate biases in the position of the ACC and subsequent dominant winds which have in turn influenced representation of other climate variables. Furthermore, the coarse resolution of AOGCMs has hindered capabilities of representing small scale processes that ultimately influence representation of the regional climate in the ASE. Considering these biases, the use of climate model output to force ice sheet models of the ASE should be put under a certain amount of scrutiny.

The BISICLES ice sheet model was used to explore the parameter uncertainty when simulating the dynamics of the ASE (Nias, 2017). The model's adaptive mesh grid ensures the model resolution is

sufficient to capture the complex dynamics of the grounding line, whilst ensuring coarse resolution in slower flowing regions of ice in order to keep the computational expense low. Using projected temperatures from CMIP5 models to force BISICLES over the ASE will provide a means by which to explore projected evolution of the region, including grounding line retreat and change in VAF, whilst relating these projections of temperature back to physical features of climate captured in the models.

Chapter 3 : Evaluation of the CMIP5 Ensemble

3.1. Introduction

Assessing model performance is an important component of numerical modelling. The evaluation of models against observational data provides a means for assessing their ability to reproduce observed climate in the past; which can be used to indicate how well a model might reproduce patterns of climate in the future.

This chapter aims to identify specific models within the 27-member CMIP5 ensemble that are best able to capture the observed ocean potential temperature from 1929 to 2016 in the Southern Ocean. This will be primarily assessed using both the root mean square error (RMSE) and mean bias error (MBE). The six best performing models will be identified and their simulations of ocean temperature over the Southern Ocean will be explored. Finally, the chapter will explore ocean temperature averaged over the ASE, simulated by the subset of six best models.

3.2. Data and Methodology

3.2.1. Observational Data

This investigation has used the Hadley Centre EN4.2.1 dataset (downloaded on 08/02/2018; Good et al. 2013) of monthly ocean potential temperature over the period from January 1979 to December 2016. Potential temperature as opposed to *in situ* temperature, was used as it accounts for the change in pressure that occurs with depth. All references to temperature will therefore describe potential temperature. Analysis is restricted to ocean temperature south of 30°S, to describe the Southern Ocean. The resultant dataset consists of 1,326,942 observations of temperature, which will be referred to henceforth as profiles. Each profile, measured during a given month, has a specific longitude, latitude, and range of depths at which temperatures were measured. Depths range from 0-5000m, and number of corresponding depth levels, up to 400.

The data were corrected for biases using the Gouretski and Reseghetti (2010) corrections. Furthermore, upon measurement, each profile is given a quality score (QC flag) from 1 to 4; where 1 is high quality and 4 is low quality. These QC flags were downloaded and subsequently profiles with a score of 4 were nullified. This ensures biased, unreliable profiles were removed from the dataset.

3.2.2. CMIP5 Ensemble

Output from a total of 27 CMIP5 models were used in this study (table 1) which were downloaded and interpolated onto 1°x1° grid, accounting for the curvature of the earth. Interpolation was performed to provide direct comparability between the models given the difference in curvilinear grids across the ensemble. Monthly ocean potential temperature output from the CMIP5 r1i1p1 simulations was analysed over the period from January 1979 to December 2016. Using the r1i1p1 ensemble of simulations ensures that all the models are consistent in their initial conditions, initialization methods and perturbed physics.

Given that the CMIP5 experiments for the historical period end in December 2005, model projections were added to the historical data from January 2006 to December 2016 to make up the period over which the models will be assessed. As a result of this addition, the assessment period from 1979 to 2016 will be referred to as the "observational period" given that it describes a combination of the CMIP5 historical experiments and projections. Both RCP2.6 and RCP8.5 will be used to make up the last decade of the observational period and compared to determine whether choice of forcing scenario impacts the model performance when evaluated against observations.

Of the 50 available models in the CMIP5 ensemble, 27 have performed experiments forced with both the RCP2.6 and RCP8.5 scenarios, where the former represents a scenario involving mitigation of climate change whilst the latter describes an extreme "business as usual" scenario. Given that this investigation is interested in the range of modelled temperature projections, it was deemed appropriate to limit to analysis of models to those which have performed, and thus have available output for, both of these experiments.

3.2.3. Summary of Methods

1. Downloaded Hadley Centre EN4 ocean potential temperature data from 1979-2016 for latitudes South of 30°S and read into Matlab
2. Downloaded, and read into Matlab, 27-CMIP5 modelled monthly ocean potential temperature outputs for the historical period (1979-2005) and the projection period (2006-2100) for RCP2.6 and RCP8.5, for latitudes South of 30°S

For each of the 27 CMIP5 models:

3. Combined model data for the historical period of 1979 to 2005 with the first decade of projections from 2006 to 2016 (using both RCPs) to make up the "observational period"
4. Interpolated modelled potential ocean temperature output onto 1°x1° grid over the observational period
5. For the month of each observational measurement, interpolated modelled ocean potential temperature output to the specific latitude and longitude of that observation
6. Interpolated modelled ocean potential temperature output to specific depth of each observation
7. Calculate RMSE and MBE compared with the observed ocean potential temperature over the observational period

Table 3.1: *Summary of the 27 CMIP5 models used in this investigation*

Model Number	Modelling Centre	Model Code
3	Beijing Climate Centre, China Meteorological Administration	bcc-csm1-1
4	Beijing Climate Centre, China Meteorological Administration	bcc-csm1-1-m
7	Canadian Centre for Climate Modelling and Analysis	CanESM2
8	Canadian Centre for Climate Modelling and Analysis	CCSM4
11	Community Earth System Model Contributors	CESM1-CAM5
18	Centre National de Recherches Météorologiques / Centre Européen de Recherche et Formation Avancée en Calcul Scientifique	CNRM- CM5
19	Commonwealth Scientific and Industrial Research Organisation in collaboration with Queensland Climate Change Centre of Excellence	CSIRO-Mk3-6-0
21	LASG, Institute of Atmospheric Physics, Chinese Academy of Sciences and CESS,Tsinghua University	FGOALS-g2
22	LASG, Institute of Atmospheric Physics, Chinese Academy of Sciences	FGOALS-s2
23	The First Institute of Oceanography, SOA, China	FIO-ESM
25	NOAA Geophysical Fluid Dynamics Laboratory	GFDL-CM3
26	NOAA Geophysical Fluid Dynamics Laboratory	GFDL-ESM2G
27	NOAA Geophysical Fluid Dynamics Laboratory	GFDL-ESM2M
29	NASA Goddard Institute for Space Studies	GISS-E2-H
31	NASA Goddard Institute for Space Studies	GISS-E2-R
33	National Institute of Meteorological Research/Korea Meteorological Administration	HadGEM2-AO
35	Met Office Hadley Centre	HadGEM2-ES
37	Institut Pierre-Simon Laplace	IPSL- CM5A-LR
38	Institut Pierre-Simon Laplace	IPSL- CM5A-MR
41	Atmosphere and Ocean Research Institute (The University of Tokyo), National Institute for Environmental Studies, and Japan Agency for Marine-Earth Science and Technology	MIROC5
42	Japan Agency for Marine Earth Science and Technology, Atmosphere and Ocean Research Institute (The University of Tokyo) and National Institute for Environmental Studies	MIROC-ESM-CHEM
43	Japan Agency for Marine Earth Science and Technology, Atmosphere and Ocean Research Institute (The University of Tokyo) and National Institute for Environmental Studies	MIROC-ESM
44	Max Planck Institute	MPI-ESM-LR
45	Max Planck Institute	MPI-ESM-MR
47	Meteorological Research Institute	MRI-CGCM3
49	Norwegian Climate Centre	NorESM1-ME
50	Norwegian Climate Centre	NorESM1-M

3.2.4. Model Assessment

All data was read into and analysed using the software MatLab version 2017a. In order to make a direct assessment of the model output to observational data, bilinear interpolation of the gridded model output onto the location of the observational dataset was performed, providing the modelled equivalent of each *in situ* temperature profile. Bilinear interpolation was used given the smoothness of the model data.

Each CMIP5 model in the ensemble consists of differing number of depth levels that are defined over different depths. To account for these differences between models, and allow for more direct comparison with observations, the model depths have also been interpolated to the depths of the observations. This provides uniformity across the models and ensures that the differing resolutions of models, both horizontally and vertically, are not influencing the model-observation comparison.

Root mean square error (RMSE) was calculated (eq. 1) between the model simulation and observational data which provided a single metric to assess model performance (Glecker et al., 2008; Naughten et al., 2018)

$$\boldsymbol{RMSE} = \sqrt{\frac{\sum_{i=1}^{N}(\boldsymbol{m_i} - \boldsymbol{o_i})^2}{\boldsymbol{N}}} \quad (1)$$

where m_i and o_i describe the modelled and observed ocean potential temperature, respectively, and N denotes the overall number of temperature measurements.

As RMSE provides no indication as to the sign of the biases, the mean bias error (MBE) was also calculated and used as a supplementary analysis metric

$$MBE = \frac{\sum_{i=1}^{N}(m_i - o_i)}{N} . \quad (2)$$

The magnitude of the errors captured by these metrics are expected to vary, given that the squaring function in the RMSE calculation will act to punish models with large biases to a greater extent than in the MBE calculation.

3.2.5. Area Mean Maps

Time mean, depth-averaged maps of RMSE and MBE were used in order to explore the spatial patterns of the biases and errors. To obtain these maps, RMSE and MBE were calculated for each specific profile which, given that these profiles have associated locational data, were binned into 1x1° grid cells and averaged. The resulting values are therefore averaged over all depths and all months in the observational period.

For each of the 27 CMIP5 models:

1. Calculate RMSE and MBE for each profile of ocean potential temperature against observations from 1979-2016
2. Average the RMSE and MBE calculated for each profile over 1°x1° grid cells
3. Use averaged RMSE and MBE to produce maps showing the patterns of errors

Given the irregular distribution of profiles across the Southern Ocean, maps created through the binning of RMSEs into grid cells do not necessarily reflect the overall RMSE calculated for each model (see model 47 for example). Should two grid cells have high RMSE values, one may contain a single profile whilst the other grid cell may contain many. Furthermore, patterns represented in these maps are likely to be distorted as a result of the latitudinally differing grid cell sizes, given the curvature of the earth. Therefore, as a more robust metric, the overall RMSE was used to determine the highest performing models and the plots of area mean RMSE and MBE are included to give an indication of the pattern of the biases for each model as opposed to describing the magnitude of these errors.

3.2.6. Identifying the Best Performing Models

The mean of the RMSE values for the two RCP scenarios was be used to determine the subset of best performing models, identified as those with the lowest errors. Six models were chosen as a sample size sufficient to capture some of the variability between models that could be covered in suitable detail.

Whilst studies have suggested that the multi-model ensemble mean, or weighted mean provide the most reliable projection data (Bracegirdle et al., 2008), this will not be performed as this investigation aims to attribute changes in ice sheet evolution to the physical climate simulated by each model. Furthermore, the study aims to explore the range in projections simulated by the models as a way of investigating the importance of model selection for making estimates of future climate.

3.2.7. Exploring temperature over the 400-700m layer

For each CMIP5 model, potential temperature interpolated to, and averaged over, the 400-700 m layer was performed for South of 30°S for modelled data over the period 1979-2016. Given that the historical period simulated by the CMIP5 models ends in 2005, RCP8.5 projections from 2006-2016 were added to make up the period.

3.3. Results: Model Evaluation

3.3.1. Observations

The patterns of whole ocean depth-averaged observed ocean temperature in the Southern Ocean, averaged over the observational period, illustrates the coldest temperatures along the coast which increase equatorward ranging from -1.5 to 4^{o}C (fig 3.1). Potential temperatures well below freezing, below -1.5^{o}C, reside along coast. Temperatures exceeding 4^{o}C surround the cooler temperatures around the continent, these warm temperatures are likely representative of the ACC. The warm band of temperatures lie closest to the ice sheet in the Pacific Sector of the Southern Ocean at 60^{o}S.

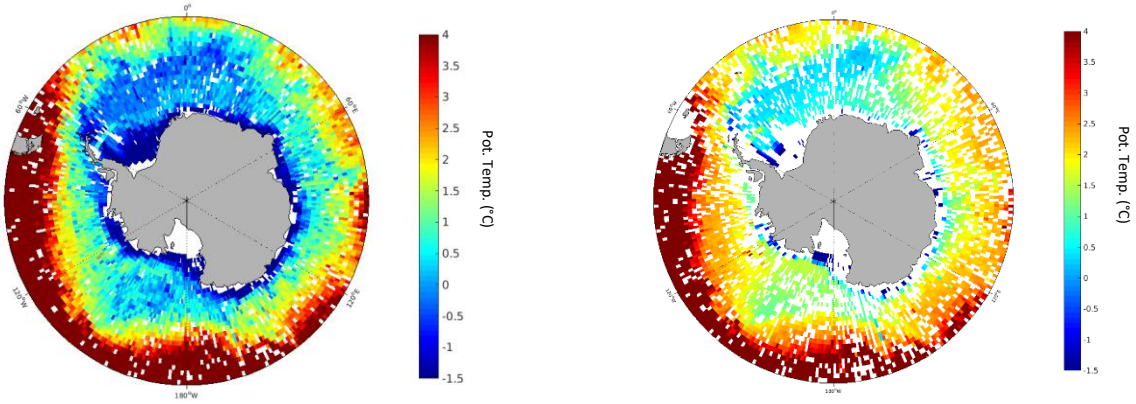

Figure 3.1: *Observed ocean potential temperature in the Southern Ocean averaged over 1979-2016. Depth averaged over all depths (left) and 400-700 m (right).*

The sparsity of the observational data is evident in the two maps (fig. 3.1), where white spaces indicate regions without any observations. No observations beneath the Filchner-Ronne and Ross ice shelves are evident in addition to a spattering of no data across the Southern Ocean. Over the 400-700m layer the lack of data is more prominent, compared with depth averaged temperature observations. There are fewer observations over this layer, particularly lacking around the coast of the ice sheet. However, regions of no data around the coast could be associated with the presence of continental topography.

3.3.2. Model Assessment

This section will present the results from the comparison between observed ocean potential temperature averaged over all depths, from the EN4 dataset over the period 1979-2016 and the output from the CMIP5 ensemble.

3.3.2.1. RMSE

The ensemble exhibits a spread of RMSE values for all profiles over the observational period (fig. 3.2). For both RCP scenarios forcing the years 2006-2016, the models with the lowest and highest RMSE scores are consistent (table 3.2). The model with the lowest RMSE being NorESM1-ME (49) of 1.66°C and the highest being GISS-E2-R with an RMSE of 2.47°C. The range of 0.95°C demonstrates that there is a difference in the performance of models within the ensemble.

There is a strong positive correlation between the RMSE for each model with the addition of both RCP8.5 against RCP2.6 (fig 3.2), with an R^2 of 0.99 indicating that choice of forcing scenario for the last decade of the observational period has little influence on the RMSE metric.

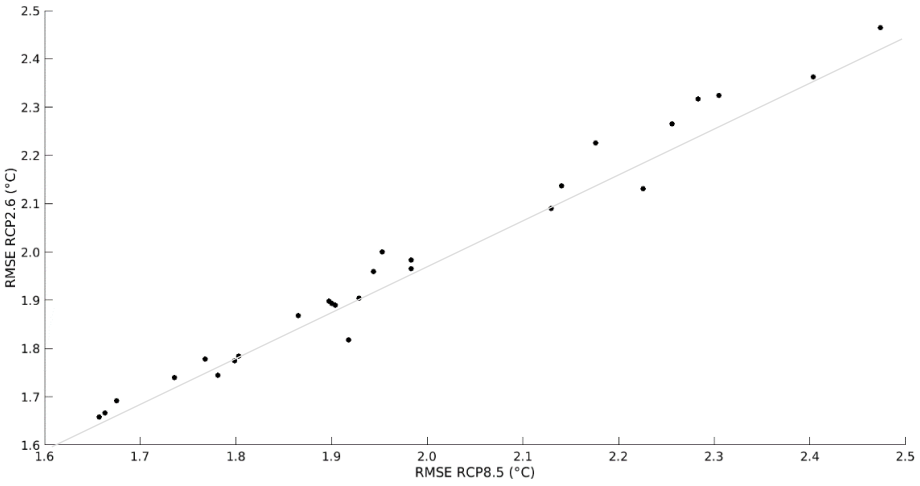

Figure 3.2: *Correlation between 27 CMIP5 model RMSE of ocean temperature calculated over the Southern Ocean from 1979-2016 using projections of RCP 2.6 versus RCP8.5 for the period of 2006-2016.*

Furthermore, the distribution of RMSEs across the 27-member ensemble is roughly normally distributed (fig 3.3), again indicating that there is no significant difference in the two sets of RMSE scores for each scenario. Overall the median RMSE remains at ~2°C for both scenarios and the range of the data for both scenarios lies between 1.6 to 2.5^{o}C

Table 3.2: *Table of modelled ocean temperature RMSE values calculated over the observational period by 27 CMIP5 models. Metrics were calculated using projected ocean temperature from both the RCP2.6 and RCP8.5 scenarios over the period from 2005-2016. The rank of each score has been given where 1 is the lowest RMSE and 27 is the highest. Red denotes the six best models with the lowest RMSEs.*

Model Number	RMSE for RCP2.6 (°C)	RANK	RMSE for RCP8.5 (°C)	RANK	MEAN RMSE (°C)	RANK
49	1.66	1	1.66	1	1.66	1
7	1.67	2	1.66	2	1.66	2
11	1.69	3	1.68	3	1.68	3
8	1.74	4	1.74	4	1.74	4
47	1.74	5	1.78	6	1.76	5
3	1.78	7	1.77	5	1.77	6
4	1.77	6	1.80	7	1.79	7
50	1.78	8	1.80	8	1.79	8
26	1.87	10	1.86	9	1.87	9
23	1.82	9	1.92	13	1.87	10
35	1.89	11	1.90	12	1.90	11
22	1.89	12	1.90	11	1.90	12
25	1.90	13	1.90	10	1.90	13
27	1.90	14	1.93	14	1.92	14
18	1.96	15	1.94	15	1.95	15
33	1.97	16	1.98	18	1.97	16
42	2.00	18	1.95	16	1.98	17
43	1.98	17	1.98	17	1.98	18
41	2.09	19	2.13	19	2.11	19
45	2.14	21	2.14	20	2.14	20
19	2.13	20	2.23	22	2.18	21
21	2.23	22	2.18	21	2.20	22
38	2.27	23	2.26	23	2.26	23
31	2.32	24	2.28	24	2.30	24
44	2.32	25	2.31	25	2.31	25
37	2.36	26	2.40	26	2.38	26
29	2.46	27	2.47	27	2.47	27

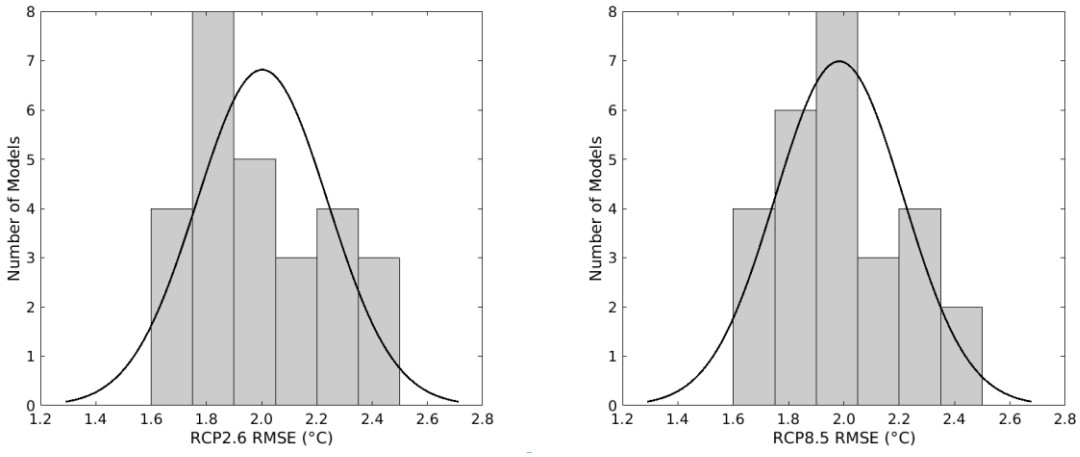

Figure 3.3: *Distribution of 27 CMIP5 RMSE of modelled ocean potential temperature over the period 1979-2016 in the Southern Ocean. RMSE calculated using both RCP2.6 (left) and RCP8.5 (right) for the period 2006 to 2016.*

Area mean RMSE maps indicate the differences in the distribution of errors simulated by each model (fig. 3.4). There are a range of patterns exhibited by the 27 CMIP5 models with some similarities. GISS-E2-R (29) simulates errors exceeding 2.5°C over a considerable portion of the domain which is consistent with the large RMSE metric of 2.47°C. In contrast, model NorESM1-ME (49) has the lowest RMSE metric of 1.66°C and the pattern of errors indicates the majority of the Southern Ocean to simulate errors of below 1°C, with bands of higher errors along the coast of the West Antarctic and in the central Pacific sector at 30°S.

Of the six best performing models, with the lowest RMSEs, the distribution of errors is generally consistent, with the exception of MRI-CGCM3. The models are producing patterns of low RMSEs of between 0.5-1.0°C over much of the domain with some regions of larger errors up to 2.5°C at lower latitudes around 30°S. For bcc-csm1-1, CanESM2, CCSM4 and NorESM1-ME the concentration of highest errors reside around 180°W. This is also exhibited in CESM1-CAM5 with the addition of large errors over 2.5°C stretching east from around 10°E to 120°E at 30°S. In contrast, MRI-CGCM3 has a region of high bias exceeding 2.5°C along the coast of WAIS, stretching north into the Pacific Ocean. Further, the model simulates a region of equally high error from the tip of the Antarctic Peninsula through Drakes passage and to the east of South America.

Considering the representation of the ASE for the six best models indicates that whilst bcc-csm1-1, CanESM2, CCESM4, CESM1-CAM5 and NorESM1-ME appear to have low RMSE in the ASE averaged over all depths, compared with the other models in the ensemble. In contrast, there is a local region of large RMSE in MRI-CGCM3.

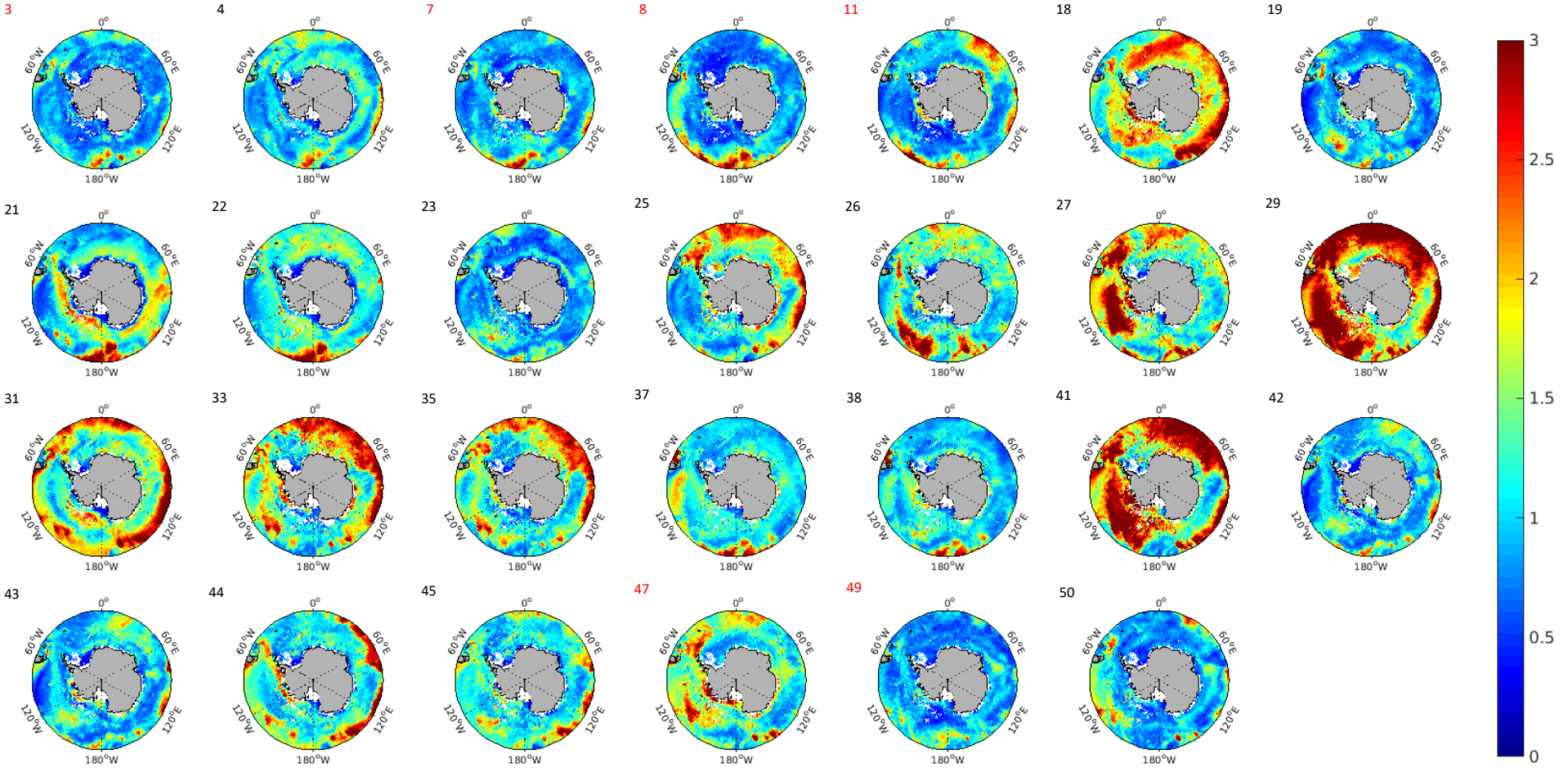

Figure 3.4: *Pattern of time mean depth average RMSE of modelled ocean potential temperature in the Southern Ocean. Each map shows the pattern of errors for each of the 27 CMIP5 models over the period 1979-2016. Historical model output is used from 1979-2005 and RCP8.5 is used for the period 2006-2016. Red numbers highlight the best performing models.*

3.3.2.2. MBE

The majority of models exhibit positive MBEs indicating that models are overestimating the temperatures in the Southern Ocean (fig. 3.5). Where cold biases exist, these are mostly located around 180^{o}W. This is evident in the pattern of errors for bcc-csm1-1-m, where the negative MBE extends longitudinally from 180°W at 30°S. The models with overall negative MBEs are FGOALS-g2 (21), FGOALS-s2 (22), FIO-ESM (23) and GDFL-ESM2M (27), these models are therefore underestimating observed temperatures.

Considering the ASE exclusively, it appears that all six models in the subset of best performing models have regions of positive MBE. Whilst the bcc-csm1-1 MBE appears to be below ~0.5°C., the remaining five models indicate larger positive errors, thus warm biases, ranging up to 2°C. The model with the greatest ASE positive MBE is MRI-CGCM3.

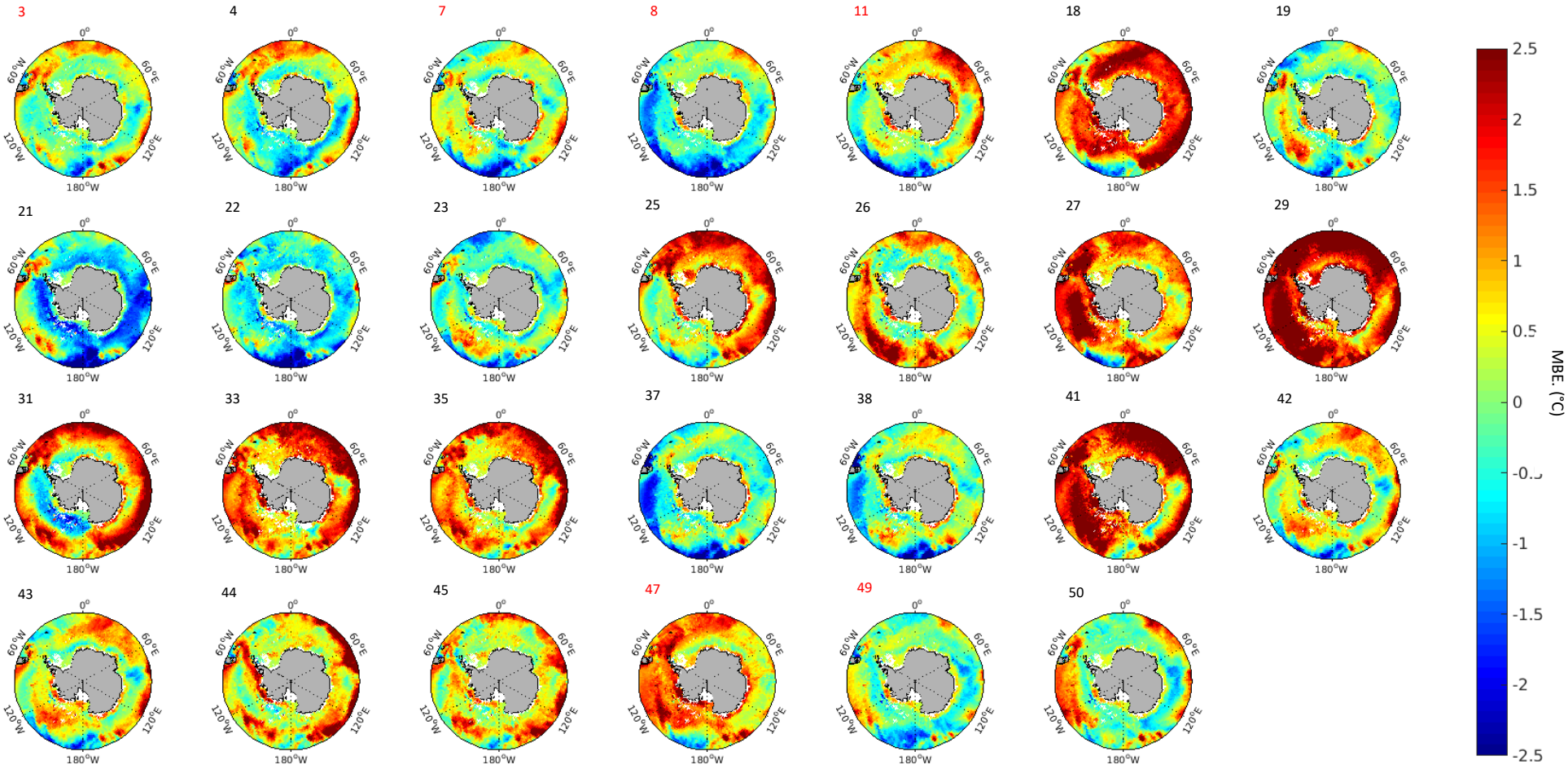

Figure 3.5: *Pattern of time mean depth average MBE of modelled ocean potential temperature in the Southern Ocean. Each map shows the pattern of errors for each of the 27 CMIP5 models over the period 1979-2016. Historical model output is used from 1979-2005 and RCP8.5 is used for the period 2006-2016. Red numbers highlight the best performing models.*

The six best performing models are consistent in their sign and magnitude of the pattern of MBEs over the Southern Ocean. With the exception of MRI-CGCM3, the best performing models overestimate temperatures by 0.5°C over most of the Southern Ocean. The MBEs that were observed around 180°W, in the top six models, are cold biased by -2°C which are present in all of the model simulations. MRI-CGCM3 has a positive MBE over much of the domain exceeding 1°C over the Pacific and Atlantic sectors of the Southern Ocean, with an overestimation exceeding 2.5°C in the ASE. MRI-CGCM3 is the most different of all the models. Models CESM1-CAM5 and MRI-CGCM3 also show a coastal MBEs of >1°C along the east Antarctic coast.

Similarly to the distribution of RMSEs (fig 3.3), the spread of MBE is the same for both scenarios and the median bias lies around 0.5°C (fig. 3.6). The slight shift of the central tendency indicates a greater number of models with positive biases, thus, on average, models are overestimating temperature.

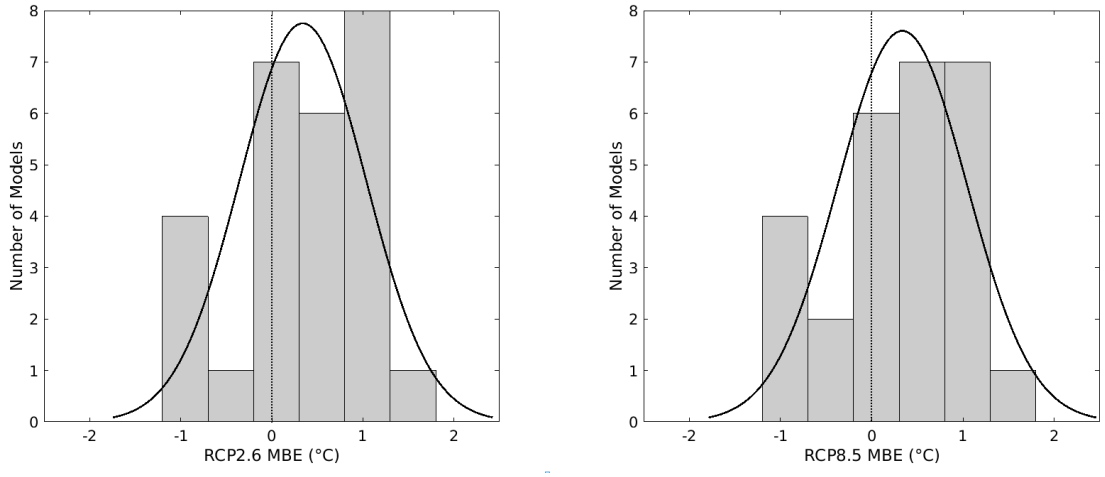

Figure 3.6: *Distribution of 27 CMIP5 MBE of modelled ocean potential temperature over the period 1979-2016 in the Southern Ocean. RMSE calculated using both RCP2.6 (left) and RCP8.5 (right) for the period 2006 to 2016.*

The MBE for the entire Southern Ocean confirms that the majority of models in the subset of best performing models are overestimating ocean temperature, with the exception of CanESM2 which underestimates temperatures by 0.17^{o}C over the observational period (table 3.3). The magnitude of MBE is inconsistent with the RMSE for each model.

Table 3.3*: MBE of modelled ocean temperature Southern Ocean from 1979-201, for the six best models identified with the lowest RMSEs. for the six best performing models for their projections over the observational period compared against observations. MBE has been calculated using RCP2.6 and RCP8.5 projections for the period from 2006 to 2016.*

	MBE (°C)	
Model Name	**RCP2.6**	**RCP8.5**
bcc-csm1-1	0.61	0.55
CanESM2	-0.17	-0.16
CCSM4	0.11	0.15
CESM1-CAM5	0.05	0.01
MRI-CGCM3	0.80	0.85
NorESM1-ME	0.21	0.28

3.3.3. Summary

There is a large range in the RMSE scores across the ensemble, with the mean scenario RMSE for each model ranging from 1.66^{o}C to 2.47^{o}C. Performance is generally consistent across both RCPs for each model. The majority of models appear to be positively biased, as indicated by their MBE. This is supported by the maps of MBE where most of the domain shows a red, warm bias of temperature. This indicates that models are overpredicting temperature in the Southern Ocean.

The six models with the lowest RMSEs for both the RCP2.6 and RCP8.5 scenarios are bcc-csm1-1, CanESM2, CCSM2, CESM1-CAM5, MRI-CGCM3 and NorESM1-ME. These models will be the focus of Section 3.4 and Chapter 4.

3.4 Results: Model Simulations

This section will explore the mean ocean temperature projected by each of the six best performing models over the observational period, from 1979 to 2016, averaged over the 400–700 m layer. The 400-700m layer was identified as the depth at which temperatures on shelf in the ASE reside, which is the main focus of this investigation. Temperatures on shelf in the ASE will also be considered, in comparison to observations.

3.4.1. Southern Ocean 400-700m Layer

The models reproduce the general overall pattern of temperature in the Southern Ocean (fig 3.7), consistent with observations (fig. 3.1), with the lowest temperatures closest to the ice sheet and increase with increasing distance from the continent. The warm band of temperatures at low latitudes, associated with the ACC, is simulated by all the models but the southernmost reach of this varies, with models MRI-CGCM3 and CanESM2 simulating the current in the Pacific sector to be closer to the coast than CCSM4. The three most similar outputs of ocean temperature over this layer are simulated by models CCSM4, CESM1-CAM5 and NorESM1-ME.

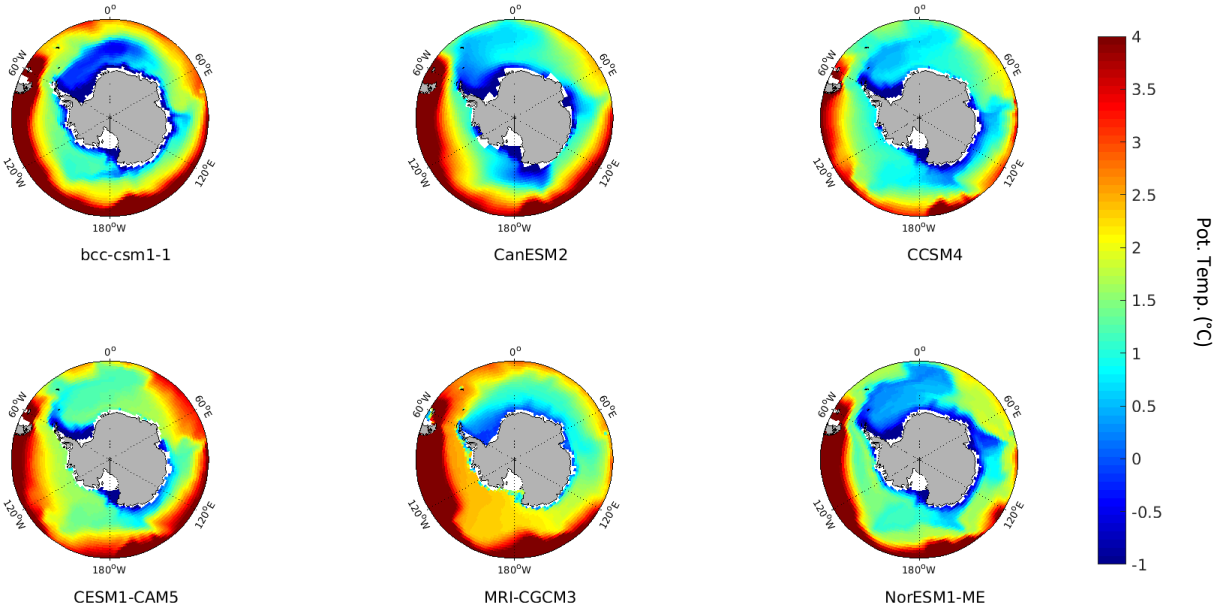

Figure 3.7: *Patterns of 400-700 m depth averaged ocean potential temperature in the Southern Ocean over the period 1979-2016, as simulated by a subset of CMIP5 ensemble members. Projections forced with the RCP8.5 scenario were added to make up the last decade of the observational period (2006-2016).*

Below freezing temperatures are simulated around the coast of Antarctica by all models, to varying extents. The lowest simulated temperatures of below -1.5°C are concentrated in the Weddell Sea. In bcc-csm1-1, CanESM2 and NorESM1-ME these cold waters are present along the entire coast uninterrupted by warmer waters. CCSM4 and CESM1-CAM5 simulate the below freezing

temperatures extending north from the Weddell and Ross Seas however the coasts of the west of the East Antarctic Ice Sheet (EAIS) and WAIS are exposed to temperatures above freezing in the 400-700m layer. MRI-CGCM3 shows a different pattern. With freezing temperatures extending from the Weddell Sea eastward but WAIS is exposed to warmer temperatures up to 2.5°C and the eastern coast of the EAIS showing temperatures around ~0.5°C.

Temperatures local to the ASE vary according to model. Models bcc-csm1-1 and CanESM2 indicate the coldest temperatures in the region of ~-1°C. CCSM4 and NorESM1-ME which also show temperatures on shelf to be below freezing, but their area covers a lesser extent than bcc-csm1-1 and CanESM2. In contrast, CESM1-CAM5 and MRI-CGCM3 indicate local temperatures in the ASE to be ~1.5°C and ~2.5°C in the region, which is a similar temperature to the surrounding Pacific Ocean.

3.4.2. Amundsen Sea

To explore modelled and observed ocean temperatures on shelf in the ASE, temperatures were averaged over the 400-700m layer from 103-113°W and 72-75°S, accounting for the curvature of the earth. Given that this investigation is interested in temperature forcing on shelf in the ASE, zonal mean ocean temperature within this region was computed over the observational period (fig. 3.8). There is a large range in the temperatures simulated, with the highest modelled temperature as 2°C on shelf by MRI-CGCM3 compared with that which fluctuates below freezing, to ~-0.5°C, as simulated by CanESM2 and bcc-csm1-1.

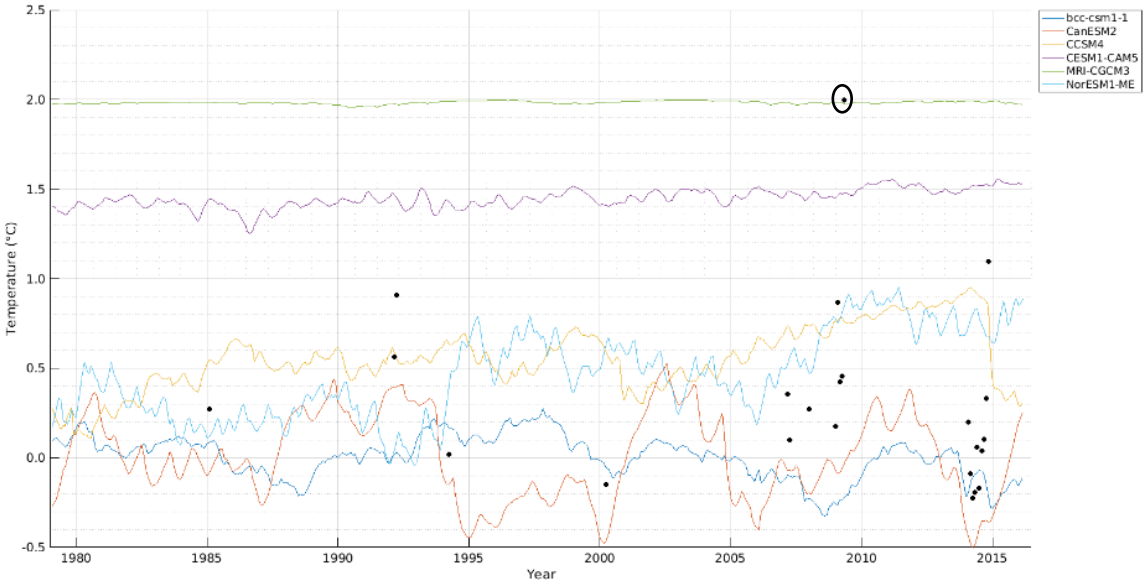

Figure 3.8: *Modelled ocean potential temperature in the Amundsen Sea Embayment averaged over the 400-700m layer from 1979-2016. Black points show mean observed temperature for the ASE 400-700 m layer, circle indicates an outlier. Ocean temperature forced with RCP8.5 was used for the last decade of the observational period (2006-2016).*

There are clear differences between the models in terms of both their mean temperatures and variability. Models with the greatest mean temperatures, namely MRI-CGCM3 and CESM1-CAM5, have the lowest residual variability of 0.01°C and 0.04°C respectively. In contrast, models with the lowest mean temperatures have the greatest variability, this is most clear for CCSM4 with a mean of 0.001°C and variability of 0.24°C.

The subset of models are roughly able to capture mean observed temperature, 0.25°C, in the ASE averaged over the observational period. Models bcc-csm1-1, CanESM2, CCSM4 and NorESM1-ME produce similar mean temperatures over the observational period (fig. 3.9), with mean temperatures of 0.002°C, 0.002°C, 0.54°C and 0.46°C respectively. No model is able to capture the magnitude of the 0.36°C variability in temperature that is observed.

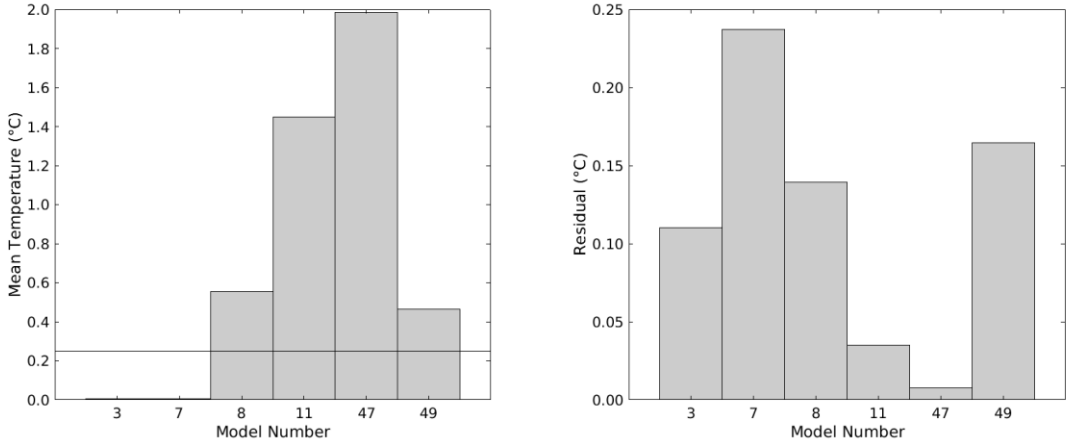

Figure 3.9: *Mean ocean potential temperature in the Amundsen Sea over observational period (1979-2016) for each CMIP5 model in the high performing subset (left) and the mean variability (standard deviation) of the temperature over the period for each model (right). The line in the left figure is the observational mean temperature (0.25°C). The observed residual has also been calculated as 0.36°C which exceeds the figure axis range. Both observational statistics calculated exclude the outlier in fig. 3.10.*

3.4.2.1. ASE Temperature Trends over the Observational Period

With the addition of RCP8.5 for the last decade of the observational period, there is a range in the decadal temperature change values from -0.05°C decade^{-1} produced by bcc-csm1-1 to a trend of 0.17°C decade^{-1} for NorESM1-ME (fig 3.10). For RCP2.6 the temperature is modelled to change by of -0.02°C decade^{-1} by bcc-csm1-1 to 0.15°C, again modelled by NorESM1-ME. All trends are statistically significant with the exception of CanESM2(7) which had a p-value of 0.3.

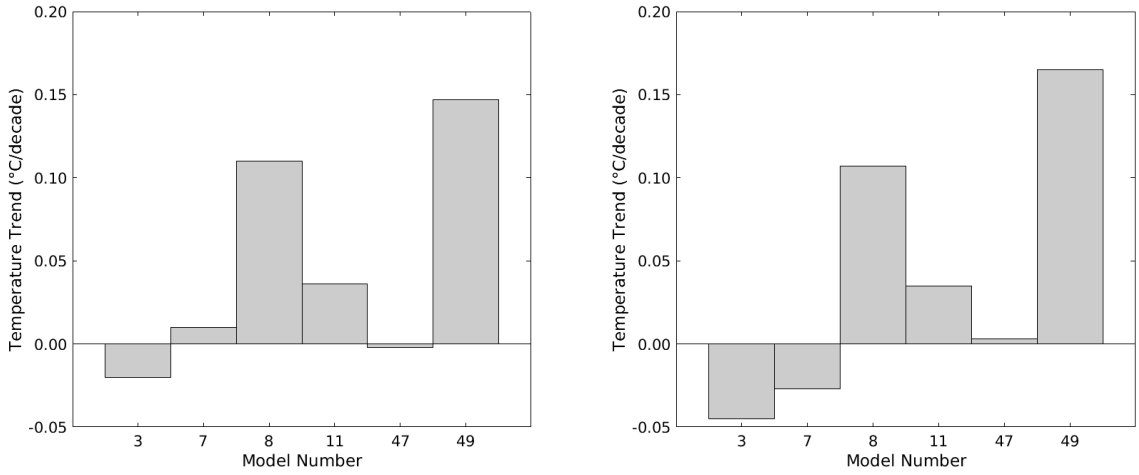

Figure 3.10: *Decadal ocean potential temperature change obtained from CMIP5 modelled temperature change over the ASE 400-700m layer during the historical period, produced by each of the CMIP5 subset under the RCP2.6 (left) and RCP8.5 (right) scenarios.*

3.4.3. Summary

The simulated temperature over the observational period is consistent across the six-best performing CMIP5 models, though the greatest difference is produced by MRI-CGCM3. Models differ in their latitudinal reach of the temperatures of ocean masses associated with the ACC, with CCSM4 and CESM1-CAM5 positioned more equatorward than the remaining models. Furthermore, the extent of the cold waters surrounding the coast vary, with the largest area of below freezing water in the Ross and Weddell Seas, that stretch around the coast, simulated by bcc-csm1-1 and CanESM2. This contrasts with CESM1-CAM5 and MRI-CGCM3 which indicate warm temperatures over much of the Pacific, stretching up to the coast of WAIS. In the ASE, models bcc-csm1-1, CanESM2, CCSM4 and NorESM1-ME best capture the mean temperature of 0.25°C observed on shelf. No model is able to capture the large observed variability in temperature. Poor spatial coverage and extent of observations limits the comparison.

3.5 Assessment of Sampling

Model assessment is limited by the restriction of data comparison to *in situ* observational profiles. In order to assess this, the ocean temperature profiles simulated by each of the 27 CMIP5 models for the 400-700m layer were binned into grid cells between 30-75°S and averaged over time, this is the average temperature of the sampled model output. This sampled mean temperature was compared with the un-sampled modelled 1x1° CMIP5 output of temperature over the 400-700m layer. The unsampled model output was calculated by simply averaging temperature over the whole Southern Ocean below 30°C, averaged over the historical period. Both averages account for the curvature of

the earth. All models indicate that the mean temperature of the Southern Ocean during the observational period is significantly higher for the sampled data than that for the unsampled data, indicating that analysis is biased by the sampling of observational data.

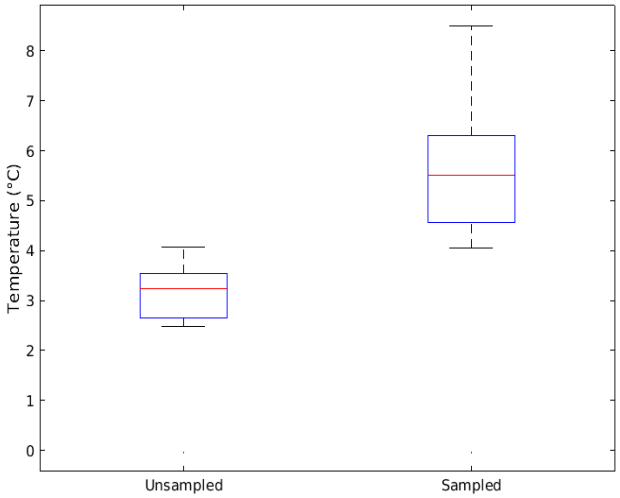

Figure 3.11: *Modelled mean potential ocean temperature during the observational period (1979-2016), averaged over the Southern Ocean 400-700m layer. Unsampled average is calculated as the mean of all grid cells where there is modelled data. Sampled average represents modelled temperature averaged over grid cells only where there are observations.*

3.6. Discussion

The comparison of ocean temperature simulated by 27 CMIP5 models over the period 1979-2016 indicates large RMSEs between 1.66-2.47°C (fig. 3.3), where the majority of the models exhibit a positive, warm bias over the Southern Ocean. The 0.95°C range in RMSE values indicate that there is an inconsistency in model performance across the ensemble, where some models better reproduce observed temperature than others. Model discrepancies are predominantly associated with a combination of the differing representations of physical processes, the way in which models capture natural and internal variability within the climate system and the uncertainty in the scenarios used for the model experiments (Weigel et al., 2010; Taylor et al., 2012). Given that each model differs so widely on these features, it is challenging to characterise what is causing these discrepancies. Furthermore, full analysis of performance is beyond the scope of this investigation.

Generally, the models have warm temperature biases over much of the Southern Ocean, as indicated by the large regions of positive MBE (fig. 3.4), this is consistent with previous studies (Sallée et al., 2013; Naughten et al., 2018). Temperature biases can be associated with multiple factors including for example the representation of the ocean density and freshness in addition to circulation driven mixing that occurs (Sallée et al., 2013). Thus, it is challenging from considering the ocean temperature errors alone to determine causes of this. Large cold errors at low latitudes could potentially be attributable to the misrepresentation, in an 3.3° equatorward bias, of the ACC position (Bracegirdle et al., 2013; Meijers et al., 2015). However, it is difficult to make any conclusions given the lack of additional variables. Other potential influences could include errors associated with simulation of the ASL, which can influence ocean circulation and thus heat delivery throughout the Pacific Sector of the Southern Ocean (Hosking et al., 2013).

Coastal biases, however, can be linked to the exclusion of a representation of ice shelves in the CMIP5 ensemble (Naughten et al., 2018; Donat-Magnin et al., 2017) which would likely hinder model performance of reproducing observations of ocean temperature. The magnitude of the positive, warm, biases in the ASE would indicate that models are overestimating temperature, likely as a result of the lack of input of additional cold, fresh, melt water from ice shelves which would be acting to cool local ocean temperature and modify sub shelf circulation (Donat-Magnin et al., 2017). The presence of ASE errors are evident in a considerable number of models, with errors in this region appearing to exceed all other coastal regions, would support the attribution of errors to lack of ice shelves, given that present melt rates in the ASE exceed all other Antarctic ice shelves (Pritchard et

al., 2012). Therefore, the absence of this feature is likely to have the greatest impact on local temperatures, causing the greatest coastal model errors.

Comparing maps of ocean temperature errors (fig. 3.3 and fig. 3.4) with modelled temperature on shelf in the ASE (fig. 3.8) reveals that the majority of models are indicating overestimations of temperatures on shelf, with the exception of bcc-csm1-1 and CanESM2; which are consistent with the maps of MBE and RMSE. Though collectively the subset of models capture the range in temperatures observed on shelf well, no single model is able to fully replicate the magnitude and timings of the observed variability of on shelf temperature (Asay-Davis et al., 2017; Arthern and Williams, 2017). Given the complex atmospheric, oceanic and topographic controls on CDW delivery to the ASE, it is likely that these coarse resolution models are unable to capture fully the observed coastal processes (Little and Urban, 2015; St-Laurent et al., 2013; Asay-Davis et al., 2017). St Laurent et al. (2013) argue that models must have a resolution of around 1 km in order to resolve the mesoscale circulation and eddies occurring, whilst the CMIP5 AOGCMs have resolutions of ~1°. Therefore, circulation features responsible for heat delivery to the ASE are likely not being fully captured in models, resulting in large model errors in this region. However, it must be noted that a considerable portion of the modelled variability could manifest as a result of random internal variability that has been simulated by the models in order to capture some of the variability in the earth system, which would therefore have no physical basis. In light of these uncertainties that manifest as a result of coarse resolution, however, the collective range in modelled temperature on shelf by the whole subset, broadly captures the overall temperatures observed on shelf (with the exception of CESM1-CAM5 and MRI-CGCM3). This could support investigations that suggest using a mean of the ensemble, or a subset of models, might better capture observed climate (Bracegirdle et al., 2008).

Table 3.4: *ASE 400-700m layer ocean temperature RMSE and MBE for the subset of best performing models CMIP5 models over the observational period 1979-2016.*

Model	RMSE (°C)	MBE (°C)
bcc-csm1-1	0.79	-0.05
CanESM2	0.85	-0.37
CCSM4	1.24	0.96
CESM1-CAM5	1.75	1.57
MRI-CGCM3	2.19	2.04
NorESM1-ME	1.15	0.83

The models best able to capture observed temperature in the ASE are bcc-csm1-1 and CanESM2 (tab. 3.4). The Southern Ocean temperatures over the historical period (fig. 3.7) show that these models, particularly compared with the other subset members, simulate a large band of cold waters around the coast of the ice sheet. Given that cold water has a higher density than warm water, this layer of cold water around the coast of the ASE will be acting to suppress the thermocline and could be blocking CDW from upwelling onto the continental shelf (Thoma et al., 2008; Walker et al., 2008; Dinnimann et al., 2016). In contrast, models with a reduced area of colder waters such as that seen in CCSM4 and NorESM1-ME may be exhibiting a thin CDW layer on shelf, given that there is a lesser extent of blocking, which would explain the warmer temperatures on shelf, given that CDW is modifying local ASE temperature on shelf.

Assuming a linear trend in temperature over the course of the 38-year observational period, the decadal temperature change ranges from -0.05°C decade^{-1} projected by bcc-csm1-1 to 0.17°C decade^{-1} for NorESM1-ME (using the RCP8.5 forcing scenario for the last decade of the period). Changes to the on shelf CDW temperature in the ASE since the 1990s has been observed to have increased at a rate of between 0.1 to 0.3°C per decade (Schmidtko et al., 2014). This would indicate that the subset of models have generally underestimated the magnitude of observed warming over the observational period. However, the observations used to calculate this trend are limited and appear to include an outlier that could lower the calculated temperature trend (Schmidtko et al., 2014; figure 1E), which would be more consistent with the projections modelled. Furthermore, observations from the Hadley Centre EN4 dataset in the ASE (fig. 3.11), illustrate a variability in temperature of 0.36°C which exceeds the magnitude of the proposed warming in the Schmidtko et al. (2014) paper. Additionally, an analysis of the observations, exclusively, indicates a negative trend in temperature over the observational period (fig. 1A). Further indicating that the large positive warming described by Schmidtko et al. (2014) is likely unrealistic.

The use of the Met Office Hadley Centre EN4 *in situ* observational data for model comparison is advantageous over other methods as it provides a more direct comparison and is able to capture some of the deficiencies in model output that manifest as a result of coarse resolution (St Laurent et al., 2013). The errors obtained in this study are larger than those presented by Little and Urban (2015) who compared 1x1° gridded observational ocean temperature from the WOA12 dataset to CMIP5 output. For example, their study identified MRI-CGCM3 to have the largest RMSE over their observational period of 1.45°C whilst in this investigation the same model has a scenario averaged RMSE of 1.76°C, making it the 5th best model in the investigation. Evaluation of models using in situ

profiles, instead of gridded observations, illustrates that models do not capture the spatial variability of the ocean temperature and therefore provides a more thorough assessment of model performance. Similar findings were proposed whereby AOGCMs were illustrated to capture broad scale patterns rather than specific finer scale processes, such as coastal processes near the Antarctic ice sheet (Heuze et al., 2013; Goddard et al., 2017).

3.4.1. Limitations

Whilst the errors inherent in the model data are being assessed, it must be acknowledged that observational datasets, such as the Hadley Centre EN4 dataset used, have associated uncertainties (Schneider and Reusch, 2016). Whilst an attempt was made to reduce the impact of these on our bias calculation by employing the quality control data and removing profiles with poor performance from the dataset, this cannot necessarily account for all the errors associated with the dataset. However, as this study utilizes the bias and RMSE calculations in order for a relative comparison between biases to be made, errors inherent in the observational dataset should be systematic.

Availability and coverage of observational data is limiting the extent of the comparison, given the poor spatial and temporal coverage of the data. Assessing sampling has inferred that the coverage of observational data is generally capturing warmer temperatures and therefore are not fully representative of the distribution of temperatures over the Southern Ocean, meaning our RMSE and MBE biases are themselves biased. From the maps of observational data over this layer it is evident that there are few profiles around the coast. These below freezing temperatures are likely responsible for lowering the mean temperature over this layer and therefore the lack of these observations is resulting in considerably higher means over the period for the sampled data. Moreover, considering the observations on shelf in the ASE, only 23 of the 456 months of the observational period have temperature measurements. Lack of coastal data is largely associated by the limitation of ship access due to extensive ice cover and challenging weather conditions, so deployment and retrieval of mooring is prevented (Mallet et al., 2018). Furthermore, the temporal extent of observations are also limited, with the majority of observations recording summer ocean properties (Heywood et al., 2016). Winter observations are generally at depths below the surface given the presence of sea ice interfering with moorings, this further limits the annual coverage of observational data. Due to the scarcity of observations in the ASE, it has been decided that the overall Southern Ocean RMSE and MBE are more reliable than those local to the ASE. Should the ASE RMSE have been used to identify the best performing subset, it is likely that different models would be included in the subset.

The profiles recorded in the Hadley Centre EN4 dataset captures a few minutes of time, whilst the simulated models capture the average temperature for the month and therefore the observations will be temporally variable. Whilst spatial variability was captured through the interpolation of model data both horizontally and vertically through depth, temporal variability has not been treated. This uncertainty will be captured and in part explain some of the observed bias.

This analysis is restricted by its limitation to only one climate variable. Given that water masses are distinguished by salinity (density), oxygen and temperature we are making assumptions as to what the water masses are on shelf. Furthermore, interpreting the patterns of variability seen in the ASE temperature projections would be better investigated with sea level pressure data in order to attribute onshore flow to changes in wind forcing, as was suggested and performed in previous studies (Thoma et al., 2008; Wåhlin et al., 2010). Naughten et al. (2018) perform analysis of atmospheric pressure as simulated by the CMIP5 ensemble and compare this with ERA-Interim data.

3.5. Summary

This chapter has assessed the ability of CMIP5 ensemble members to simulate observations of ocean temperature during the period 1979-2016. RMSE scores for each of the 27 models ranges from between 1.66°C to 2.50°C. Our method of analysis involved comparison of model data with *in situ* measurements, which is a more direct analysis than other studies and therefore provides a greater assessment of model performance. Large errors are likely to be associated with the coarse resolution of these AOGCMs and their inability to represent circulation features such as mesoscale eddies in addition to models being unable to capture the position of the ACC and the resulting westerlies in the Southern Ocean, which will be impacting simulation of temperature. Further investigation into other CMIP5 variables would be needed in order to establish more of the causes of these biases.

A subset of six models with the lowest RMSE scores were selected, specifically bcc-csm1-1, CanESM2, CCSM4, CESM1-CAM5, MRI-CGCM3 and NorESM1-ME. Exploring temperatures averaged over the ASE during the historical period reveals a large range of between -0.5°C to 2.0°C for the subset of models. Models with the highest mean temperature were found to have the lowest variability, and vice versa for the lowest mean temperatures. The six models together were able to capture the range of temperatures observed on shelf over the observational period, however, no single model captured the large variability of the observations. Furthermore, large errors arose in the calculations due to the inability of these models to capture the timing of observed variability.

This analysis was largely limited by the poor spatial and temporal coverage of the *in situ* temperature dataset used. Sampling has shown that temperatures captured by the data tend to be those in warmer regions and therefore the assessment is not considering the range of observed temperatures. Furthermore, in the ASE, temperature measurements have only been retrieved for 23 of the 456 months of the observational period. Increased coverage of data will benefit evaluation of climate models.

Chapter 4 : Exploring CMIP5 Projections of Ocean Temperature in the Southern Ocean

4.1 Introduction

The CMIP5 ensemble was used to project future climate in order to establish the range of possible conditions of the earth system under a changing climate. This chapter aims to explore the range of ocean temperature projections averaged over the 400-700m in the Southern Ocean from 2017 to 2100, produced by the best performing CMIP5 models (which were identified in Chapter 3) forced with the RCP2.6 and RCP8.5 scenarios. Further, an exploration into the projected temperatures on-shelf from 2017 to 2100 in the ASE was performed, forced with both RCP2.6 and RCP8.5.

4.2 Data and Methods

4.2.1. Southern Ocean

Analysis in this chapter will be restricted to the six models identified in Chapter 4 as best reproducing observed temperature over the observational period. For the projections over the period 2017-2100, the r1i1p1 experiment was analysed for each CMIP5 model forced under RCP2.6 and RCP8.5. These scenarios describe the lowest and highest forcing scenarios outlined in the IPCC Assessment Report 5 (Collins et al., 2013), and therefore cover the greatest range of climate projections. Again, the output from the models were downloaded and resolutions interpolated so that all models are read onto 1x1^{o} grid, for latitudes south of 30^{o}S. Temperatures were interpolated in order to obtain the mean temperature over the 400-700m layer for all models. This interpolation was necessary due to the differing vertical resolutions of the models.

Temperature averaged over 400-700m depths were selected to illustrate the ocean temperatures of the water masses accessing the continental shelf in the ASE (Thoma et al., 2008; Little and Urban, 2016). The upper limit of this layer was chosen to define the lower reach of the Winter Water layer and therefore the thermocline (Webber et al., 2017; Wåhlin et al., 2012; Nakayama et al., 2017). This also will exclude short term variability observed in surface waters (Timmermann and Hellmer, 2013).

Whilst the depth of the continental shelf could be used as the lower boundary of the on-shelf depth layer, the coarse resolution of the AOGCMs would be unable to capture sufficient detail of the continental topography (Lazeroms et al., 2018) and therefore a constant boundary was set. Furthermore, different characterisation of topography in each model would mean depth averaged temperature would be non-uniform across the different models. As a large portion of the shelf resides at ~700m from bathymetric maps of the continent (Nitsche et al., 2007), one can state that averaging temperatures over this depth is roughly representative of those on shelf.

4.2.2 ASE

For each model, a projected ocean temperature time series from 2017 to 2100 was calculated by averaging ocean temperature over the 400-700m layer in the ASE, which constitutes a region between 103-113°W and 72-75°S, taking into account the curvature of the earth. A limit on the southernmost portion of the region was instated, given that models are unable to simulate ice shelf cavities and therefore the simulated temperatures in regions where shelves are present are unreliable.

In order to fully explore the data, descriptive statistics of the trends were calculated. The monthly temperatures from 2017-2100, inclusive, were averaged to provide the mean temperature. The variability of the trends was obtained by calculating the standard deviation of the detrended temperature time series.

4.3 Results: Southern Ocean

4.3.1. RCP2.6

Projections by the end of the 21st century under the RCP2.6 (fig. 4.1) forcing are very similar to those for the historical period (fig. 3.7). Models are projecting below freezing temperatures along the coast of the ice sheet of <-1.0°C, with warmer water at lower latitudes around 30-60°S exceeding 4°C. All models project the coldest waters to be situated in the Weddell and Ross Seas, however, the models differ in the extent and reach of cold waters surrounding the coast. The bcc-csm1-1 projection has the greatest region of below freezing temperatures encompassing the entire coast, reaching into the Atlantic Sector of the Southern Ocean from the Weddell Sea. In contrast, the MRI-CGCM3 projection of ocean temperature is the exemption from this pattern, with waters of around 2.5°C in the Pacific sector of the Southern Ocean and the WAIS coast.

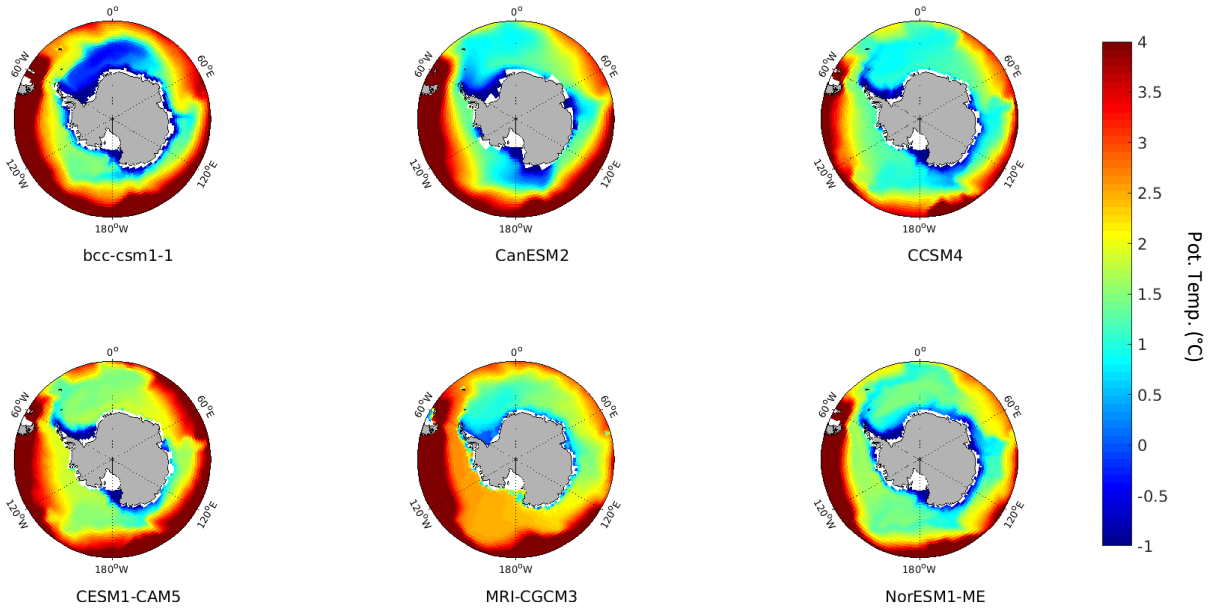

Figure 4.1: *Maps of projected mean 400-700 m layer ocean potential temperature in 2100 (2091-2100 mean) forced with the RCP2.6 scenario. Each map represents a projection by each CMIP5 model in the subset of best performing models.*

Overall, the temperature change relative to the historical period under the RCP2.6 scenario in most models is modest, with a maximum warming of ~1°C (fig. 4.2), though the pattern of change varies across the subset. Models bcc-csm1-1, CanESM2, CCSM4 and CESM1-CAM5 show warming >0.4°C that is highest at lower latitudes, away from the continent. CCSM4 and CESM1-CAM5 show very similar patterns of warming, with the latter exhibiting warming of a greater magnitude, reaching >1°C. Both models show warming of the Indian and Pacific Oceans extending to EAIS in addition to a warming of >0.6°C along the east Antarctic Peninsula in the Weddell Sea. Temperature change along the coast is modest, with some warming along the eastern coast of EAIS in MRI-CGCM3, NorESM1-ME and CanESM2. Similarly, temperature change in the ASE is minimal, ranging from a 0-0.5°C warming.

NorESM1-ME and MRI-CGCM3 have the most different patterns of temperature anomalies, both exhibiting regions of ocean cooling. MRI-CGCM3 projects temperature change over the century to vary over the domain from -0.2°C to 0.2°C, which is more modest than the rest of the models in the subset. Specifically, there is region of warming over 0.4°C in the Weddell Sea and a cooling in excess of -0.5°C stretching north from the tip of the Antarctic Peninsula. NorESM1-ME projects a warming of over 1°C extending from the Weddell Sea into the Atlantic sector of the Southern Ocean. The model also projects a region of cooling greater than -0.5°C from the tip of South America stretching west across the Southern Ocean low latitudes.

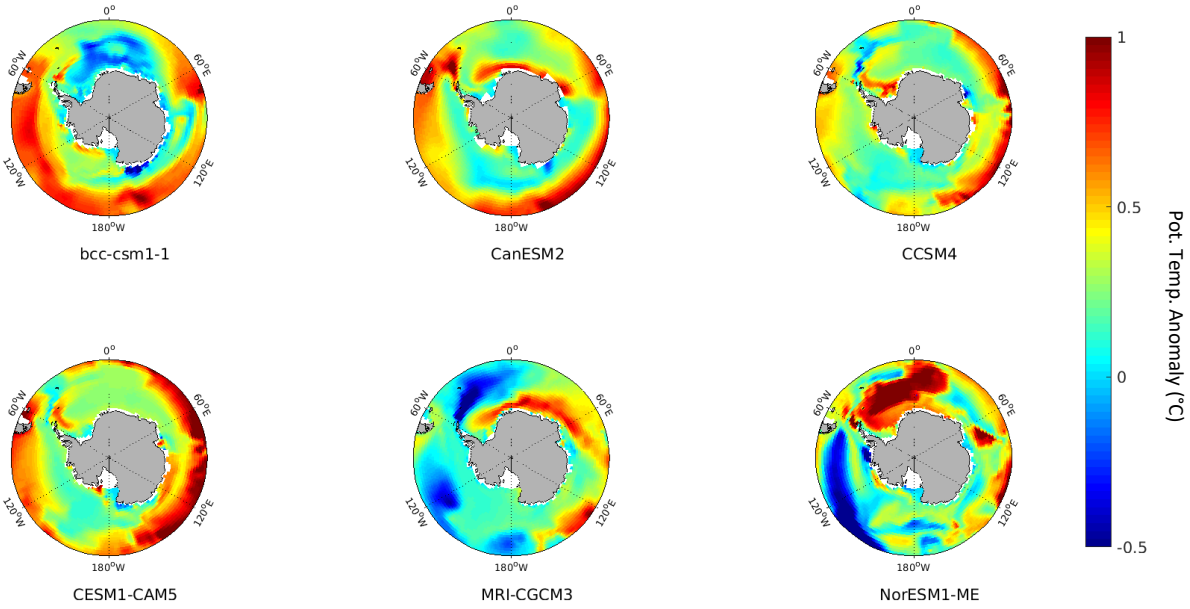

Figure 4.2: *Maps of projected mean ocean potential temperature anomaly in 2100 (2091-2100 mean) relative to present day (2005-2016 mean) forced with the RCP2.6 scenario. Ocean temperature is averaged over the 400-700m layer over the Southern Ocean. Each map represents a projection for each CMIP5 model in the subset of best performing models.*

4.3.2. RCP 8.5

The overall pattern of projected temperature under RCP8.5 is similar to that of RCP2.6, with cold waters around the coast and warmer temperatures at lower latitudes (fig. 4.3). However, the spatial extent of coastal cold waters is notably reduced. The model with the largest coastal region of ocean temperatures below freezing is bcc-csm1-1 where cold water <-1°C extends eastward along the coast from the Weddell Sea but ceases along the WAIS coast. Presence of below freezing temperatures are less prominent in the remaining models, with only CESM1-CAM5, CanESm2 and NorESM1-ME indicating some below freezing temperatures in the Weddell and eastern Ross Seas. Below freezing temperatures in the Ross Sea are also observed in CCSM4, CESM1-CAM5 and NorESM1-ME. MRI-CGCM3 projected ocean temperatures are predominantly above 0°C, with temperatures over 4°C in the Pacific Ocean in close proximity to the ice sheet.

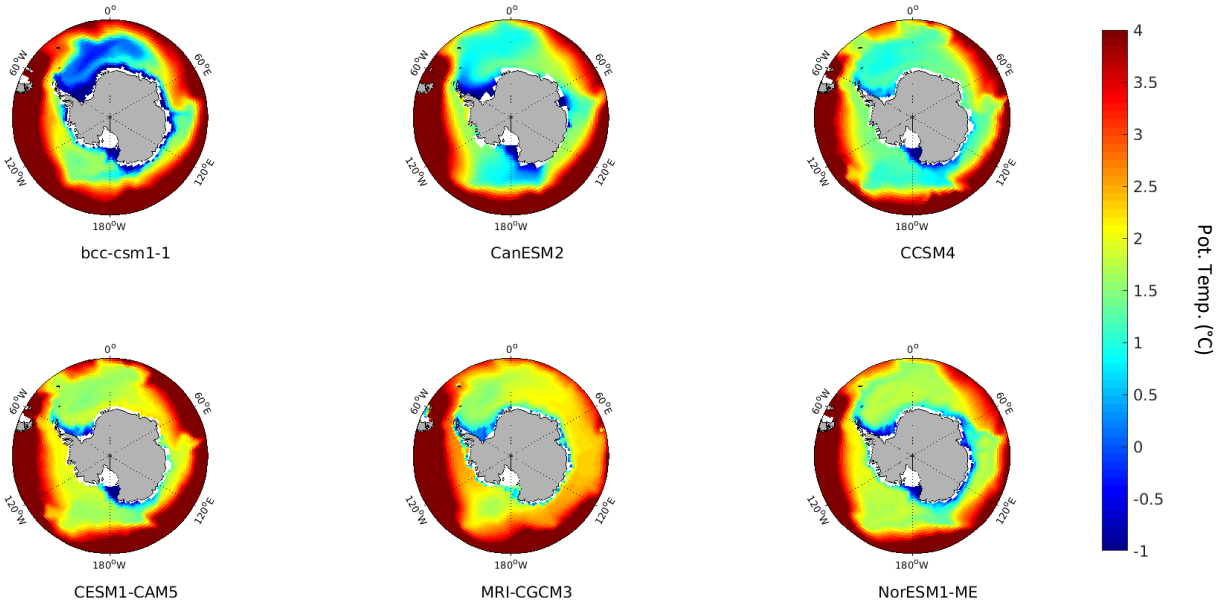

Figure 4.3: *Maps of projected mean 400-700 m layer ocean potential temperature in 2100 (2091-2100 mean) forced with the RCP8.5 scenario. Each map represents a projection by each CMIP5 model in the subset of best performing models.*

Relative to present day, models bcc-csm1-1, CanESM2, CCSM4 and CESM1-CAM5 project the greatest magnitude of warming ~2°C to be at lower latitudes of ~40°S over much of the Southern Ocean (fig. 4.4). These four models are consistent in terms of the patterns of their temperature anomalies. Below 60°S these models project warming of ~0.5°C. Models indicating warming in the Weddell Sea including CCSM4, CESM1-CAM5, MRI-CGCM3 and NorESM1-ME, with the latter projecting this warming to extend north into the Atlantic sector of the ocean.

In contrast, projections produced by bcc-csm1-1 and MRI-CGCM3 show distinct areas in which the ocean is cooling, most notably being a temperature change of <-1°C stretching from the top of the Antarctic Peninsula travelling eastward to 10°E. MRI-CGCM3 also projects a large decrease in temperature of over 1°C in the Ross Sea. Warming in the ASE is evident in models bcc-csm1-1, CanESM2, CCSM4 and NorESM1-ME, ranging from 1-2°C in magnitude. Furthermore, models that project coastal warming around the EAIS are CanESM2, CCSM4, CESM1-CAM5, MRI-CGCM3 and NorESM1-ME.

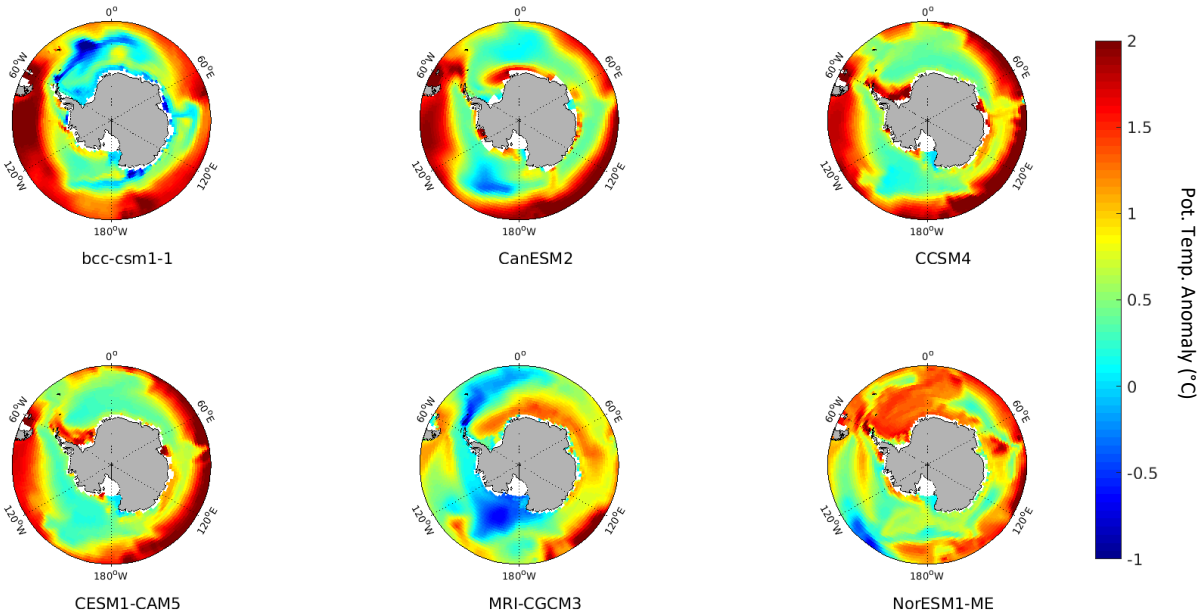

Figure 4.4: *Maps of projected mean ocean potential temperature anomaly in 2100 (2091-2100 mean) relative to present day (2005-2016 mean) forced with the RCP8.5 scenario. Ocean temperature is averaged over the 400-700m layer over the Southern Ocean. Each map represents a projection for each CMIP5 model in the subset of best performing models.*

4.3.3. Summary

Generally, all models under both forcing scenarios project warm temperatures at lower latitudes and colder temperature closer to the coast, however there is a considerable difference in projections when comparing the magnitude of temperatures in projections for each of the scenarios. The extent of cold waters around the coast is greater for the mitigation scenario, RCP2.6, where most models project below freezing temperatures in the Weddell Sea and along the coast of EAIS. In contrast, projections forced with RCP8.5 show a reduced region of below freezing temperatures, with bcc-csm1-1 being the only model with a large extent of cold water.

The patterns of temperature anomalies indicate that most of the warming is taking place at lower latitudes in both scenarios. Warming is present in the Weddell Sea in all models other than bcc-csm1-1; this model projects a regional cooling of 0.2°C and 0.5°C in RCP2.6 and RCP8.5 respectively. Furthermore, an ocean temperature cooling is notable in the Ross Sea in all models with the exception of NorESM1-ME. Warming of >0.4°C local to the ASE is visible in CCSM4 and NorESM1-ME under the RCP2.6 scenario. Whereas under the RCP8.5 scenario, warming local to the ASE and more generally along the coast of WAIS is visible in all model projections with the exception of CESM1-CAM5 and MRI-CGCM3. Warming under the higher emissions scenario appears to exceed 1°C in the ASE.

4.4. Results: ASE

4.4.1. RCP2.6

The projections of ocean temperature on shelf in the ASE illustrate a broad range of patterns (fig 4.5). Despite the observed variability in temperature trends, overall there is little change in the mean temperature by the end of the century, concurrent with the projections of ocean temperature over the Southern Ocean.

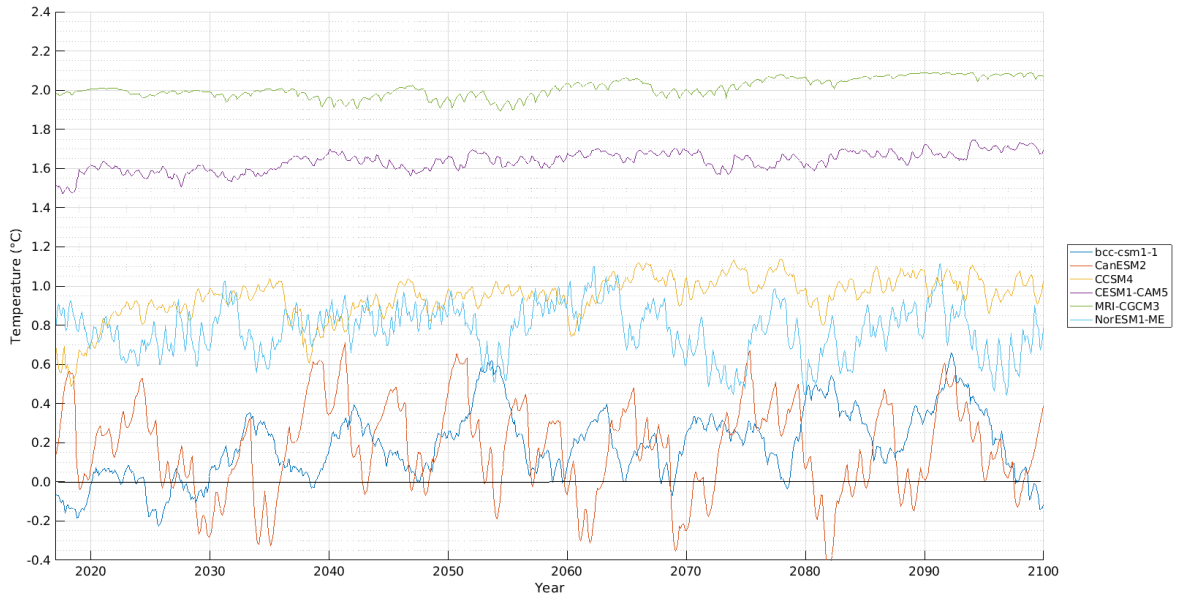

Figure 4.5: *Projected RCP2.6 forced ocean potential temperature from 2017-2100 averaged over the 400-700m layer in the ASE for each CMIP5 model in the subset.*

The six-model subset covers a range of -0.4-2.2°C, which is consistent over the course of the century long projection period. The models with the lowest mean temperature projections, bcc-csm1-1 (0.18°C) and CanESM2 (0.17°C), have the highest variability of temperature over the projection period, of 0.16 and 0.23°C respectively (fig 4.6). Variability manifests over both annual and decadal length cycles, exceeding 1^{o}C on occasion over the CanESM2 projection. Decadal cycles are more distinct in bcc-csm1-1, where the interannual variability is less pronounced.

The models with the highest mean temperatures are CESM1-CAM5 and MRI-CGCM3 with temperatures of 1.6°C and 2.0°C respectively. These two models also have the lowest overall variability of 0.035°C and 0.033°C respectively, occurring on seasonal timescales. CCSM4 illustrates a large increase in temperature over the first 5 years of the projection period, from ~0.2°C to 0.9°C, following which the slope flattens for the remainder of the projection period whilst remaining

positive. This appears to follow on from the increase in temperature observed over the historical period which recovers after a large fall in temperature (fig. 3.10). NorESM1-1 has a mean temperature of 0.77°C and variability of 0.13°C. The magnitude of the oscillations in temperature projected by NorESM1-1 appear to increase over the course of the century, in addition to showing a decadal scale cycle in temperature toward the end of the century.

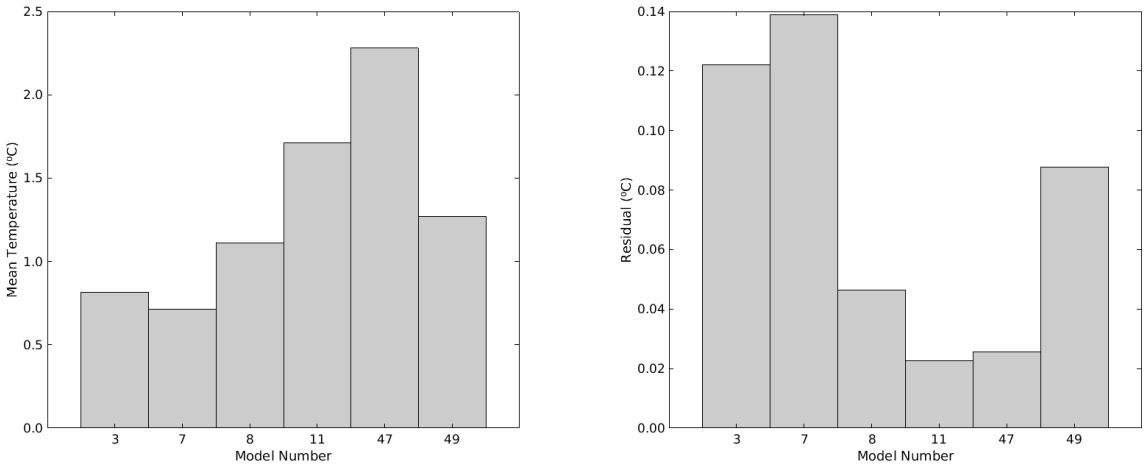

Figure 4.6: *Statistics for each CMIP5 model in the subset describing the RCP2.6 projected temperature from 2017-2100 in the 400-700m layer averaged over the Amundsen Sea. Left: mean temperature. Right: residual (standard deviation).*

Relative to their respective present day means, which were averaged over the period 2005-2016, the spread in model temperature change decreases, with the models indicating similar ranges of temperature which fluctuate between -0.2°C and 0.4°C, with some more variable models such as bcc-csm1-1 and CanESM2 exceeding this with their large fluctuations (fig. 4.7); where the magnitude of the variability exceeds the magnitude of the temperature trend. In contrast, CESM1-CAM5 and MRI-CGCM3 illustrate a relatively flat positive temperature change, with high frequency, low amplitude variability on seasonal timescales.

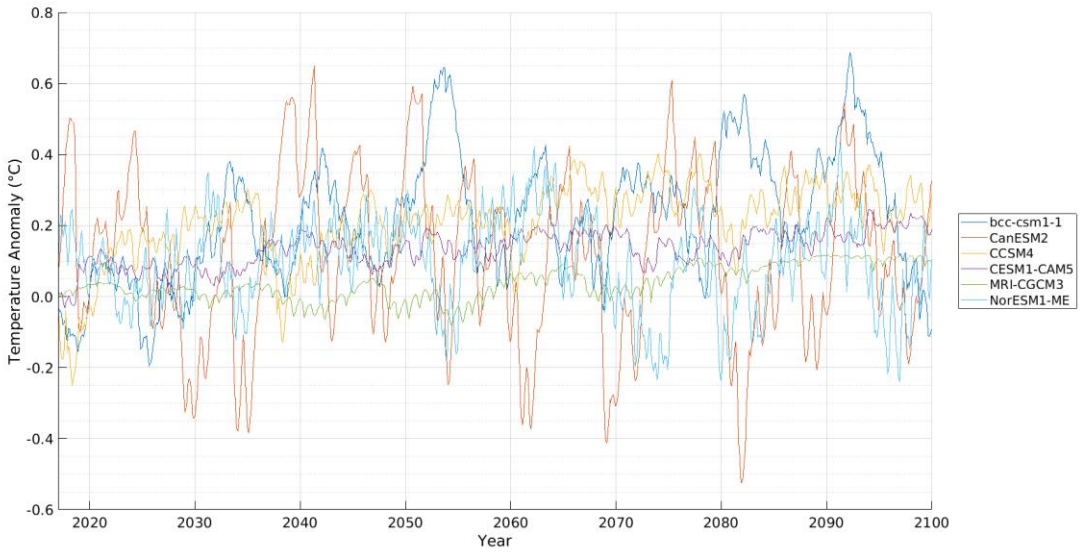

Figure 4.7: *Projected RCP2.6 ocean potential temperature anomalies from 2017-2100 relative to the 2005-2016 mean for the 400-700m layer in the Amundsen Sea for each CMIP5 subset member.*

4.4.2 RCP8.5

All models project an increase in the mean ASE ocean temperature over the century, with the exception of MRI-CGCM3. The spread of modelled ocean temperature projections, forced with RCP8.5, decreases over the course of the century. The 2017 modelled temperature range of between -0.1-2.0°C reduces to a range of 0.8-2.0°C by 2100, suggesting that models are converging in their projections of temperature in the ASE (fig. 4.8). Whilst overall the changes in temperature are greater

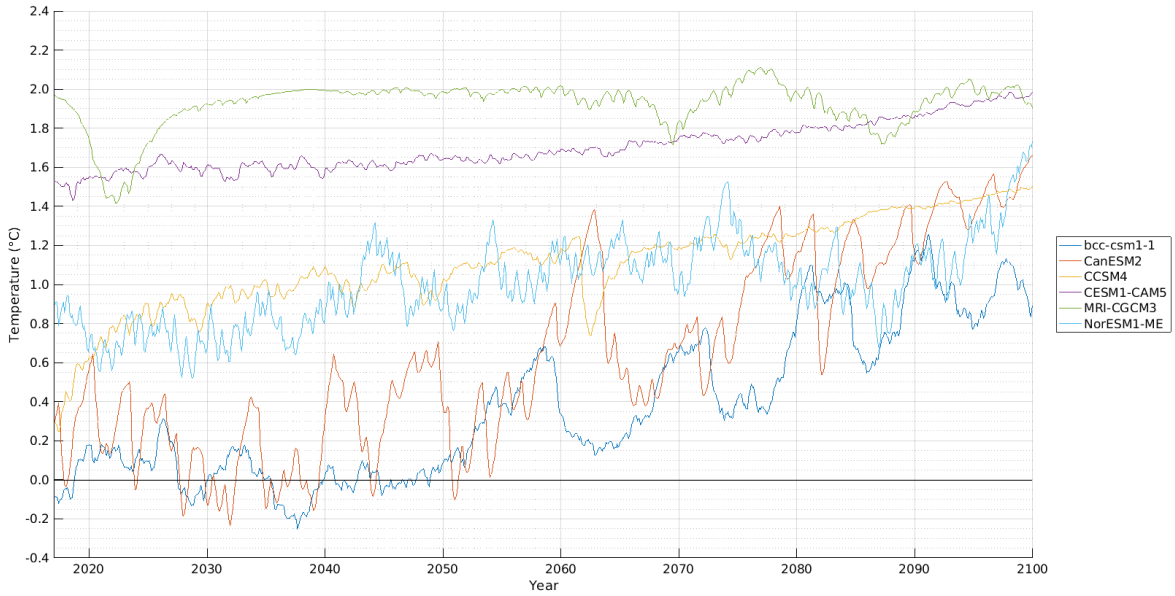

Figure 4.8: *Projected RCP8.5 forced ocean potential temperature from 2017-2100 averaged over the 400-700m layer in the ASE for each CMIP5 model in the subset.*

than those projected under the RCP2.6 forcing, models are producing similar patterns of variability, suggesting that variability could be scenario independent.

Models with the highest mean temperatures of 1.7°C and 1.9°C are CESM1-CAM5 and MRI-CGCM3 (fig 4.9). CESM1-CAM5 has the lowest variability of 0.04^{o}C, in contrast, MRI-CGCM3 projects higher variability of 0.11^{o}C. This larger variability is likely a result of the 0.6^{o}C decline in temperature at the beginning of the projection period, as, aside from this, the magnitude of the seasonal variability appears to be low. CESM1-CAM5 shows a low positive trend, increasing by 0.5°C over the 21st century. Generally, for RCP8.5 forcings, models with the lowest mean temperature have the greatest variability and temperature trend over the century.

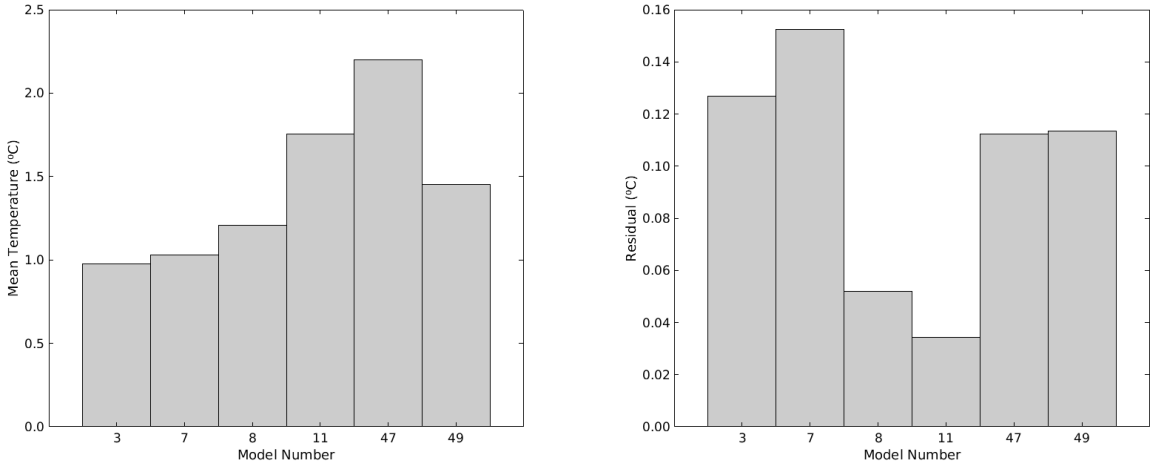

Figure 4.9: *Statistics for each CMIP5 model in the subset describing the RCP8.5 projected temperature from 2017-2100 in the 400-700m layer averaged over the Amundsen Sea. Left: mean temperature. Right: residual (standard deviation).*

The remaining four models present similar temperature trends over the record, with differing patterns of variability. Similarly to the RCP2.6 projection, CCSM4 shows an initial 10-year rapid increase in temperature in the ASE from 0.2-0.9°C followed by a more gradual increase for the rest of the projection period with 0.0094°C variability. NorESM1-ME has a positive trend with temperatures on shelf exhibiting high amplitude seasonal and multi-annual variability with temperature oscillating by up to 0.17°C. The greatest temperature variability over the century is observed in the CanESM2 projection with large temperature fluctuations, averaging 0.26°C, that are irregular in frequency and amplitude. The variability appears to follow an interannual cycle, however there appears to be a number of multi-annual to decadal length cycles over the record. Model bcc-csm1-1 shows the greatest temperature change over the century, increasing from -0.1°C to 0.8°C, with large 0.19^{o}C decadal temperature variability.

The modelled projections of temperature change relative to their respective present day means (2006-2016 average) show an increase in the spread of temperature changes over the century (fig 4.10). MRI-CGCM3 exhibits almost no change over the period, with fluctuations oscillating above and below 0.0°C. This contrasts with CanESM2 which increases by 1.7°C over the period in addition to exhibiting large temperature fluctuations of >0.5°C. In 2100 there is a >1.5°C difference in the temperature change within the subset.

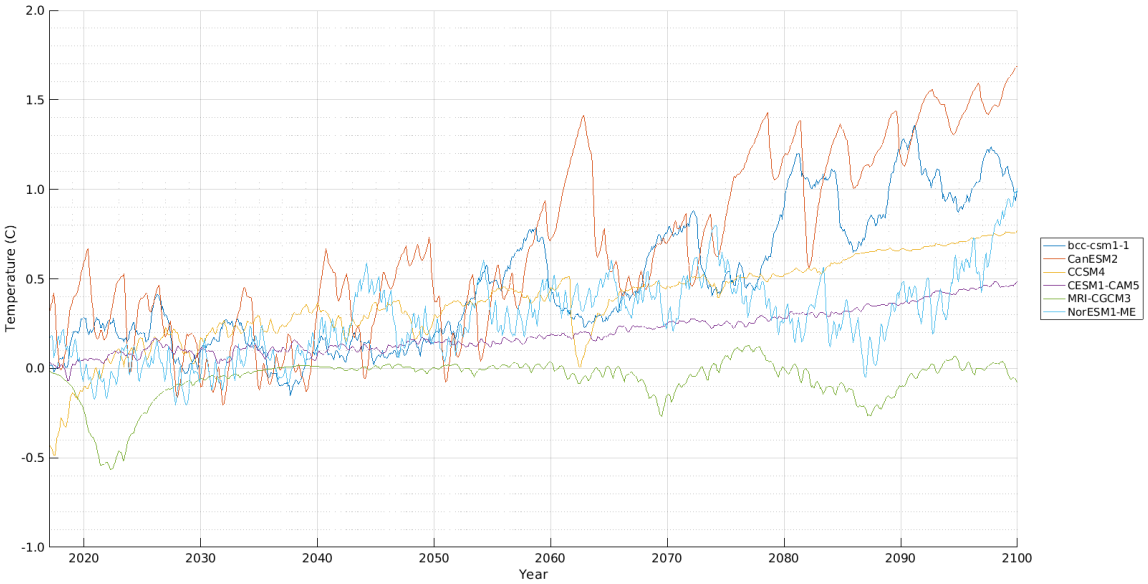

Figure 4.10: *Projected RCP8.5 forced ocean potential temperature anomalies from 2017-2100 relative to the 2005-2016 mean for the 400-700m layer in the Amundsen Sea for each CMIP5 subset member.*

4.4.3. Temperature Trends

Decadal temperature change was calculated by fitting linear regression models to the projection trends in the ASE (fig 4.11). The range of temperature trends is between -0.005°C decade^{-1} for NorESM1-ME to 0.032°C decade^{-1} for bcc-csm1-1 under the RCP2.6 forcing. In contrast the range of trends are from 0.015°C decade^{-1} for MRI-CGCM3 to 0.18°C decade^{-1} for CanESM2. All models had statistically significant p-values at the 95% confidence interval, with the exception of CanESM2 forced with RCP2.6 which has a p-value of 0.4.

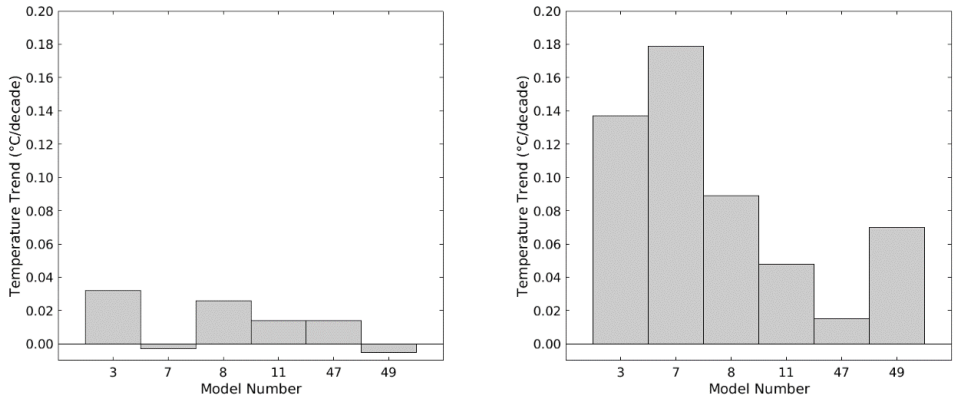

Figure 4.11: *Decadal ocean potential temperature change over the 400-700 m layer in the ASE calculated for each CMIP5 model from 2017 to 2100 forced under RCP2.6 (left) and RCP8.5 (right).*

4.4.4. Scenario Comparison

The range of mean temperature anomalies for the CMIP5 ensemble, when forced with RCP8.5, exceeds the range of values projected under RCP2.6; with the exception of two models (fig. 4.12). In contrast, exploring the subset of six best models exclusively indicates that the range of modelled temperature anomalies in 2100 forced with RCP8.5 fully encompasses the range of temperatures produced with the RCP2.6 forcing. This provides justification for using the RCP8.5 projections, exclusively, in the following chapter.

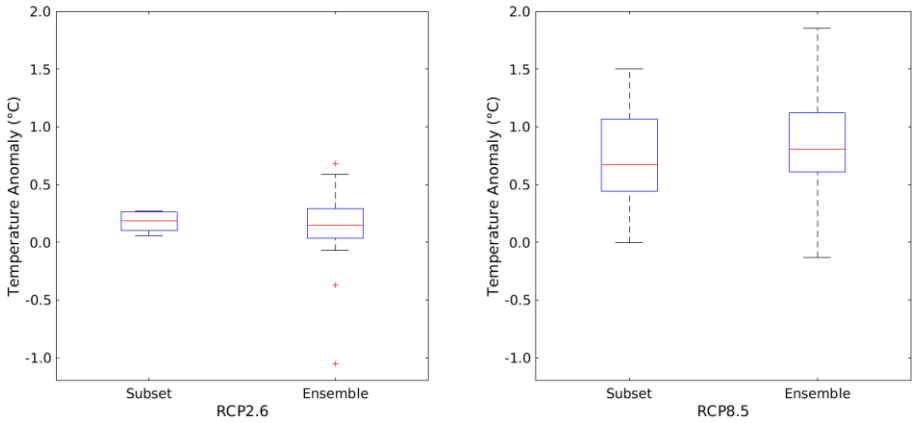

Figure 4.12: *Mean ASE ocean potential temperature anomalies in 2100 for each model (2095-2100 average) relative to present day (2005-2016), as projected by the 27-member CMIP5 ensemble compared with the subset of the six best performing CMIP5 models. Temperatures were averaged over the Amundsen Sea 400-700 m layer and forced with RCP2.6 (left) and RCP8.5 (right).*

4.4.5. Subset Assessment

The range of temperature anomalies captured by the subset roughly reflects the range in temperatures of the ensemble (fig. 4.13), indicating that the subset is a representative sample of the ensemble range and thus sufficient for use in the following chapter.

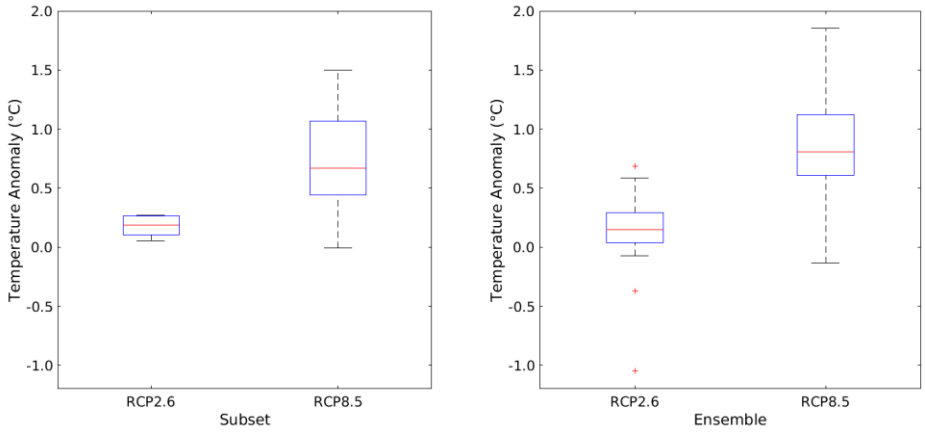

Figure 4.13: *Mean ASE ocean potential temperature anomalies in 2100 for each model (2095-2100 average) relative to present day (2005-2016) forced with RCP2.6 and RCP8.5. Left: temperatures projected by 27-member ensemble of CMIP5 models. Right: subset of the six best performing models (Chapter 3).*

4.4.6. Summary

The range in temperatures projected in the ASE over the 400-700m exceed 2.4°C, from -0.4°C to 2.0°C throughout the projection period forced with RCP2.6. RCP8.5 projections vary in that the initial range in temperatures is of a similar size, -0.2 to 2.0°C, however the models with the lowest temperatures warm to the greatest extent over the projection period, resulting in a convergence in the range. This convergence is also illustrated in the temperature anomalies, where RCP2.6 projections do not differ considerably from 0°C whilst the RCP8.5 anomalies result in a spread of between 0°C and >1.7°C warming in 2100.

Considering the decadal temperature change under the RCP2.6 scenario illustrates that there is little overall change in the mean temperature over the period, with the greatest trend projected by bcc-csm1-1 of 0.03°C decade^{-1} and two modelled trends being negative (though only one was found to be statistically significant). In contrast, the decadal temperature trends under the RCP8.5 forcing exhibits a large range from 0.02 decade^{-1} to 0.18°C decade^{-1} depending on the model. Furthermore, variability of these trends differs depending on model, with models CCSM4 and CESM1-CAM5

illustrating little temperature variation across the period, contrasting with models bcc-csm1-1 and CanESM2 which indicate temperatures to deviate from the mean by ~0.12°C and 0.15°C respectively.

Comparing the modelled temperature anomalies in 2100 relative to the 2006-2016 mean reveals that, for the subset of six models, the temperature anomalies forced with RCP8.5 encompass the range in temperatures projected under the RCP2.6 forcing. As a result of this finding, the investigation will use only the RCP8.5 projections for the following chapter. Furthermore, exploring the difference in temperature anomalies captured by the subset compared with the ensemble indicates that the subset roughly captures the range of the ensemble, and therefore our subset is a good representation of the ensemble.

4.5. Discussion

4.5.1. Southern Ocean

The CMIP5 subset produce fairly similar patterns of projected ocean temperature over the Southern Ocean in 2100, with below freezing temperatures around the coast of the ice sheet and warmer temperatures >4°C over lower latitudes of around 30 to 60°S (fig 4.1 & fig. 4.3), representative of the ACC (Meijers et al., 2014). For all models in the subset, the potion of the ACC in the Pacific Sector has the greatest reach southward (Schmidtko et al., 2014). This southward veering current in the Pacific Ocean sector can be responsible for CDW incursion, therefore the representation of this position across the subset could influence the resulting temperature on shelf in the ASE (Little and Urban, 2015; Thoma et al., 2008). For example, MRI-CGCM3 simulates the closest ACC to the coast, in addition to a lack of cold waters blocking the WAIS coast from these warmer temperatures which could be the cause of the high, 2°C temperatures on shelf (fig. 4.5 & fig. 4.8).

Projections of temperature change in the Southern Ocean averaged over the 400-700 m layer under the RCP2.6 forcing illustrate a modest change in temperatures. The greatest warming is occurring further afield from the ice sheet from 30-60°S which is associated with a warming of the ACC (Liu and Curry, 2010), consistent with the CMIP3 ensemble mean temperature projections (Yin et al., 2011) and CMIP5 ensemble mean (Sallée et al., 2013). This warming could be the result of the movement in the ACC causing warmer waters to inhabit lower latitudes, instead of, or in addition to, a warming of the water masses situated just south of the ACC (Sallée et al., 2013; Turner et al., 2017).

Under the RCP8.5 scenario, all of the models (excluding NorESM1-ME) demonstrate a cooling in the Ross Sea, which is consistent with the observations of Schmidtko et al., (2014). This was associated with a freshening of the gyre through introduced meltwater produced in the Amundsen and Bellingshausen Seas and transported westward by the coastal current (Nakayama et al., 2014). However, it is uncertain whether these mechanisms are in fact responsible for the cooling projected by the CMIP5 models, given that freshening was modelled by FESOM (Timmerman et al., 2012), a finite element model with greater resolution capacities than the CMIP5 AOGCMs. Additionally, FESOM models ice shelf cavities, and thus input of meltwater, which are not captured in the CMIP5 models (Timmermann and Hellmer, 2013).

Similarly, almost all of the models are indicating, under both scenarios, a warming in the Weddell which is concurrent with the findings of Little and Urban (2015). Models CCSM4 and CESM1-CAM5 show a warming local to the coast of the Weddell, whereas MRI-CGCM3 and NorESM1-ME indicate a

warming over the whole sea, stretching around the EAIS coast. A study by Hellmer et al. (2017) indicate that under an extreme warming scenario forced with atmospheric CO2 over 700ppmv in 2100 results in a warming of the Weddell Sea sufficient to cause excessive melting of the Ronne-Filchner ice shelf, this was also observed in CMIP3 SRES A1B where a redirection of the coastal current causes incursion of warm waters beneath the ice shelf (Hellmer et al., 2012). The difference in regions of warming in the Weddell could also be related to the modelled sea ice extent, as over this period some models still indicate that sea ice is present at the end of summer over the Weddell by the end of the century (Church et al., 2013; Comiso and Nishio, 2008). The presence of sea ice acts to block surface warming (Turner et al., 2013), which over a multi-decadal timescale could be influencing the subsurface depths of this investigation and would be resulting in warming to a lesser extent over the region. To establish the cause of this warming a more in-depth investigation into additional variables such as sea ice and ocean circulation would be necessary.

4.5.2. Amundsen Sea

Under the RCP2.6 scenario, there is little difference in the magnitude of temperature change in the ASE across the model subset (fig. 4.7). All models are indicating large variability on differing timescales, from seasonal to multi-annual, with mean variability ranging from 0.033 to 0.14°C. By the end of the century, the projected temperature anomalies range from 0.06 to 0.27°C, demonstrating that the variability of temperature is not much lower than the magnitude of the overall temperature change. The ensemble mean in the ASE, calculated along the coast of the ice sheet, indicates 0.21°C of warming over the 400-700 m layer by the end of the 21st century under the same forcing scenario (Little and Urban, 2015), which lies at the upper end of the range of projections from the six-model subset. RCP8.5 forcing shows a large range in temperature anomalies by the end of the century; from a modest cooling of -0.05°C to a warming of 1.5°C. This is consistent with the ensemble mean warming of 0.66°C in the region for the 400-600m layer (Little and Urban, 2015), a mean for the West Antarctic coast over the 200-500m layer of 0.5 ± 0.4°C (Yin et al., 2011) and a modelled warming of 0.41°C over the 100-700 m layer within the ASE (Goddard et al., 2017).

Over the course of the 21st century there is a large range in the projected temperature anomalies across the subset, with MRI-CGCM3 exhibiting the smallest temperature change of -0.005°C whilst CanESM2 indicates an increase in temperature of 1.5°C. MRI-CGCM3 has high temperatures in the ASE during the historical period (fig. 3.11), which change little over the 21st century. Such high temperatures on shelf are likely associated with the warm waters in the Pacific Ocean (Steig et al., 2012) and lack of cold waters blocking the coast of the ice sheet (Jacobs et al., 2011). Therefore, this

model may not be simulating delivery of CDW to the ASE, which would be understandable given the coarse resolutions of AOGCMs and the topography of the models, meaning models are unable to capture this feature of ocean circulation (Little and Urban 2015). Thus, high temperatures are a result of the Pacific Ocean teleconnections established by Steig et al. (2012). Further, patterns of temperature change projected by MRI-CGCM3 over the Southern Ocean show temperature anomalies of around 0°C adjacent to the ice sheet, which are consistent with the -0.005°C decade^{-1} temperature change in the ASE. In contrast, CanESM2, which shows the greatest warming trend in the ASE, exhibits a localised region of temperatures exceeding 2°C in the ASE. Given that this temperature anomaly is local to the ASE and is not occurring over all waters around the WAIS coast indicates that it is likely manifesting as a result of the upwelling of warm CDW on shelf (Goddard et al., 2017; Turner et al., 2017; Thoma et al., 2008; Assmann et al., 2013). This indicates that the coarse resolution AOGCMs are able to replicate processes that result in this localised incursion to take place and indicates that the representation of temperatures across the southern Pacific Ocean is likely to impact the simulation of local temperatures in the ASE.

Models bcc-csm1-1, CanESM2 and CCSM4 indicate the greatest warming over the low latitudes of the Pacific Ocean sector of the Southern Ocean which is attributable to a warming and migration of the ACC (Sallée et al., 2013; Meehl et al., 2007). Furthermore, when comparing the RCP8.5 maps to those for the historical period indicates the situation of the ACC closer to the coast in the future scenario (fig. 3.7). These three models exhibit the greatest decadal temperature trends relative to present day (fig. 4.11), which could be an indication of the impact of ACC migration on onshore flow in the ASE. The observed poleward shift of the ACC was found to drive a strengthening of the westerlies bringing warm water masses on shelf in the region (Sallée et al., 2013; Bracegirdle et al., 2013; Meijer et al., 2012; Gille, 2002). Furthermore, migration has also been associated with a positive SAM (Marshall, 2003), which could be underlying the subsurface warming trends observed through enhanced onshore flow due to a strengthening in circumpolar westerlies (Gillet and Fyfe, 2013; Spence et al., 2014). It could be interesting to explore the migration of the ACC in CMIP5 projections and consider the correlation between migration and increased heat delivery to the ASE, this could be investigated in future work.

The variability of temperature over the century, as indicated by the standard deviation of projected temperature from the detrended time series, provides some insight into the different ways in which the models are simulating ocean and atmospheric circulation; and the way in which these patterns are manifesting in the ocean temperature in the ASE. Over the 400-700m layer, temperature change

signals on short timescales are associated with the changing inflow of warm water masses on shelf, as was observed in numerous studies (Walker et al., 2008; Thoma et al., 2008; Wåhlin et al., 2010; Turner et al., 2017; Dutreiux et al., 2014). Surface processes such as heat loss to the atmosphere and ice melt freshening are generally confined to the upper 150m of the ocean (Mallet et al., 2018) and therefore will be unlikely to be directly influencing the depths of interest in our study on seasonal timescales. In contrast, warming observed over longer time scales is more likely attributable to core warming of CDW, which was observed on decadal timescales in the ASE (Wåhlin et al., 2012; Sallée et al., 2013), or an increase in the thickness of the CDW layer on shelf which is acting to modify temperatures in the ASE (Thoma et al., 2008; Turner et al., 2017).

All model projections of ocean temperature in the ASE appear to experience seasonal changes in temperature, particularly models MRI-CGCM3 and CESM1-CAM5, likely associated with wind driven seasonal patterns of on-shelf CDW delivery (Thoma et al., 2008; Wåhlin et al., 2010). Seasonal cycles in the onshore flow of CDW were associated with the seasonal cycle of thermocline depth, which is likely linked to seasonal changes in the depth and location of the ASL (Assmann et al., 2013; Turner et al., 2013; Arthern and Williams, 2017). This variation in temperature is evident in all six of the high performing models, however, as the magnitude of this variability differs across models from 0.08°C to 0.1°C which could suggest that models differ in the quantity of warm water masses accessing the shelf on these timescales, or this could indicate that the models vary in the simulation of core CDW temperatures. Alternatively, given that the magnitude of this variability appears to not change over the course of the projection period, this variability could simply manifest as a result of model internal, random, variability (Taylor et al., 2012). This relationship could be explored further by exploring the onset and timing of seasonal changes to sea level pressure in the Pacific Ocean sector and comparing this to the ocean temperature variability on shelf in the ASE.

Variability in ocean temperature on shelf occurs over sub-decadal timescales, this was particularly evident in bcc-csm1-1 where the cycles appeared to be regularly occurring for equal durations. This could illustrate the impact of ENSO conditions on temperatures on shelf, through heat delivery and changes to ocean circulation (Ding et al., 2011). During an El Nino phase the ASL weakens which causes a weakening of westerlies that are responsible for delivering heat to the continental shelf break (Turner et al., 2017). However, the onset and timing of such a climatic feature is challenging to capture in models (Taylor et al., 2012).

Models with the highest mean temperatures, MRI-CGCM3 and CESM1-CAM5 have the lowest detrended variability, whilst the models with the lowest mean temperature have the highest residuals, those being models NorESM1-ME and CanESM2. This is most relevant for RCP2.6 compared with RCP8.5 projections. It could be inferred that the models with the highest mean temperature over the projection period have the lowest seasonal and annual variability, as warm CDW is more likely a permanent feature on the continental shelf, manifesting as a thicker layer than other models, and therefore temperatures are permanently influenced by this water mass (Thoma et al., 2008). In contrast, models with lower temperatures have larger fluctuations where CDW was blocked from the shelf throughout much of the year and temporarily upwells and incurs, mixing with on shelf waters hence the ocean temperatures remaining below the temperature of unmodified circumpolar deep water (Dinnimann et al., 2016).

4.5.3. Model Similarities

Of the top six models in the ensemble, given that they have performed well at reproducing ocean temperatures over the historical period and therefore must have produced similar distributions and magnitudes of temperatures, there are some similarities between specific models. This was observed most notably in CCSM4 and CESM1-CAM5, where the former is a subset of the latter models. Furthermore, NorESM1-ME is based on CCSM4 and therefore associated with CESM1-CAM5 model, explaining some of the similarities between these models. Further similarities between the outputs of models in the CMIP5 ensemble can arise from models having the same components. Each AOGCM is made up of a sea ice, land, ocean, and atmosphere model with some models involving additional model components to represent the biosphere etc. For example, CCSM4 and CESM1-CAM5 both use the POP2 ocean model in addition to the CICE model for sea ice, which is also used by NorESM1-ME.

4.5.4. Limitations and Future Work

As was discussed in Chapter 3, the AOGCMs in the CMIP5 ensemble have no inclusion of ice shelf cavities and are therefore capturing realistically the input of shelf meltwater into the ocean (Donat-Magnin et al., 2017). The use of a finite-element sea ice ocean model FESOM by Timmermann and Hellmer (2013) to model projected changes to the ocean circulation surrounding the large Antarctic ice shelves resulted in the identification of a proposed positive feedback. The feedback suggests that additional meltwater will act to freshen the water column resulting in suppressed convection (Hellmer et al., 2012). Should CMIP5 models not capture this feedback it would result in increased unmodified CDW entering cavities, accelerating melt. Therefore, CMIP5 ocean temperatures in the ASE could be underestimating temperature. Furthermore, this freshening would result in reduced

surface warming through reduced heat retention of less saline water; which would, over extended timescales, propagate to subsurface depths (Swingedouw et al., 2008). However, given low sea ice formation rates and subsequent lack of deep-water convection in the ASE, this feedback is unlikely to influence ocean temperatures in the region to as great an extent as other ice shelves such as the Ross and Amery.

Whilst one can make inferences as to the physical processes included in the models that produce these patterns of temperature change, much of the variability is likely associated with the model internal variability. As previously discussed, the 0.08 to 0.1°C variability that is evident in both RCP forcing scenarios is the same despite difference in the magnitude of the forcing, the observed variability could manifest as a result of internal, random variability (Taylor et al., 2012). To further explore this, future work could take composites of periods of high and low variability in order to explore the timings of these changes and consider the associated climatic states over the Southern Ocean to see whether these patterns could be attributed to physical changes in the climate.

4.6. Summary

This chapter has explored the modelled projections of ocean temperature in the Southern Ocean averaged over the 400-700m layer from 2017 to 2100, produced by a subset of CMIP5 models determined in Chapter 3 as the best at reproducing patterns of ocean temperature over the observational period. Both RCP2.6 and RCP8.5 were used and compared. The majority of models are projecting a poleward migration of the ACC in addition to a warming of its core temperatures, consistent with observations in literature. In terms of the relative temperature change over the Southern Ocean, there is some consistency across the subset. For example, most models are showing a warming in the Weddell which is likely a result of enhanced transport of a coastal current associated with the ACC migration. Furthermore, most models are showing a cooling in the Ross which is linked to a freshening of the Ross gyre. Both these patterns of change are evident in both RCP2.6 and RP8.5 but to a far greater extent in the latter.

Exploring the temperatures on shelf in the ASE, averaged over the 400-700 m layer reveals a large range in the absolute temperature over both scenarios. Models converge in their projections of temperature under the RCP8.5 scenario, where those with the lowest temperature over present day increase to the greatest extent over the projection period. Furthermore, models that produce high temperatures on shelf over the observational period and present day show little change over the projection period. The projected temperature change in 2100 relative to present day gives a range of

-0.005 to 1.5°C under RCP8.5 and 0.06 to 0.27°C under RCP2.6. This difference in temperatures and trends illustrates that there are differences in the modelled patterns of ocean circulation that are responsible for heat, and CDW, delivery to the ASE.

Warming local to the ASE is captured in maps of ocean temperature, indicating that warming on shelf in that region is a result of a local mechanism of heating which is attributable to the upwelling of CDW. Furthermore, over the timescale explored, core warming of the warm water mass is likely to be occurring also. Both are supported by the migration of the ACC that is evident in the results, as this has a strengthening impact on westerlies which cause increased transport of CDW toward the ASE continental shelf. The varying trends of warming in addition to the differing magnitude and timing of variability suggest that the models are simulating different mechanisms resulting in different amounts of upwelling. Short term variability is a result of changing quantities of CDW on shelf as determined by changes in atmospheric circulation associated with the SAM and seasonal movement of the ASL. It is challenging to determine why these temperatures and patterns vary as only one variable was analysed.

Chapter 5 : CMIP5 Forced Changes to ASE Glaciers

5.1 Introduction

The BISICLES ice sheet model has not yet been used to explore the projected evolution of the Antarctic Ice Sheet forced with climate model output using the scenarios described in the IPCC 5th Assessment Report. This chapter will use the RCP8.5 forced projections of ocean temperature averaged over the 400-700m depth layer in the ASE, presented in Chapter 4, to calculate an additional melt rate forcing that will force BISICLES from 2017 to 2100. Results show projected grounding line migration and contribution of mass to global sea level under modelled climate scenarios. By performing the runs using two different model initial conditions, an assessment of internal uncertainty is made.

5.2 Data and Methodology

BISICLES is based on the vertically integrated flow model described by Schoof and Hindmarsh (2010). The flow model includes longitudinal and lateral stresses in addition to a simplification of vertical shear stress, this model is better applied to ice shelves and streams (Cornford et al., 2013; Cornford et al., 2015) and is therefore applicable for the ASE ice streams. Furthermore, as these glaciers are fast flowing, the use of an adaptive mesh grid allows for high resolution tracking of the grounding line.

5.2.1. Model Equations

Applying mass conservation to ice thickness and horizontal velocity $\boldsymbol{u}$ gives

$$\frac{\partial h}{\partial t} + \nabla.(\boldsymbol{u}h) = M_s - M_b \ , \tag{1}$$

where M_s denotes surface mass balance and $M_b$is the basal melt rate, which, when discretised, is applied solely to cells in which ice is floating.

Upper surface elevation s is dependent on ice thickness h and bedrock elevation b, given that ice is assumed to be in hydrostatic equilibrium

$$s = \max\left[h + b, \left(1 - \frac{\rho_i}{\rho_w}\right)h\right] , \tag{2}$$

where ρ_i and $\rho_w$describe the respective densities of ice and water.

A two-dimensional stress balance equation is also applied, where the vertically integrated effective viscosity $\varphi\bar{\mu}$ is obtained from both the stiffening factor φ and a vertically varying effective viscosity μ, which was derived from Glen's flow law. This is the stress balance equation

$$\nabla.[\varphi h\bar{\mu}(2\dot{\varepsilon} + 2tr(\dot{\varepsilon})\boldsymbol{I})] + \boldsymbol{\tau_b} = \rho_i g h \nabla s \ . \tag{3}$$

Horizontal strain rate tensor as seen in Eq. 3 is described by the following equation

$$\dot{\boldsymbol{\varepsilon}} = \frac{1}{2}[\nabla \boldsymbol{u} + (\nabla \boldsymbol{u})^{\boldsymbol{T}}] . \tag{4}$$

The vertically varying effective viscosity μ includes representation of vertical shear strains and, given that the flow rate exponent $n = 3$ satisfies

$$2\mu A(4\mu^2\dot{\varepsilon}^2 + |\rho_i g(s - z\_\nabla s|^2) = 1 \tag{5}$$

where the temperature rate dependent factor $A(T)$ is calculated using the formula described by Cuffey and Paterson (2010). Uncertainty in both temperature T and $A(T)$ is accounted for by φ, which is solved through the inverse problem (Nias et al., 2016). Basal traction C is assumed to satisfy a non-linear power law, where m = 1/3

$$\tau_b = \begin{cases} -C|\boldsymbol{u}|^{m-1}\boldsymbol{u}, & h\dfrac{\rho_i}{\rho_w} > r \\ 0, & otherwise \end{cases} . \tag{6}$$

Basal melt rate is determined on ice shelves from $\nabla.(\boldsymbol{u}h)$ and parameterised so that it is spatially varying with melt concentrated closest to the grounding line according to the following equation

$$M_b(x,y,t) = \begin{cases} M_G(x,y)p(x,y,t) + M_A(x,y)\big(1 - p(x,y,t)\big), & floating \\ 0, & grounded \end{cases} , \tag{7}$$

where $p(x, y, t)$=1 at the grounding line which then decays exponentially with increasing distance from the grounding line,

$$p - \lambda^2 \nabla^2 p = \begin{cases} 1, & grounded \\ 0, & elsewhere \end{cases} , \quad (8)$$

with $\nabla p. n = 0$ as a boundary condition.

To concentrate melt rates close to the grounding line, the grounding line proximity parameter p was used, where $p = 1$ at the grounding line and decays exponentially with increasing distance from the grounding line. In the 1D case, $p(x) = exo(-x/\lambda)$ where λ is a scale (= 1000m in this case). The melt rate is found from $M_b(x) = M_{GP}$, where $M_G$is melt at the grounding line and is found by ensuring the following equation is true

$$M_b L = \int_0^L M_G p \ dx \quad . \quad (9)$$

In this case, M_b is the mean melt rate (i.e. the desired forcing obtained from the temperature projection) and L is a length scale of the order of a ice stream width (100 km). For $L \gg \lambda$, $M_b L \approx M_G \lambda$. The melt rate forcing was written in python and read into BISICLES via its embedded python interpreter.

5.2.2. Inverse Problem

BISICLES must be initialised so that the starting conditions are representative of present conditions. The inverse problem, often referred to as the control problem, is performed in order to obtain unmeasured parameters that are required for the model equations. The model requires the input of surface elevation (s) and surface mass balance (M_s) from a modified bedrock topography and a 3D temperature field. These input variables are then used to find the unobservable C, or φ, h, b, and a basal melt rate M_b.

Unknown parameters C and φ are obtained by solving an optimisation problem

$$J = \int_\Omega (|u| - |u_{obs}|)^2 + \alpha_C \int_\Omega (\nabla C)^2 d\Omega + \alpha_\varphi \int_\Omega (\nabla \varphi)^2 d\Omega \ . \quad (10)$$

This minimises the difference between the modelled ice velocity u and the actual observed velocity found by Rignot et al. (2011) through changing $C(x, y)$ and $\varphi(x, y)$. This procedure is iterative and these methods were discussed by Joughin et al. (2009), Macayeal (1992) and Morlighem et al. (2010).

5.2.3. Discretisation

As modelling the whole domain at such a high resolution is computationally demanding, spatially varying resolution is a preferable alternative. Adaptive mesh refinement (AMR) was adopted by a number of ice sheet models including BISICLES to allow for high resolution grounding line to be simulated whilst maintaining coarser resolution in less dynamic regions of the ice stream (Nias et al., 2016). AMR uses an irregular grid that evolves with each time step to contain high resolution to the migrating grounding line. BISICLES uses the Chombo AMR framework that utilised the conservative finite volume method (Cornford et al., 2013). For the simulations performed in this study the mesh grid spacing applied is $\Delta x^l = 2^{-l} \times 4000m$, where l is an integer between 0 and 4 to obtain a maximum resolution of 250m at the grounding line.

5.2.4. Parameter Selection

In order to explore a range of the possible uncertainties associated with parameters identified in the initialisation procedure, two sets of parameters from the Nias (2017) ensemble were used. Nias (2017) performed the inverse problem (Section 5.2.2) to obtain optimum spatially distributing patterns of C, φ, and M_b. This was performed using Bedmap2 (Fretwell et al., 2013), a modified version of this bed (Nias et al., 2016) and a constant 3D temperature field (Pattyn, 2010). Each parameter field was multiplied by a factor that varied each parameter by a halving and doubling, to create vectors of parameters. These vectors were sampled, creating an ensemble of 284 differing parameter combinations. For this investigation two sets of Nias (2017) parameters, which used the modified Bedmap2 topography, were chosen which describe the parameter fields that generated an upper and lower bounds of sea level equivalent estimates. Parameter combinations that resulted in overall negative sea level equivalents or exceeded 95% confidence interval were ignored.

Table 5.1: *Description of the parameter combinations from Nias et al. (2016) that were chosen to use in this investigation. Numbers represent the scaling factor that were applied to each of the spatially varying coefficients obtained from the initialisation procedure.*

	Basal Traction	Stiffening Factor	Melt Rate	Average Rate of SLR over 50 years (mm/yr)
B1052 (L)	0.662	0.742	0.730	0.0024
B1023 (H)	0.576	0.125	0.884	0.68
B0000 (Optimum)	0.500	0.500	0.500	0.27

Chosen parameters are outlined (tab. 5.1). The numbers in the table are representative of the scaling factor that was applied to each of the spatially varying parameters, varied between a halving (0) and doubling (1) of the optimum value (0.5) for each as determined during the control problem. B1052 produces a relatively low rate of SLE as parameters describe the bed to be stickier, ice to be harder and basal melt rate to be higher than the optimum values. In contrast, B1023 produces a relatively high rate of SLE as parameters describe the bed to be stickier (but less sticky than B1052), ice to be softer and melt rate to be higher than the optimum. Each combinations of parameters, when used in the model set up for the following experiments, will therefore be describes as 'L' and 'H'.

5.2.5. CMIP5 Forced Basal Melting

In order to project future evolution of glaciers in the ASE, BISICLES requires a melt rate forcing to be applied to the model, to represent future climate forcing, in addition to the forcing established in the model set-up. Models CESM1-CAM5 and MRI-CGCM3 from the subset were chosen to force BISICLES, in addition to model GISS-E2-R. These models were identified as covering a suitably large range of temperature anomalies over the 21st century. CESM1-CAM5 and MRI-CGCM3 were identified as two of the best performing models; which were used as a mid-range estimate and lower bound, respectively. GISS-E2-R projects the greatest temperature change over the projection period, thus providing an upper bound of temperature change (see appendix).

Projected monthly ocean temperature change, relative to the 2006-2016 mean, was extracted for each of the three CMIP5 models and averaged over the 400-700m layer for the ASE region of 103-113°W and 72-74°S. The RCP8.5 forcing scenario was used; given that the range of projected temperature anomalies in 2100 produced by the subset fully encompasses the equivalent range under the RCP2.6 forcing (see Chapter 3). Finally, the monthly ocean temperature anomalies were averaged to produce annual mean temperature change.

To convert annual mean temperature change to melt rate, the simple linear relationship determined by Rignot and Jacobs (2002) was applied; where a 1°C increase in temperature results in an increase in melt by 10m yr^{-1} (fig. 5.1). This was added to the basal melt rate determined in the optimization procedure, which differs between the two parameter combinations.

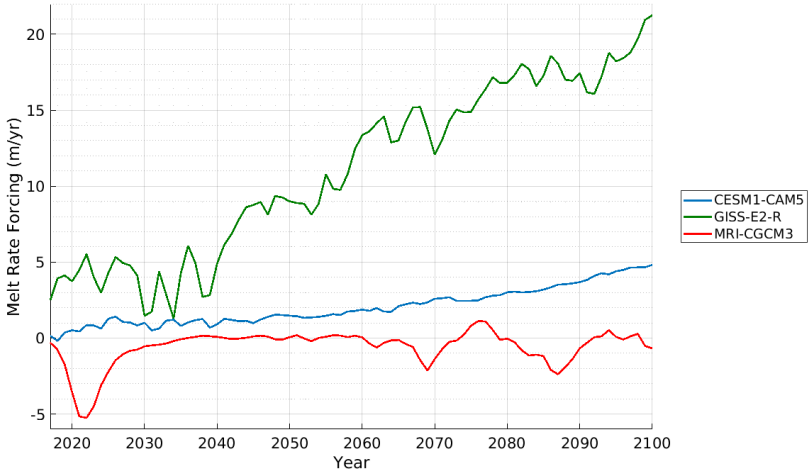

Figure 5.1: *Additional melt rate forcing from 2017 to 2100 that was used as an input for BISICLES. Melt rate was calculated from projected temperature change produced by three CMIP5 models using the relationship described by Rignot and Jacobs (2002).*

5.2.6. Description of Experiments and Analysis

BISICLES was set up with L and H parameter combinations for each of the three CMIP5 model melt rate forcings from 2017-2100; producing six estimates of grounding line positions and mass budgets. The upper and lower range of parameter combinations were used in order to investigate the magnitude of uncertainties arising from choice of initialisation parameters. The projected grounding lines were mapped and discussed, in addition to the overall changes in grounded area over the ASE. Furthermore, an estimate of sea level equivalent from each experiment was calculated from a change in volume above floatation (VAF; Nias et al., 2016)

$$Mass(Gt) = VAF(km^3) \cdot \frac{\rho_i}{\rho_w} \ . \qquad (12)$$

This overall contribution of mass can be converted to a sea level equivalent contribution using a simple relationship that approximates the total area of ocean as 361×10^6 km^3

$$SLE(mm) = \frac{Mass(Gt)}{361} \ . \quad (13)$$

Finally, in order to investigate the specific timing and extent of grounding line retreat for Pine Island, a transect was estimated along the flowline of the glacier and grounding line migration along the transect which bisects the PIG trunk.

5.3. Results

5.3.1. 'L' Parameter Set

Over the 21st century, all CMIP5 forced model experiments experience grounding line retreat (fig. 5.2). Projected retreat extent is similar across the three CMIP5 models but differences between grounding line positions vary across catchments. The three models project similar grounding line positions for PIG and Thwaites, whilst there is a large difference in grounding line position of the PSK glaciers; with GISS-E2-R showing the greatest retreat followed by CESM1-CAM5, with a more modest retreat projected by MRI-CGCM3.

Grounding line retreat for each glacier was mapped, with a colour gradient to distinguish the grounding line positions every two years from 2017 to 2100 (fig. 5.2). Considering Pine Island Glacier, the light-coloured grounding lines show that grounding line migration begins early in the projection period. The sharp transition to a darker grounding line colour indicates that retreat has stabilised mid-way through the projection period before continuing to retreat; which is observed for all CMIP5 models.

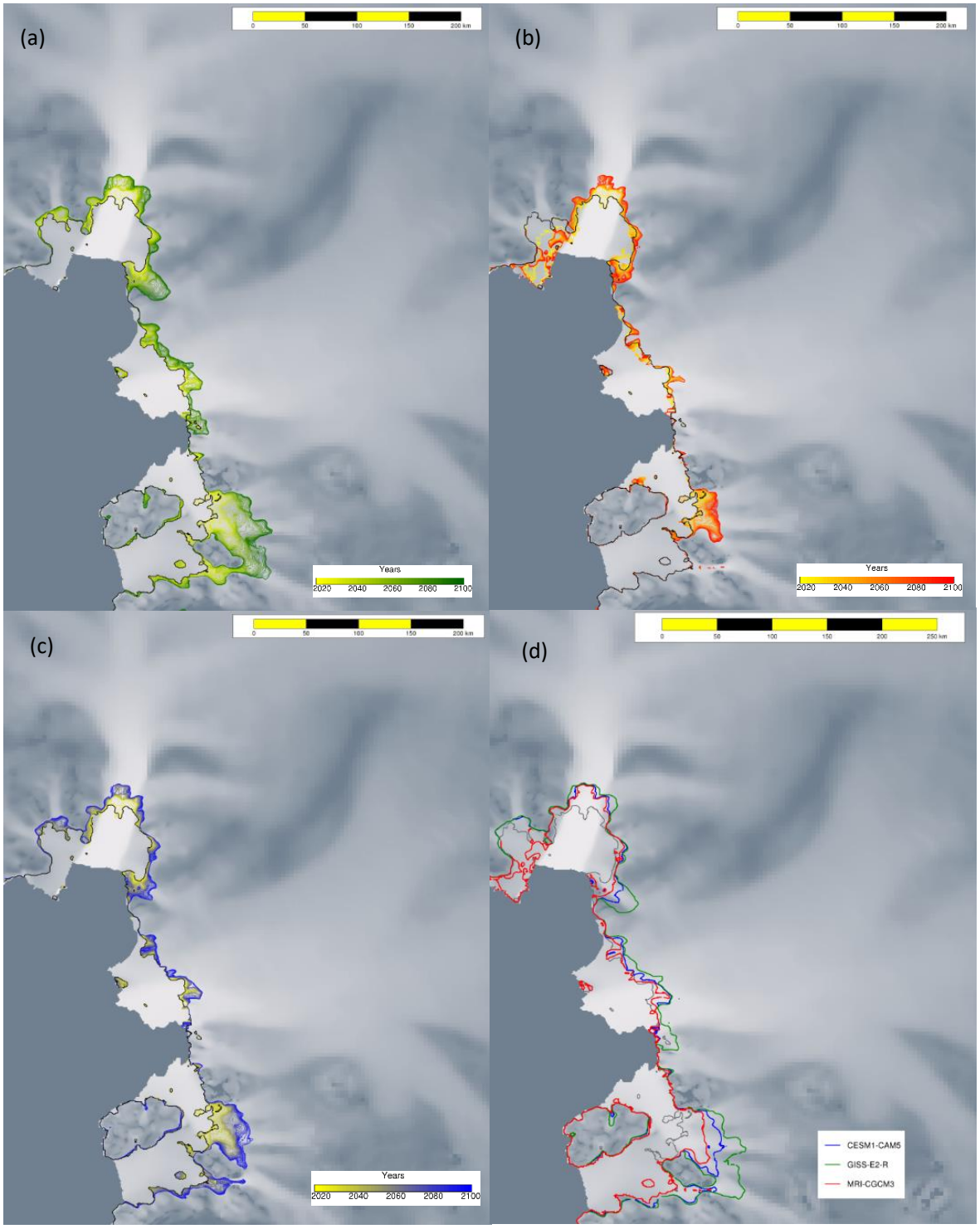

Figure 5.2: *Grounding line retreat in the ASE projected from 2017 to 2100, using the L parameter set, when BISICLES is forced by melt rates parameterised from three CMIP5 model projections of ocean temperature under RCP8.5. (a) GISS-E2-R. (b) MRI-CGCM3. (c) CESM1-CAM5. (d) grounding line positions in 2100 for all three models. Grey grounding line is present day position. Grounding line position was plotted every two years.*

The proposed temporary period of stability during the first half of the century is supported by exploring the grounding line migration along a transect through the centre of PIG (fig. 5.3). Initial rapid retreat of the PIG grounding line by 10 km over the first 5-10 years is present in all three models, despite the large differences in magnitude of forcing over this period (fig. 5.1). There are four periods in which all of the grounding lines remain fixed temporarily, between 10 and 14 km upstream of the initial grounding line, which is consistent for all three CMIP5 models. Furthermore, despite the different magnitudes of melt forcing applied, the extent of grounding line retreat by 2100 for MRI-CGCM3 and CESM1-CAM5 is the same, with both converging to a 24 km retreat upstream. Whereas, from 2060-2100 the GISS-E2-R grounding line remains stationary at a position 25 km upstream of the present-day grounding line.

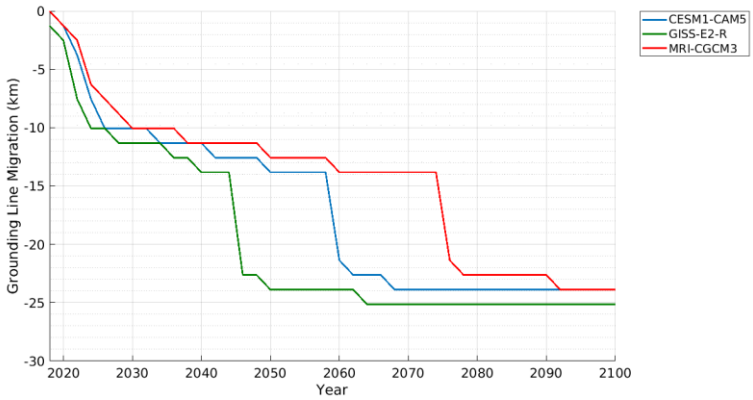

Figure 5.3: *Timing and distance of the Pine Island Glacier grounding line migration from 2017 to 2100 for each CMIP5 model RCP8.5 melt rate forcings using the L parameter set.*

Grounding line retreat of the Thwaites glacier does not take place until the latter half of the projection period, as indicated by the darker contours. This is the case for all three CMIP5 models. There is some difference between models, with MRI-CGCM3 showing very little migration and GISS-E2-R indicating the greatest retreat which appears to be spatially uniform across the 50 km wide trunk. The greatest retreat is observed in the PSK catchment. GISS-E2-R shows retreat to be fairly uniform in time, again exhibiting the greatest retreat over the projection period (fig. 5.2). In contrast, MRI-CGCM3 indicates that the grounding line is stabilising before the end of the century. For both GISS-E2-R and CESM1-CAM5, the grounding line across all three glaciers is retreating. However, under the more modest forcing of MRI-CGCM3, the western branch of Kohler does not appear to be retreating.

Contribution of the ASE to global mean sea level rise indicates a large range in projections which diverge across the century under the differing forcings (fig. 5.4). By the end of the 21st century, there

is a range in sea level contribution estimates from 0 to 15mm depending on the melt rate forcing used. The rate of sea level rise indicates an increase over the period, as exhibited by the nonlinear trend in contribution for CESM1-CAM5 and GISS-E2-R.

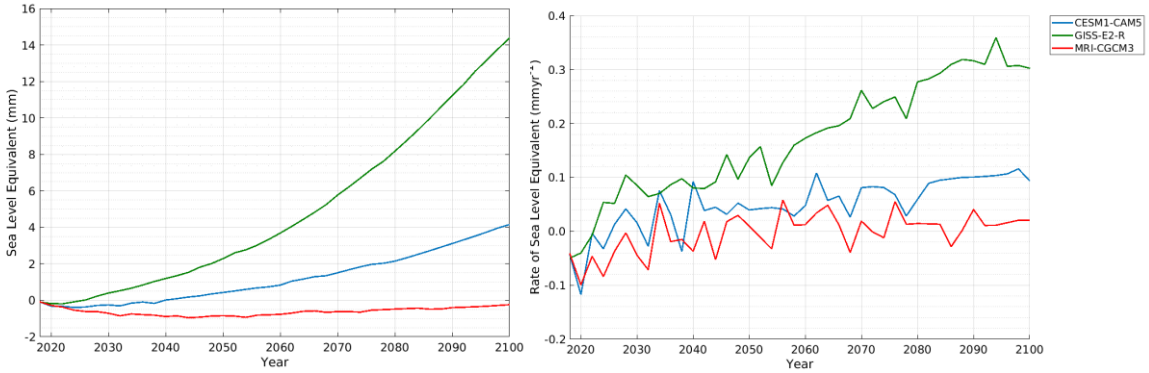

Figure 5.4: *Projected sea level equivalent contribution from the ASE glaciers from 2017 to 2100 from experiments using the L parameter set forced by three CMIP5 models under RCP8.5 (left). Rate of ASE contribution to sea level for each of the three CMIP5 models under RCP8.5 (right).*

Over the first ~6 years of the projection period, the relative contribution of the region to sea level is negative throughout all three experiments. Whilst this would be expected for the MRI-CGCM3 negative melt forcing, this response to the CESM1-CAM5 and GISS-E2-R forcings are unusual. Negative VAF loss and subsequent sea level equivalent is believed to be a result of the initial state mismatch between surface mass balance and flux divergence at the beginning of the experiment, due to the higher ice stiffness and stickier bed.

The contribution of MRI-CGCM3 to global sea level rise remains negative over the entire projection period; though it begins to increase after 2060, resulting in a net -0.02mm contribution to the present-day sea level over the 21st century. A fall in sea level in addition to an increase in grounded area is observed in the northern ice shelf of PIG where the grounding line advances over the first decade of the experiment, coincident with a rapid fall in melt rate forcing (fig. 5.1). Over the course of the projection period, the grounding lines of PIG and PSK retreat along their respective central

trunks, resulting in a loss in grounded area from 2055 onward; coinciding with a positive rate of sea level change (fig. 5.4).

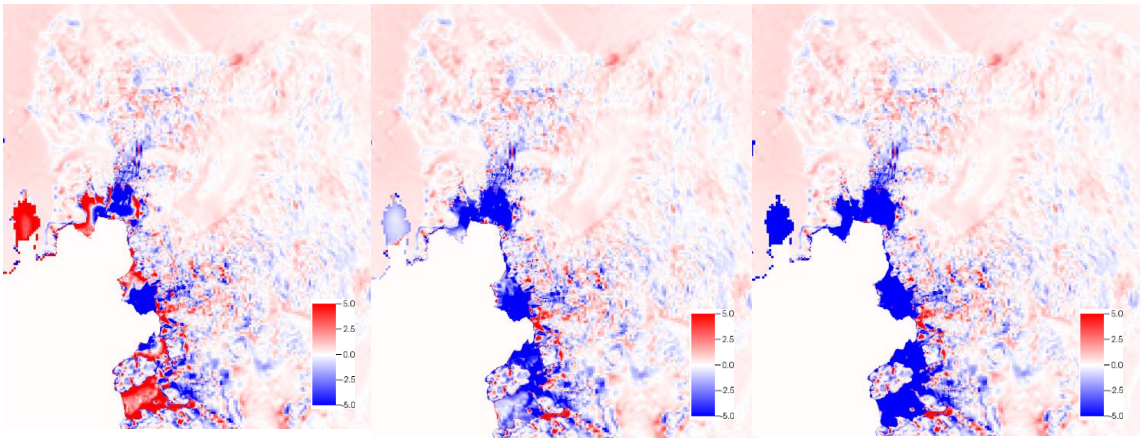

Figure 5.5: *Rate of change of ice thickness (δh/δt) in the ASE in 2020 for each CMIP5 model forcing using parameter set L. MRI-CGCM3 (left), CESM1-CAM5 (middle), GISS-E2-R (right).*

The change in grounded area (fig. 5.5) reveals a similar pattern to the melt forcing, (fig. 5.1) which is particularly noticeable when considering the MRI-CGCM3 experiment. Two periods in which there is a brief period in which the grounded area begins to increase relative to the previous year, indicating grounding line advance, coincide with periods in which melt forcing becomes negative during the 2060s and 2080s.

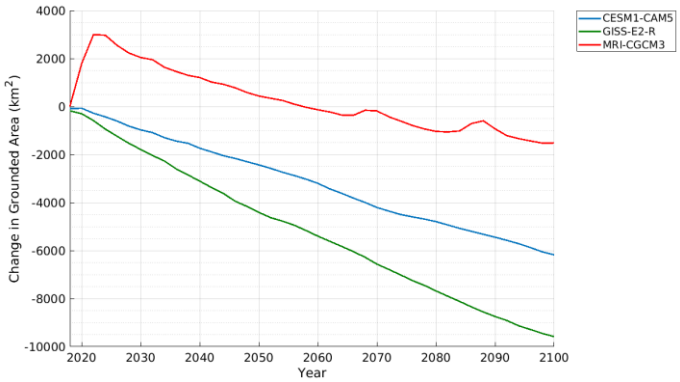

Figure 5.6 *Change in ASE grounded area from 2017-2100 relative to the 2016 area for each experiment using CMIP5 model RCP8.5 forcing using the L parameter set.*

In contrast, CESM1-CAM5 and GISS-E2-R which show linear, flat trends in change in grounded area despite GISS-E2-R showing notable variability in its additional melt forcing. This could indicate that

once the melt rate forcing is of a certain magnitude, the grounding line sensitivity to melt variability is decreased.

5.3.2. 'H' Parameter Set

The projected grounding line positions for the experiments initialised with the H parameter set are considerably different to those using L (fig. 5.6), with all grounding lines showing greater retreat. In all cases, the grounding lines of PIG and Thwaites have merged.

Exploring PIG, whilst MRI-CGCM3 appears to show slowed retreat and some stabilisation toward the end of the century, which is also observed for CESM1-CAM5, GISS-E2-R shows continued rapid retreat over the entire period. With increasing distance between grounding line positions further upstream, it is indicated that retreat is accelerating. This is supported by the timing of grounding line retreat (fig. 5.7) projecting an exponential retreat. The grounding line position retreats 130 km upstream over the century. This compares with the modest 13 km difference between 2100 grounding line positions of MRI-CGCM3 and CESM1-CAM5, experiencing 30 km and 43 km retreat respectively. Additionally, MRI-CGCM3 exhibits grounding line advance at the northern side of PIG, before continuing to retreat marginally and reach a fixed position. Whilst the retreat of the PIG grounding line is generally confined to the main trunk, under the GISS-E2-R forcing there is an extended retreat of the southern side of the glacier which appears to migrate upstream into one of the tributaries.

The difference in Thwaites Glacier grounding line positions in 2100 is primarily evident in the western side of the trunk. Retreat of the grounding line upstream results in a widening of the region in contact with the ocean. Furthermore, PSK retreat is the most similar to the low parameter projections, with GISS-E2-R exhibiting the greatest extent of grounding line retreat, followed by CESM1-CAM5 and MRI-CGCM3. All three ice streams merge and become one, which is evident in each of the forcing scenarios. This illustrates almost complete retreat and disappearance of PSK. Complete disappearance of PSK was noted and found by Nias et al. (2016). It was observed over the recent historical period by Scheuchl et al. (2016) that rapid retreat observed will continue into the future, even in absence of additional forcing.

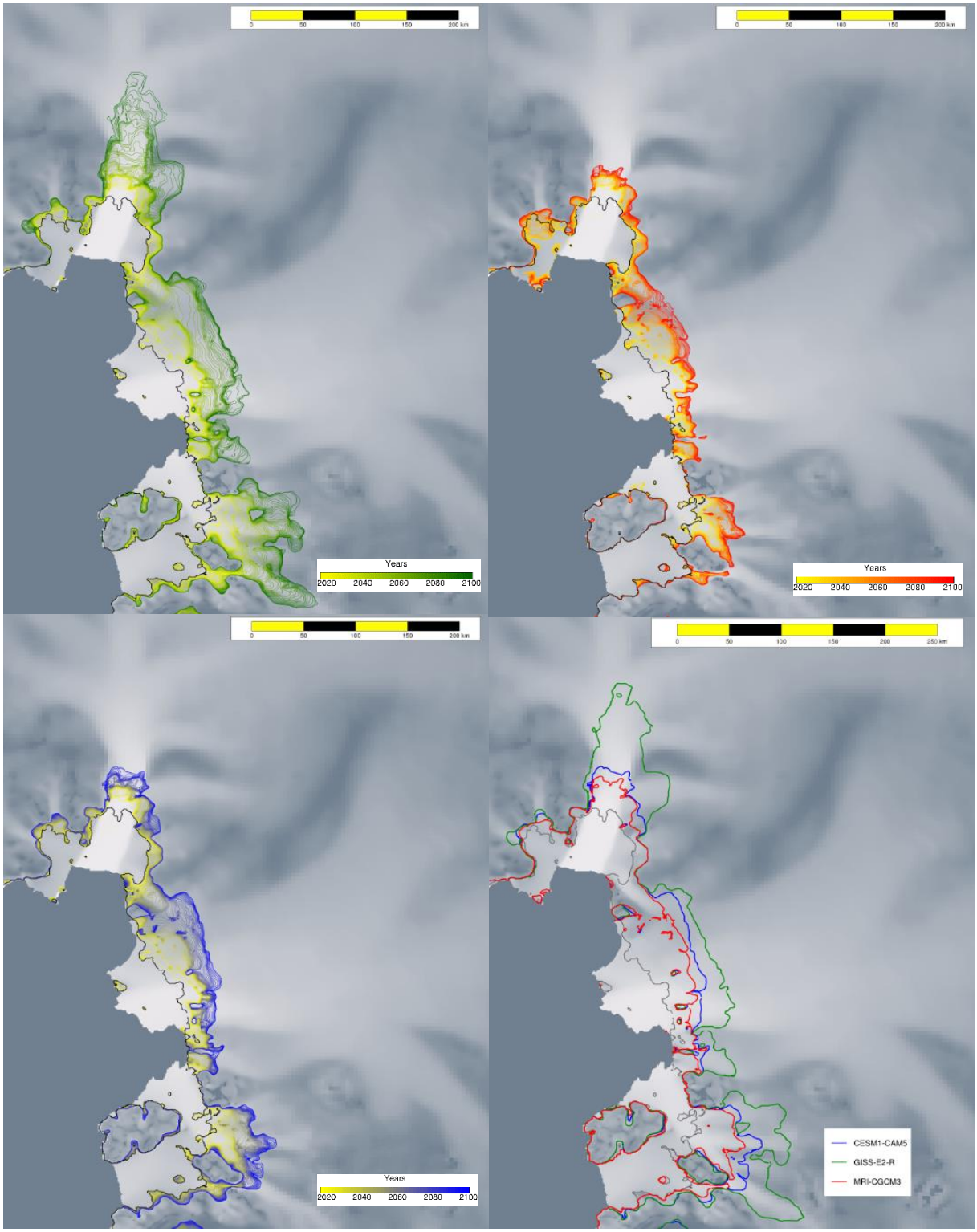

Figure 5.7: *Grounding line retreat in the ASE projected from 2017 to 2100, using the H parameter set, when BISICLES is forced by melt rates parameterised from three CMIP5 model projections of ocean temperature under RCP8.5. (a) GISS-E2-R. (b) MRI-CGCM3. (c) CESM1-CAM5. (d) grounding line positions in 2100 for all three models. Grey grounding line is present day position. Grounding line position was plotted every two years.*

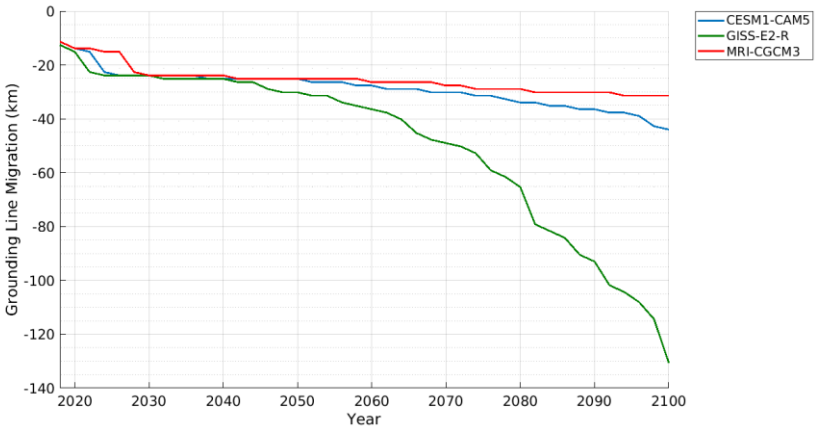

Figure 5.8: *Timing and distance of the Pine Island Glacier grounding line migration from 2017 to 2100, for experiments forced by three CMIP5 model outputs.*

Examining the PIG grounding line retreat over the course of the century for each model reveals a 30 to 130 km difference in the projected position of the grounding line in 2100, relative to present day. Both CESM1-CAM5 and MRI-CGCM3 indicate that the majority of the retreat is occurring in the first 10 years of the projection period, both models showing retreat of ~24 km initially, followed by a respective gradual ~8 km and ~20 km retreat over the remaining 70 years of the century. All models indicate the same magnitude and extent of retreat until 2040, after which the projected grounding lines diverge. Whilst GISS-E2-R undergoes the initial 24 km retreat over the first 6 years of the projection, it remains situated roughly around this point until around 2042 where the rate of grounding line retreat appears to accelerate throughout the rest of the century, proceeding to retreat over 100 km in 60 years. This coincides with the acceleration in applied melt rate forcing (fig. 5.1)

The contribution of mass to global mean sea level is largely different from the projections initialised with the low parameters. Sea level contribution projected by MRI-CGCM3 and CESM1-CAM5 appear to be almost linear, reaching a contribution by the end of the century of 55mm and 70mm respectively. In contrast, GISS-E2-R appears to increase linearly from 2017 to 2060 before a brief acceleration, resulting in an increased linear gradient. The model projects a contribution of 120 mm to global mean sea level rise.

The rate of SLE contribution diverges across the projection period, with GISS-E2-R exhibiting an acceleration from 2040 until the end of the 21st century. This acceleration period coincides with the increased melt forcing applied (fig. 5.1). In contrast, the trends reveal the near linearity of the CESM1-CAM5 projection, with a gradual increase in the rate of sea level rise from around 2050 onward. MRI-

CGCM3 projects a decrease in the rate of SLR, with a gradual deceleration. All three models begin the projection with a rate of sea level contribution of around 0.8mm/yr.

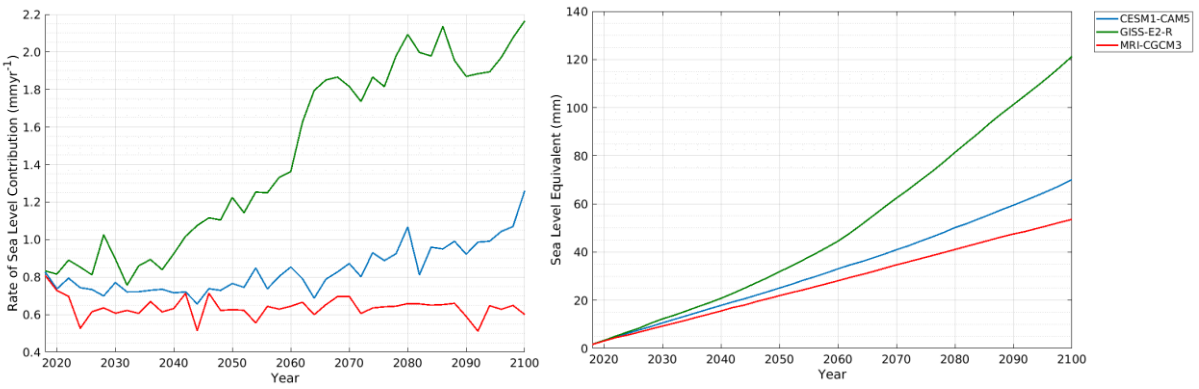

Figure 5.9: *Projected sea level contribution from the Amundsen Sea glaciers from 2017 to 2100 using the H parameter set from experiments forced by three CMIP5 models (top). Rate of Amundsen Sea contribution to sea level for each of the three CMIP5 models (bottom)*

As occurred under the low initialised experiment, the MRI-CGCM3 model exhibited an increase in grounded area at the beginning of the century (fig. 5.9) which was the result of an advance in the grounding line of the northern side of the PIG ice shelf. Change in grounded area therefore effectively mimics the behaviour of the forcing when the magnitude of the forcing is low. This subsequently retreated again, as did the grounding line over the remainder of the domain, in addition to the rate of sea level contribution. In contrast, GISS-E2-R and CESM1-CAM5 show unabated retreat throughout the projection, with GISS-E2-R appearing to show an acceleration in loss of grounded area from 2050 onward.

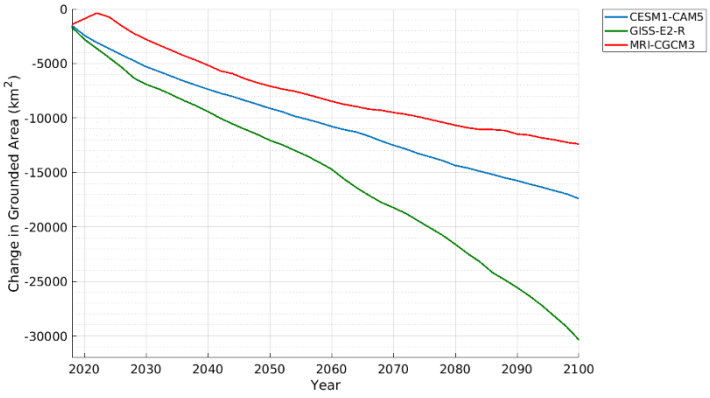

Figure 5.10 *Change in ASE grounded area from 2017-2100 relative to the 2016 area for each experiment using CMIP5 model RCP8.5 forcing using the H parameter set.*

5.4 Discussion

Using RCP8.5 scenario CMIP5 model projections to force BISICLES, indicates a broad range of projected sea level contribution between -0.02 cm to 12.3 cm from the ASE alone, by the end of the 21st century. This upper limit is concurrent with the 12 cm upper limit found by Nias (2017). In comparison, Ritz et al. (2015) indicate that the ASE will contribute 25 cm by 2100 (95% quantile), which is more than double the upper bound projected in this study. Ritz et al. (2015) used a coarse grid model with a prescribed grounding line which therefore could be overpredicting grounding line retreat, as opposed to a freely evolving, resolved grounding line. Moreover, Levermann et al. (2014) forced five ice sheet models forced with RCP8.5 projections until the end of the century and found the whole Antarctic contribution of 4 cm and 21 cm to global sea level rise, though estimates are likely to be offset by the inclusion of increased accumulation under atmospheric warming (Frierler et al., 2015). Levermann et al. (2014) used coarse resolution ice sheet models to obtain these estimates, with a heavily parameterised the grounding line. Considering the contribution of mass to sea level from ice discharge alone, the IPCC AR5 provide a likely range of -1 cm to 16 cm by 2100, from the entire continent; again, produced using coarse resolution models. In contrast, this investigation used an adaptive mesh grid to track the grounding line position at high resolution of 250 m, thus our modelled results determine a more realistic range of projections.

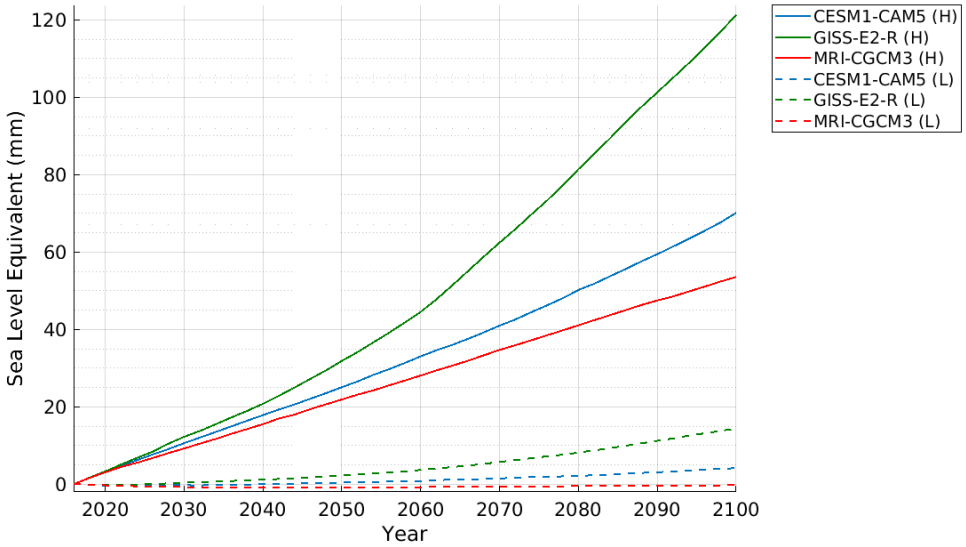

Figure 5.11**: Projected sea level equivalent contribution from the ASE over 2017-2100 forced with each of the CMIP5 model RCP8.5 melt forcings for both L and H parameter **sets.

There is a substantial difference in the projected ASE response to forcing when initialised with two differing sets of parameters, with a possible range of -0.2 cm to 1.5 cm for the L set, contrasting with 5.4 cm to 12.3 cm using H. Extensive grounding line retreat, and subsequent decreased VAF, occurring

over the simulations initialised with the H parameters is expected, given that ice stiffness was scaled so that it is just over half of the value obtained in the optimisation procedure. Consequently, low ice viscosity results in softer ice which is more deformable, causing faster flow and thus increased delivery of ice mass to the grounding line (Nias et al., 2016). Considering the basal traction coefficients, the H combination experiences a more slippery bed than L, meaning that faster velocities are likely to occur, which explains the greater flux over the grounding line and subsequent large sea level rise. Finally, the baseline melt rate forcing between the two parameter sets are different, with H experiencing greater underlying melt forcing than L, meaning the two different configurations experience different melt rate forcings. The impact of these differing parameters on response to melt forcing was illustrated, where CESM1-CAM5 using L has greater velocities in 2050 than H (fig. 5.12). The substantial difference in the overall contributions to global mean sea level that is dependent on the initialisation conditions, illustrates the importance of this optimization process and thus the large range of uncertainty that can develop within the configuration of the BISICLES ice sheet model.

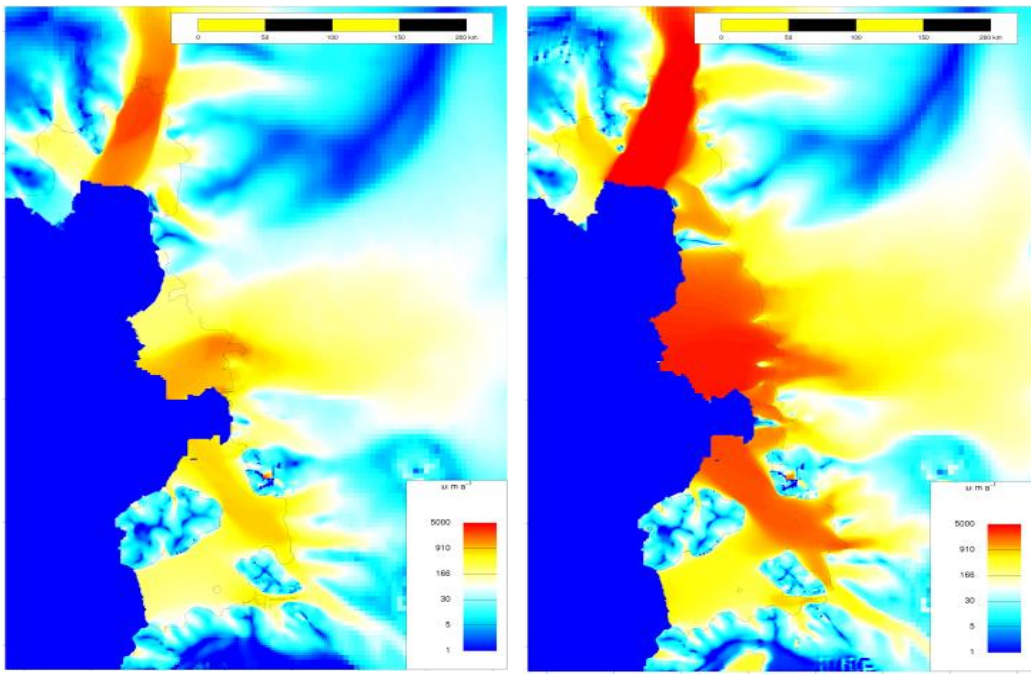

Figure 5.12: *Velocity magnitude maps of the ASE glaciers in 2050 for low parameters (left) and high parameters (right) using the CESM1-CAM5 melt rate forcing.*

This difference in baseline melt rate forcings partially explains the different initial rates of sea level contribution ranging between -0.5 mm yr^{-1} and 0.8 mm yr^{-1} in 2017 for L and H parameters respectively. This wide range of rates in 2017 exceed estimates of 0.33 ± 0.05 mm yr^{-1} from both using Cryosat from 2010 to 2013 (Mcmillan et al., 2014) and 0.27 ± 0.004 mm yr^{-1} from the input output method (Medley et al., 2014). In comparison, the projected end of the century (2091-2100 mean)

upper limit of sea level equivalent contribution is 0.32 mm yr^{-1}. This suggests that even under the most extreme forcing scenario, forced with GISS-E2-R, there will be no acceleration in the contribution of the region to global sea level rise for this parameter set up. In contrast, the mean rate of sea level contributions over the last decade of the 21st century range from 0.63 mm yr^{-1} to 2.02 mm yr^{-1}.

Relating the range of responses to the differing melt forcings applied, it appears as though the ice dynamics are more sensitive to the applied melt rate forcing when the parameters are initialised with the H parameters. There is a more distinct difference between the 21st century projected grounded line position and resulting sea level contribution over the century when forced with H. Using L, all three models project similar 21st century grounding lines in PIG and Thwaites Glacier whereas this differs considerably under the high set up. Specifically, the final grounding line position for PIG differs by 100 km under H and 1 km under the L set up. Further, comparing the range of sea level contributions for the two parameter combinations indicates a range of -0.02 cm to 1.5 cm for L parameters in 2100, which contrasts with the range from 5.4 cm to 12.3 cm using H, indicating that the range in SLR contribution is 5 times greater for the H parameters than L parameters.

The timing and extent of retreat of the PIG grounding line, for both sets of initial conditions, indicates that topography provides periods in which the grounding line retreat is pausing temporarily due to grounding on locally prograde bedrock (Schoof, 2010; Joughin et al., 2010). The same is illustrated in the clustering of grounding lines of Thwaites Glacier (fig. 5.7) This highlights the importance of using high resolution, reliable topographic datasets (Sun et al., 2014; Nias et al., 2018); for example, Durand et al. (2011) proposed that a 1 km resolution was necessary for ice sheet models. It should be noted therefore that the resolution of Bedmap2 varies between 5 and 15 km (Fretwell et al., 2013). Using the modified Bedmap2 dataset presented by Nias et al. (2016), under the low parameters, all three models indicate a sustained grounding 24-25 km behind the present-day grounding line. This grounding position is consistent with the topographic ridge identified by Vaughan et al. (2006), suggesting that the local prograde bed is stabilising the retreat of the grounding line. Moreover, this pause in grounding line retreat at ~24 km is also evident for the experiments initialised with H parameters, which indicates that regardless of the defined model parameters for initialisation, topography is influencing the ice dynamics.

Considering the experiments run with the low parameters, concurrent with findings in literature, once grounding line retreat of PIG was initiated, the rate of retreat appears to be insensitive to the

magnitude of the melt rate forcing (Ritz et al., 2015; Schoof, 2007); inferring that retreat could be self-sustaining regardless of changes in this forcing (Turner et al., 2017). Looking at the L set up, this is particularly notable for the initial ~10 years of the projection, where melt forcing is most notably different across the three models, but the rate of grounding line retreat is the same. In contrast, once the models have reached a period in which their grounding line is temporarily stabilised, the duration for which they remain stabilised is dependent on the magnitude of applied melt forcing. For example, a temporary transient period 14 km upstream from the present-day grounding line lasts for <5 years when forced with GISS-E2-R compared with >10 years for the modest MRI-CGCM3 forcing. This finding is conducive to the findings of Joughin et al. (2010) whereby the sensitivity of the grounding line to melt forcing is dependent on topography. This is most notable in the L experiments, however, can also be observed in H but it is harder to recognise given the greater retreat over shorter time periods. Future work might involve exploration of the durations of grounding with relation to the temperatures applied in order to investigate the possibility of a "tipping point" whereby melt forcing that exceeds this, causes unabated retreat from a local transient period of stability.

Using L parameters, there is little to no difference in the response of the grounding line of Thwaites Glacier between the 20m yr^{-1} melt forcing of GISS-E2-R compared with that of 0.2m yr^{-1} projected by MRI-CGCM3, given their grounding lines by the end of the century residing in the same place. This highlights the insensitivity of Thwaites Glacier to melt rate forcing and thus reiterates that Thwaites Glacier ice shelf, through its unconstrained lateral boundaries, provides less of a buttressing on grounded ice (Macgregor et al., 2012; Dupont and Alley, 2005; Parizek et al., 2013). On the other hand, the response of Thwaites Glacier to the same forcings, when initialised with different conditions, is dramatically different. Where the H parameter set indicates noticeably different grounding line positions by the end of the projection period. It could therefore be inferred that Thwaites Glacier is particularly insensitive to melt forcing when initialised with low ice stiffness, but sensitive under conditions with softer ice. Joughin et al. (2014) found that retreat of Thwaites Glacier is modest over the 21st century but could experience rapid and widespread retreat should forcing be of a sufficient magnitude and duration. Whilst this is the case for the L parameter set, instability is evident in our high simulations over the 21st century, the grounding line appears to retreat dramatically into the embayment, merging with the grounding line of PIG, with the 45 km long grounding line increasing in length as part of a positive feedback to exacerbate mass loss of the glacier.

The three differing melt rate forcings applied to the model experiments capture a large proportion of the range of projected temperature anomalies on shelf in the ASE. The response of MRI-CGCM3 effectively provides an idea of a control run, with the exception of two periods of variability over the century. It must be recognised that the H conditions when forced with MRI-CGCM3, which has an overall melt rate forcing around 0 m yr^{-1}, results in a 5 cm rise in global mean sea level rise. This highlights that even in the absence of additional melt rate forcing, should ice have a relatively low viscosity in addition to a higher initialised baseline melt rate, the region could be undergoing exceptionally rapid grounding line retreat.

5.4.1. Limitations

Melt rate forcing was assumed to be uniform across the three catchments, in reality there is a prominent spatial gradient in temperature and thus each ice stream will experience largely different additional melt rate forcings. In an observational study, Wåhlin et al. (2013) identified that CDW is warmer in the eastern part of the embayment as the water interacting with the PSK glaciers were cooled and modified through ice-ocean interactions. Therefore, by applying a uniform temperature to all glaciers in the embayment we are removing the differences in forcing that will exist between ice streams in the embayment.

According to the depression of the pressure melting point with depth, melt rate parameterisations provide higher rates closer to the grounding line where the ice shelf thickens. Though it considers the thermal driving caused by increased pressure, such a parameterisation neglects a number of physical components such as the geometry of the sub shelf cavity and the influence of glacial outflow. The former could result in a limitation of the simulated heat delivery to the grounding line whilst the latter could be neglecting the influence of glacial meltwater plumes beneath the ice shelves. Donat-Magnin et al. (2017) suggest that the use of ocean temperature data that was simulated by a model that does not include representation of ice shelves will likely be wrong, thus the use of these forcings for ice sheet modelling will produce questionable projections of grounding line retreat.

Similarly, to the experimental design of Gladstone et al. (2012), our experiments neglect any uncertainty associated with the ocean temperatures simulated by the climate models under each forcing scenario. Therefore, the results are less of a representation of the response of BISICLES to the specific scenarios, more a demonstration of the way in which BISICLES is responding to the prescribed ocean temperatures. By comparing this output with similar model simulations under these forcing scenarios one might have a better idea of whether CMIP5 output alone is sufficient for forcing the

model in comparison to experiments using cavity resolving ocean models and regional ocean models as an alternative, higher resolution forcing.

There are limitations with the calculation of the melt rate forcings for this study. Whilst the linear relationship established by Rignot and Jacobs (2002) was used, Holland et al. (2008) demonstrate that there are a broader range of ways in which to mathematically equate temperature to melt forcing. Their investigation suggests that the relationship is quadratic, through considering the impact of velocity on ice shelf melting. Should time have permitted, both the linear and quadratic relationships would were used and compared, and the uncertainty considered. However, numerous studies have identified that even a quadratic relationship is too simplistic as this neglects features such as melt plumes and their incision into ice shelves, in addition to the general geometry of the cavity. It has thus been suggested that the next step in advancements of ice sheet modelling lie in the use of coupled ice sheet-cavity resolving ocean models (Naughten et al., 2018). De Rydt and Gudmundsson (2016) in their use of an offline coupling between an ice flow model and an ocean general circulation model, demonstrate that simple melt rate parameterisations with independent climate model output produces a 40% overestimation of mass loss over a 50-year timescale, this may be the case for our estimations of global mean sea level contributions from the ASE.

Our investigation has applied a constant temperature field that represents present day conditions (Pattyn, 2010). A study by Golledge et al. (2015) investigates the contribution of atmospheric and oceanic forcing to projections of grounding line retreat using PISM. The study found that whilst ocean forcing plays a greater role in driving ice sheet evolution over centennial timescales, over multi-millennial timescales the role of atmospheric warming becomes increasingly more important in driving mass changes in Antarctic, primarily through increased ice creep. Therefore, whilst we have held atmospheric forcing constant over our relatively short run, should this investigation look to make projections further in the future, application of a changing atmospheric forcing would be necessary. Furthermore, additional precipitation as a result of atmospheric warming (Frierler et al., 2015) could alter estimates of sea level contribution from the region.

5.5 Summary

This chapter has demonstrated the projected response of ice streams in the ASE when forced with ocean temperature output from CMIP5 models from present day to the end of the 21st century. Using two differing combinations of values for the basal traction coefficient, ice stiffening factor and baseline melt forcing, the range in responses were explored taking into account possible variability

within the BISICLES model configuration. The resulting contribution to sea level ranges from -0.02 cm to 12.3 cm, depending on choice of melt rate forcing in addition to choice of parameters. Results indicate that the response of the ice stream varies greatest according to use of parameters, 5.4 cm to 12.3 cm, as opposed to the choice of applied melt rate forcing, -0.02 to 1.5 cm. This highlights the importance for models to capture appropriate parameters that represent realistic conditions in order to produce reliable sea level contribution estimates. These estimates are half those projected by Ritz et al. (2015) for the ASE, indicating that studies using coarse resolution models without capabilities of resolving the grounding line are overestimating projected mass loss in the region.

The stepped retreat of the grounding line of PIG, in response to melt forcing, indicates that grounding lines are most sensitive to the magnitude of the melt forcing when they are temporarily stabilised on a topographic highpoint. However, once retreat was initiated, grounding lines are insensitive to the applied melt forcing. Regardless of the parameters used in the model configuration, topography is of great importance on the grounding line position and thus stability of the ice streams.

Chapter 6 : Conclusions

6.1. Research Objectives

The first aim of this investigation was to evaluate the ability of CMIP5 models to reproduce observed ocean temperature patterns over the observational period (1979-2016). The results show that, given the large differences in their physics, resolutions, configurations and model components, the CMIP5 models differ widely in their ability to capture observed temperature over the observational period. A range in model error of 1.66 to 2.47°C, in addition to a majority of models having positive mean bias errors, indicates that models are generally overestimating temperatures over much of the Southern Ocean; consistent with other studies. Inability for the models to capture the timings and variability on shelf in the ASE is likely due to their inability to capture small scale coastal processes, due to their coarse resolution. Despite these errors, the chosen subset of models, collectively, are able to capture the range of temperature on shelf in the ASE over the observational period. This, in light of the large errors and uncertainties associated with the ensemble, indicates that whilst no single model is particularly "good", a subset of CMIP5 AOGCMs could provide reliable projections of ocean temperature on a smaller geographical scale. The assessment of models in this investigation, however, is severely limited by the poor data coverage over the Southern Ocean, particularly local to the ASE, which has made model assessment challenging and uncertain.

The second objective required an exploration of the temperatures in the Southern Ocean in addition to local ocean temperatures in the ASE, given that these will be the temperatures interacting with ice shelves in the region. Overall temperature change in the Southern Ocean relative to present day indicates a greater warming at lower latitudes away from the ice sheet. Additionally, a local region of warming in the ASE was recognised in some model projections, likely indicating increased intrusion of warm CDW onto the continental shelf. Considering mean temperature on shelf in the ASE, there is a range in the RCP8.5 forced temperature mean anomalies in 2100 of -0.05°C to 1.4°C, relative to the present day. The models with an increase in temperature over the projection period are believed to be illustrating an increase in the depth of the CDW layer on shelf, through greater extents of upwelling and incursion, hence an increase in the mean temperature of the region. Furthermore, the differing extents of temperature variability reflect the likely seasonal, interannual and multiannual changes to CDW delivery on shelf, dictated by patterns in atmospheric and oceanic circulation. Models with initial high temperatures over the present day and observational period could indicate that a thick

layer of this warm water is a permanent feature on shelf, hence the negligible temperature change over the period. In contrast, models with lower present-day temperatures exhibit large magnitude trends with high variability suggesting that the temperature on shelf is sensitive to the change in CDW upwelling that is driven by patterns in circulation. The large range in temperatures on shelf projected over the century illustrate the differences between the way in which models are representing both the core temperature of CDW, in addition to the processes of coastal atmospheric and oceanic circulation, thus impacting the quantities of CDW modelled on shelf.

Estimates of projected SLR over the course of the century were obtained through using projected ocean temperature as a melt rate forcing of BISICLES, thus achieving the third objective. As would be expected, models with the greatest positive temperature change over the century are resulting in the greatest grounding line retreat over PIG, Thwaites and PSK glaciers. Therefore, increased CDW delivery to the region is driving increased melting of glaciers, as has been suggested in literature. As a result, applied melt rate forcings range from ~0 m yr^{-1} by the end of the 21st century to ~20 m yr^{-1}. Exploring the upper and lower limits of the ice sheet model parameter combinations, forced with the same melt forcings, however, indicates that the range in SLR estimates varies from -0.02 to 1.5 cm to between 5.4 cm to 12.3 cm depending on initialisation of the model. Furthermore, the melt forcing with almost no change over the projection period, when considered as a control run, could experience a range in between -0.02 to 5.4 cm of SLR depending on these set-up parameters. Therefore, the modelled projected mass loss in the ASE is more sensitive to the choice of ice sheet model parameters, ice stiffness and basal traction coefficients, than the applied additional melt rate forcing. Results have also shown evidence of MISI, where retreat of the PIG grounding line, once initiated, occurs at the same rate regardless of the applied melt rate forcing; this is evident for simulations using both parameter sets.

6.2. Future Work

Should time have permitted, experiments would be performed for all CMIP5 models, forced with both RCP2.6 and RCP8.5 for both of the chosen H and L combinations of initial parameters. Further, experiments would be performed using the optimum parameters determined in the control problem. This would have enabled us to capture the distribution of projected SLR, for four separate ensembles, and thus work out the confidence intervals and most likely projections. Finally, a weighting would be applied, based on the performance metrics calculated for each model.

6.3. Concluding Remarks

The overall aim of this investigation was to explore the suitability of using ocean temperature projections from CMIP5 models to force BISICLES in the ASE. Having discussed model errors, it has been suggested that the coarse resolution of the CMIP5 AOGCMs is likely causing models to misrepresent the small-scale coastal processes resulting in onshore flow of CDW in the ASE; which is the primary driver of basal melting of ice in the region. Though the timing and variability of temperature change in the region has not been captured, the range of observed temperatures in the ASE has been well captured by a subset of models. Thus, use of an ensemble or subset of AOGCMs, instead of a singular model, is beneficial when using climate model output to force standalone ice sheet models. Therefore, by forcing BISICLES with projections from a number of models, a range in of the projected response to varying possible forcings has been considered. However, the uncertainty in ice-sheet parameters, such as ice stiffness and basal traction coefficients, is as, if not more, important as the uncertainty associated with AOGCM climate projections for calculating SLR in the ASE over the 21st century.

Chapter 7 : Bibliography

Alley, R.B., Clark, P.U., Huybrechts, P. and Joughin, I. (2005). Ice-sheet and sea-level changes. *Science. 310*(5747). pp.456-460.

Arneborg, L., Wåhlin, A.K., Björk, G., Liljebladh, B. and Orsi, A.H., (2012). Persistent inflow of warm water onto the central Amundsen shelf. *Nature Geoscience*, *5*(12), p.876.

Arthern, R.J. and Williams, C.R. (2017). The sensitivity of West Antarctica to the submarine melting feedback. *Geophysical research letters*. 44(5). Pp. 2352-2359.

Asay-Davis, X.S., Jourdain, N.C. and Nakayama, Y. (2017). Developments in simulating and parameterizing interactions between the Southern Ocean and the Antarctic Ice sheet. *Current Climate Change Reports*, *3*(4), pp.316-329.

Assmann, K.M., Jenkins, A., Shoosmith, D.R., Walker, D.P., Jacobs, S.S. and Nicholls, K.W. (2013). Variability of Circumpolar Deep Water transport onto the Amundsen Sea continental shelf through a shelf break trough. *American Geophysical Union.*

Bamber, J.L., Riva, R.E., Vermeersen, B.L. and LeBrocq, A.M. (2009). Reassessment of the potential sea-level rise from a collapse of the West Antarctic Ice Sheet. Science. 324(5929). pp.901-903.

Bamber, J.L., Vaughan, D.G. and Joughin, I. (2000). Widespread complex flow in the interior of the Antarctic ice sheet. Science. 287(5456). pp.1248-1250.

Bintanja, R., Van Oldenborgh, G.J., Drijfhout, S.S., Wouters, B. and Katsman, C.A. (2013). Important role for ocean warming and increased ice-shelf melt in Antarctic sea-ice expansion. *Nature Geoscience*, *6*(5), p.376.

Bracegirdle, T.J., (2013). Climatology and recent increase of westerly winds over the Amundsen Sea derived from six reanalyses. International Journal of Climatology, 33(4), pp.843-851.

Bracegirdle, T.J., Connolley, W.M. and Turner, J., (2008). Antarctic climate change over the twenty first century. *Journal of Geophysical Research: Atmospheres*. 113(D3).

Church, J.A., Clark, P.U., Cazenave, A., Gregory, J.M., Jevrejeva, S., Levermann, A., Merrifield, M.A., Milne, G.A., Nerem, R.S., Nunn, P.D. and Payne, A.J. (2013). *Sea level change.* PM Cambridge University Press.

Collins, M., R. Knutti, J. Arblaster, J.-L. Dufresne, T. Fichefet, P. Friedlingstein, X. Gao, W.J. Gutowski, T. Johns, G. Krinner, M. Shongwe, C. Tebaldi, A.J. Weaver and M. Wehner, (2013): Long-term Climate Change: Projections, Commitments and Irreversibility. In: Climate Change

2013: The Physical Science Basis. Contribution of Working Group I to the Fifth Assessment Report of the Intergovernmental Panel on Climate Change [Stocker, T.F., D. Qin, G.-K. Plattner, M. Tignor, S.K. Allen, J. Boschung, A. Nauels, Y. Xia, V. Bex and P.M. Midgley (eds.)]. Cambridge University Press, Cambridge, United Kingdom and New York, NY, USA.

Comiso, J.C. and Nishio, F. (2008). Trends in the sea ice cover using enhanced and compatible AMSR-E, SSM/I, and SMMR data. *Journal of Geophysical Research: Oceans.* 113(C2).

Connolley, W.M., (1997). Variability in annual mean circulation in southern high latitudes. *Climate Dynamics*, *13*(10), pp.745-756.

Cook, A.J. and Vaughan, D.G. (2010). Overview of areal changes of the ice shelves on the Antarctic Peninsula over the past 50 years*. The cryosphere*. 4(1). pp.77-98.

Cornford, S.L., Martin, D.F., Graves, D.T., Ranken, D.F., Le Brocq, A.M., Gladstone, R.M., Payne, A.J., Ng, E.G. and Lipscomb, W.H. (2013). Adaptive mesh, finite volume modeling of marine ice sheets. *Journal of Computational Physics.* 232(1). pp.529-549.

Cornford, S.L., Martin, D.F., Payne, A.J., Ng, E.G., Le Brocq, A.M., Gladstone, R.M., Edwards, T.L., Shannon, S.R., Agosta, C., Van Den Broeke, M.R. and Hellmer, H.H. (2015). Century-scale simulations of the response of the West Antarctic Ice Sheet to a warming climate.

Cuffey, K.M. and Paterson, W.S.B. (2010). *The physics of glaciers*. Academic Press.

De Winter, J.C., (2013). Using the Student's t-test with extremely small sample sizes. *Practical Assessment, Research & Evaluation.* 18(10).

De Rydt, J. and Gudmundsson, G.H. (2016). Coupled ice shelf-ocean modeling and complex grounding line retreat from a seabed ridge. *Journal of Geophysical Research: Earth Surface*. 121(5). pp.865-880.

De Rydt, J., Holland, P.R., Dutrieux, P. and Jenkins, A. (2014). Geometric and oceanographic controls on melting beneath Pine Island Glacier. *Journal of Geophysical Research: Oceans*. 119(4). pp.2420-2438.

De Rydt, J., Gudmundsson, G.H., Rott, H. and Bamber, J.L (2015). Modeling the instantaneous response of glaciers after the collapse of the Larsen B Ice Shelf. *Geophysical Research Letters*. 42(13). pp.5355-5363.

DeConto, R.M. and Pollard, D. (2016). Contribution of Antarctica to past and future sea-level rise. *Nature*. 531(7596). pp.591-597.

Depoorter, M.A., Bamber, J.L., Griggs, J.A., Lenaerts, J.T.M., Ligtenberg, S.R., Van den Broeke, M.R. and Moholdt, G., (2013). Calving fluxes and basal melt rates of Antarctic ice shelves. *Nature.* 502(7469). p.89.

Ding, Q., Steig, E.J., Battisti, D.S. and Küttel, M., (2011). Winter warming in West Antarctica caused by central tropical Pacific warming. *Nature Geoscience*. *4*(6). p.398.

Dinniman, M.S. and Klinck, J.M. (2004). A model study of circulation and cross-shelf exchange on the west Antarctic Peninsula continental shelf. *Deep Sea Research Part II: Topical Studies in Oceanography*. 51(17-19). pp.2003-2022.

Dinniman, M.S., Asay-Davis, X.S., Galton-Fenzi, B.K., Holland, P.R., Jenkins, A. and Timmermann, R. (2016). Modeling ice shelf/ocean interaction in Antarctica: A review. *Oceanography*. *29*(4). pp.144-153.

Dinniman, M.S., Klinck, J.M. and Hofmann, E.E. (2012). Sensitivity of Circumpolar Deep Water transport and ice shelf basal melt along the west Antarctic Peninsula to changes in the winds. *Journal of Climate*. *25*(14). pp.4799-4816.

Donat-Magnin, M., Jourdain, N.C., Spence, P., Le Sommer, J., Gallée, H. and Durand, G. (2017). Ice-Shelf Melt Response to Changing Winds and Glacier Dynamics in the Amundsen Sea Sector, Antarctica. *Journal of Geophysical Research: Oceans*. 122(12). pp.10206-10224.

Downes, S.M. and Hogg, A.M. (2013). Southern Ocean circulation and eddy compensation in CMIP5 models. *Journal of Climate*. 26(18). pp.7198-7220.

Dupont, T.K. and Alley, R.B., (2005). Assessment of the importance of ice-shelf buttressing to ice-sheet flow. Geophysical Research Letters, 32(4).

Dutrieux, P., De Rydt, J., Jenkins, A., Holland, P.R., Ha, H.K., Lee, S.H., Steig, E.J., Ding, Q., Abrahamsen, E.P. and Schröder, M. (2014). Strong sensitivity of Pine Island ice-shelf melting to climatic variability. *Science*. *343*(6167). pp.174-178.

Dutrieux, P., Vaughan, D.G., Corr, H.F., Jenkins, A., Holland, P.R., Joughin, I. and Fleming, A.H., (2013). Pine Island glacier ice shelf melt distributed at kilometre scales. *The Cryosphere*, 7, pp.1543-1555.

Favier, L., Durand, G., Cornford, S.L., Gudmundsson, G.H., Gagliardini, O., Gillet-Chaulet, F., Zwinger, T., Payne, A.J. and Le Brocq, A.M. (2014). Retreat of Pine Island Glacier controlled by marine ice-sheet instability. *Nature Climate Change*, 4(2), p.117.

Flament, T. and Rémy, F. (2012). Dynamic thinning of Antarctic glaciers from along-track repeat radar altimetry. *Journal of Glaciology. 58*(211), pp.830-840.

Flato, G., Marotzke, J., Abiodun, B., Braconnot, P., Chou, S.C., Collins, W., Cox, P., Driouech, F., Emori, S., Eyring, V. and Forest, C. (2013). *Evaluation of climate models*.

Fogt, R.L. and Bromwich, D.H. (2006). Decadal variability of the ENSO teleconnection to the high-latitude South Pacific governed by coupling with the southern annular mode. *Journal of Climate*. *19*(6). pp.979-997.

Foldvik, A. and Kvinge, T., (1974). Conditional instability of sea water at the freezing point. In Deep Sea Research and Oceanographic Abstracts. 21(3). pp. 169-174.

Fretwell, P., Pritchard, H.D., Vaughan, D.G., Bamber, J.L., Barrand, N.E., Bell, R., Bianchi, C., Bingham, R.G., Blankenship, D.D., Casassa, G. and Catania, G. (2013). Bedmap2: improved ice bed, surface and thickness datasets for Antarctica.

Frieler, K., Clark, P.U., He, F., Buizert, C., Reese, R., Ligtenberg, S.R., Van Den Broeke, M.R., Winkelmann, R. and Levermann, A. (2015). Consistent evidence of increasing Antarctic accumulation with warming. Nature Climate Change, 5(4), p.348.

Galton-Fenzi, B.K., (2009). Modelling ice-shelf/ocean interaction (Doctoral dissertation, University of Tasmania).

Gille, S.T. (2002). Warming of the Southern Ocean since the 1950s. *Science*. 295(5558). pp.1275-1277.

Gille, S.T. (2008). Decadal-scale temperature trends in the Southern Hemisphere ocean. *Journal of Climate*, *21*(18), pp.4749-4765.

Gladstone, R.M., Lee, V., Rougier, J., Payne, A.J., Hellmer, H., Le Brocq, A., Shepherd, A., Edwards, T.L., Gregory, J. and Cornford, S.L. (2012). Calibrated prediction of Pine Island Glacier retreat during the 21st and 22nd centuries with a coupled flowline model. *Earth and Planetary Science Letters*. 333. pp.191-199.

Gladstone, R.M., Warner, R.C., Galton-Fenzi, B.K., Gagliardini, O., Zwinger, T. and Greve, R., (2017). Marine ice sheet model performance depends on basal sliding physics and sub-shelf melting. *The Cryosphere*. *11*. pp.319-329.

Gleckler, P.J., Taylor, K.E. and Doutriaux, C. (2008). Performance metrics for climate models. *Journal of Geophysical Research: Atmospheres*. *113*(D6).

Goddard, P.B., Dufour, C.O, Yin, J., Griffies, S.M., Winton, M. (2017). CO2-Induced Ocean Warming of the Antarctic Continental Shelf in an Eddying Global Climate Model. Journal of *Geophysical Research: Oceans*. 122. Pp. 8079-8101.

Goldberg, D., Holland, D.M. and Schoof, C. (2009). Grounding line movement and ice shelf buttressing in marine ice sheets. *Journal of Geophysical Research: Earth Surface*. 114(F4).

Golledge, N.R., Kowalewski, D.E., Naish, T.R., Levy, R.H., Fogwill, C.J. and Gasson, E.G. (2015). The multi-millennial Antarctic commitment to future sea-level rise. *Nature*. *526*(7573), p.421.

Good, S.A., Martin, M.J. and Rayner, N.A., (2013). EN4: Quality controlled ocean temperature and salinity profiles and monthly objective analyses with uncertainty estimates. *Journal of Geophysical Research: Oceans.* 118(12). pp.6704-6716.

Gouretski, V. and Reseghetti, F., (2010). On depth and temperature biases in bathythermograph data: Development of a new correction scheme based on analysis of a global ocean database. *Deep Sea Research Part I: Oceanographic Research Papers*. *57*(6). pp.812-833.

Gudmundsson, G.H., (2013). Ice-shelf buttressing and the stability of marine ice sheets. *The Cryosphere.* 7(2). p.647.

Hanna, E., Navarro, F.J., Pattyn, F., Domingues, C.M., Fettweis, X., Ivins, E.R., Nicholls, R.J., Ritz, C., Smith, B., Tulaczyk, S. and Whitehouse, P.L. (2013). Ice-sheet mass balance and climate change. Nature, 498(7452), p.51.

Harig, C. and Simons, F.J. (2015). Accelerated West Antarctic ice mass loss continues to outpace East Antarctic gains. *Earth and Planetary Science Letters*. 415.

Hellmer, H.H., Kauker, F., Timmermann, R. and Hattermann, T. (2017). The fate of the southern Weddell Sea continental shelf in a warming climate. *Journal of Climate*. 30(12). pp.4337-4350.

Hellmer, H.H., Kauker, F., Timmermann, R., Determann, J. and Rae, J. (2012). Twenty-first-century warming of a large Antarctic ice-shelf cavity by a redirected coastal current. *Nature*. *485*(7397), p.225.

Hellmer, H.H., Kauker, F., Timmermann, R., Determann, J. and Rae, J. (2012). Twenty-first-century warming of a large Antarctic ice-shelf cavity by a redirected coastal current. *Nature.* 485(7397). pp.225-228.

Heuzé, C., Heywood, K.J., Stevens, D.P. and Ridley, J.K. (2013). Southern Ocean bottom water characteristics in CMIP5 models. *Geophysical Research Letters*, *40*(7), pp.1409-1414.

Holland, P.R., Jenkins, A. and Holland, D.M. (2008). The response of ice shelf basal melting to variations in ocean temperature. *Journal of Climate*. 21(11). pp.2558-2572.

Holt, J.W., Blankenship, D.D., Morse, D.L., Young, D.A., Peters, M.E., Kempf, S.D., Richter, T.G., Vaughan, D.G. and Corr, H.F. (2006). New boundary conditions for the West Antarctic Ice Sheet: Subglacial topography of the Thwaites and Smith glacier catchments. *Geophysical Research Letters*. 33(9).

Hosking, J.S., Orr, A., Marshall, G.J., Turner, J. and Phillips, T. (2013). The influence of the Amundsen–Bellingshausen Seas low on the climate of West Antarctica and its representation in coupled climate model simulations. *Journal of Climate*. 26(17). pp.6633-6648.

Hughes, T.J. (1981). The weak underbelly of the West Antarctic ice sheet. *Journal of Glaciology*. 27(97). pp.518-525.

Jacobs, S. (2006). Observations of change in the Southern Ocean. *Philosophical Transactions of the Royal Society of London A: Mathematical, Physical and Engineering Sciences*. *364*(1844). pp.1657-1681.

Jacobs, S.S., Jenkins, A., Giulivi, C.F. and Dutrieux, P. (2011). Stronger ocean circulation and increased melting under Pine Island Glacier ice shelf. *Nature Geoscience*. 4(8). pp.519-523.

Jenkins, A. (2011). Convection-driven melting near the grounding lines of ice shelves and tidewater glaciers. *Journal of Physical Oceanography*. *41*(12). pp.2279-2294.

Jenkins, A., Dutrieuz, P., Jacobs, S., Steig, E.J., Gudmundsson, G.H., Smith, J. and Heywood, K.J. (2016). Decadal Ocean Forcing and Antarctic Ice Sheet Response: Lessons from the Amundsen Sea*. Oceanography.* 29(4).

Jenkins, A., Nicholls, K.W. and Corr, H.J.F. (2010). Observation and Parameterisation of Ablation at the Base of Ronne Ice Shelf, Antarctica. *Journal of Physical Oceanography.* 40.

Jevrejeva, S., Grinsted, A. and Moore, J.C. (2014). Upper limit for sea level projections by 2100. *Environmental research letters*. 9(10). P.104008.

Joughin, I., Smith, B.E. and Holland, D.M. (2010). Sensitivity of 21st century sea level to ocean-induced thinning of Pine Island Glacier, Antarctica. *Geophysical Research Letters. 37*(20).

Joughin, I., Smith, B.E. and Medley, B., 2014. Marine ice sheet collapse potentially under way for the Thwaites Glacier Basin, West Antarctica. *Science*, 344(6185), pp.735-738.

Joughin, I., Tulaczyk, S., Bamber, J.L., Blankenship, D., Holt, J.W., Scambos, T. and Vaughan, D.G., (2009). Basal conditions for Pine Island and Thwaites Glaciers, West Antarctica, determined using satellite and airborne data. *Journal of Glaciology*. *55*(190). pp.245-257.

Katz, R.F. and Worster, M.G. (2010). Stability of ice-sheet grounding lines. In Proceedings of the Royal Society of London A: Mathematical, Physical and Engineering Sciences. 466(2118). pp. 369-373.

Knutti, R. and Sedláček, J. (2013). Robustness and uncertainties in the new CMIP5 climate model projections. *Nature Climate Change*. 3(4). pp.369-373.

Konrad, H., Gilbert, L., Cornford, S.L., Payne, A., Hogg, A., Muir, A. and Shepherd, A. (2017). Uneven onset and pace of ice-dynamical imbalance in the Amundsen Sea Embayment, West Antarctica. *Geophysical Research Letters*. 44(2). pp.910-918.

Lazeroms, W.M., Jenkins, A., Gudmundsson, G.H. and Van De Wal, R.S. (2018). Modelling present-day basal melt rates for Antarctic ice shelves using a parametrization of buoyant meltwater plumes. *The Cryosphere*. 12(1). pp.49-70.

Levermann, A., Winkelmann, R., Nowicki, S., Fastook, J.L., Frieler, K., Greve, R., Hellmer, H.H., Martin, M.A., Meinshausen, M., Mengel, M. and Payne, A.J. (2014). Projecting Antarctic ice

discharge using response functions from SeaRISE ice-sheet models. *Earth System Dynamics*. *5*. pp.271-293.

Little, C.M. and Urban, N.M. (2016). CMIP5 temperature biases and 21st century warming around the Antarctic coast. *Annals of Glaciology*. 57(73), pp.69-78.

Little, C.M., Horton, R.M., Kopp, R.E., Oppenheimer, M. and Yip, S. (2015). Uncertainty in twenty-first-century CMIP5 sea level projections. *Journal of Climate*, *28*(2), pp.838-852.

Little, C.M., Oppenheimer, M. and Urban, N.M. (2013). Upper bounds on twenty-first-century Antarctic ice loss assessed using a probabilistic framework. *Nature Climate Change*. *3*(7). p.654.

Liu, J. and Curry, J.A. (2010). Accelerated warming of the Southern Ocean and its impacts on the hydrological cycle and sea ice. *Proceedings of the National Academy of Sciences*. *107*(34). pp.14987-14992.

MacAyeal, D.R., (1984). Thermohaline circulation below the Ross Ice Shelf: A consequence of tidally induced vertical mixing and basal melting. *Journal of Geophysical Research: Oceans.* 89(C1). pp.597-606.

MacGregor, J.A., Catania, G.A., Conway, H., Schroeder, D.M., Joughin, I., Young, D.A., Kempf, S.D. and Blankenship, D.D. (2013). Weak bed control of the eastern shear margin of Thwaites Glacier, West Antarctica. *Journal of Glaciology*. *59*(217). pp.900-912.

MacGregor, J.A., Catania, G.A., Markowski, M.S. and Andrews, A.G., (2012). Widespread rifting and retreat of ice-shelf margins in the eastern Amundsen Sea Embayment between 1972 and 2011. *Journal of Glaciology*. 58(209). pp.458-466.

Mallett, H.K., Boehme, L., Fedak, M.A., Heywood, K.J., Stevens, D.P. and Roquet, F. (2018). Variation in the distribution and properties of Circumpolar Deep Water in the eastern Amundsen Sea, on seasonal timescales, using seal-borne tags. *Geophysical Research Letters*.

Marshall, G.J., (2003). Trends in the Southern Annular Mode from observations and reanalyses. *Journal of Climate*. *16*(24). pp.4134-4143.

Martin, M.A., Winkelmann, R., Haseloff, M., Albrecht, T., Bueler, E., Khroulev, C. and Levermann, A., (2011). The Potsdam Parallel Ice Sheet Model (PISM-PIK)–Part 2: Dynamic equilibrium simulation of the Antarctic ice sheet. *The Cryosphere*. 5(3). pp.727-740.

Martinson, D.G. and McKee, D.C. (2012). Transport of warm Upper Circumpolar Deep Water onto the western Antarctic Peninsula continental shelf. *Ocean Science*. 8(4).

Mcmillan, M., Shepherd, A., Sundal, A., Briggs, K., Muir, A., Ridout, A., Hogg, A. and Wingham, D. (2014). Increased ice losses from Antarctica detected by CryoSat-2. *Geophysical Research Letters*. 41(11). pp.3899-3905.

Meehl, G.A., Covey, C., Taylor, K.E., Delworth, T., Stouffer, R.J., Latif, M., McAvaney, B. and Mitchell, J.F. (2007). The WCRP CMIP3 multi-model dataset: A new era in climate change research. *Bulletin of the American Meteorological Society*. 88(9). pp.1383-1394.

Meehl, G. A., et al., (2007b): Global climate projections. In: Climate Change 2007: The Physical Science Basis. Contribution of Working Group I to the Fourth Assessment Report of the Intergovernmental Panel on Climate Change [Solomon, S., D. Qin, M. Manning, Z. Chen, M. Marquis, K. B. Averyt, M. Tignor and H. L. Miller (eds.)] Cambridge University Press, Cambridge, United Kingdom and New York, NY, USA, pp. 747–846

Meehl, G.A., Washington, W.M., Arblaster, J.M., Hu, A., Teng, H., Tebaldi, C., Sanderson, B.N., Lamarque, J.F., Conley, A., Strand, W.G. and White III, J.B. (2012). Climate system response to external forcings and climate change projections in CCSM4. *Journal of Climate*. 25(11). pp.3661-3683.

Meijers, A.J., Shuckburgh, E., Bruneau, N., Sallée, J.B., Bracegirdle, T.J. and Wang, Z. (2012). Representation of the Antarctic Circumpolar Current in the CMIP5 climate models and future changes under warming scenarios. *Journal of Geophysical Research: Oceans, 117*(C12).

Meijers, A.J.S. (2014). The Southern Ocean in the coupled model intercomparison project phase 5. *Philosophical Transcripts Research Society. A*, *372*(2019), p.20130296.

Mengel, M., Levermann, A., Frieler, K., Robinson, A., Marzeion, B. and Winkelmann, R. (2016). Future sea level rise constrained by observations and long-term commitment. *Proceedings of the National Academy of Sciences*, p.201500515.

Miller, R.L., Schmidt, G.A. and Shindell, D.T. (2006). Forced annular variations in the 20th century intergovernmental panel on climate change fourth assessment report models. *Journal of Geophysical Research: Atmospheres*, *111*(D18).

Mouginot, J., Rignot, E. and Scheuchl, B. (2014). Sustained increase in ice discharge from the Amundsen Sea Embayment, West Antarctica, from 1973 to 2013. *Geophysical Research Letters.* 41(5). pp.1576-1584.

Nakayama, Y., Timmermann, R., Rodehacke, C.B., Schröder, M. and Hellmer, H.H. (2014). Modeling the spreading of glacial meltwater from the Amundsen and Bellingshausen Seas. *Geophysical Research Letters*. *41*(22). pp.7942-7949.

Nakayama, Y., Menemenlis, D., Schodlok, M. and Rignot, E. (2017). Amundsen and Bellingshausen Seas simulation with optimized ocean, sea ice, and thermodynamic ice shelf model parameters. *Journal of Geophysical Research: Oceans*. 122(8). pp.6180-6195.

Naughten, K.A., Meissner, K.J., Galton-Fenzi, B.K., England, M.H., Timmermann, R. and Hellmer, H.H. (2018). Future Projections of Antarctic Ice Shelf Melting Based on CMIP5 Scenarios. *Journal of Climate*. *31*(13). pp.5243-5261.

Nias, I.J., Cornford, S.L. and Payne, A.J. (2016). Contrasting the modelled sensitivity of the Amundsen Sea Embayment ice streams. *Journal of Glaciology*. 62(233), pp.552-562.

Nias, I.J. (2017). Modelling the Amundsen Sea ice streams, West Antarctica. PhD. University of Bristol.

Nitsche, F.O., Jacobs, S.S., Larter, R.D. and Gohl, K. (2007). Bathymetry of the Amundsen Sea continental shelf: implications for geology, oceanography, and glaciology. *Geochemistry, Geophysics, Geosystems*. 8(10).

Nitsche, F.O., Gohl, K., Larter, R.D., Hillenbrand, C.D., Kuhn, G., Smith, J.A., Jacobs, S., Anderson, J.B. and Jakobsson, M. (2013). Paleo ice flow and subglacial meltwater dynamics in Pine Island Bay, West Antarctica. *The Cryosphere*. 7(1). pp.249-262.

Nowicki, S.M.J., Payne, A., Larour, E., Seroussi, H., Goelzer, H., Lipscomb, W., Gregory, J., Abe-Ouchi, A., Shepard, A. (2016). Ice Sheet Model Intercomparison Project (ISMIP6) contribution to CMIP6. *Geoscience Model Development*. 9. pp. 4521-4545.

Orsi, A.H., Whitworth III, T. and Nowlin Jr, W.D., 1995. On the meridional extent and fronts of the Antarctic Circumpolar Current. *Deep Sea Research Part I: Oceanographic Research Papers*. 42(5). pp.641-673.

Parizek, B.R. and Walker, R.T. (2010). Implications of initial conditions and ice–ocean coupling for grounding-line evolution. *Earth and Planetary Science Letters*. 300(3-4). pp.351-358.

Parizek, B.R., Christianson, K., Anandakrishnan, S., Alley, R.B., Walker, R.T., Edwards, R.A., Wolfe, D.S., Bertini, G.T., Rinehart, S.K., Bindschadler, R.A. and Nowicki, S.M.J. (2013). Dynamic (in) stability of Thwaites Glacier, West Antarctica. *Journal of Geophysical Research: Earth Surface*. 118(2). pp.638-655.

Park, J.W., Gourmelen, N., Shepherd, A., Kim, S.W., Vaughan, D.G. and Wingham, D.J. (2013). Sustained retreat of the Pine Island Glacier. *Geophysical Research Letters.* 40(10), pp.2137-2142.

Pattyn, F. (2010). Antarctic subglacial conditions inferred from a hybrid ice sheet/ice stream model. *Earth and Planetary Science Letters*. *295*(3-4). pp.451-461.

Pattyn, F., Perichon, L., Durand, G., Favier, L., Gagliardini, O., Hindmarsh, R.C., Zwinger, T., Albrecht, T., Cornford, S., Docquier, D. and Fürst, J.J. (2013). Grounding-line migration in plan-view marine ice-sheet models: results of the ice2sea MISMIP3d intercomparison. *Journal of Glaciology*, *59*(215). pp.410-422.

Payne, A.J., Holland, P.R., Shepherd, A.P., Rutt, I.C., Jenkins, A. and Joughin, I. (2007). Numerical modeling of ocean-ice interactions under Pine Island Bay's ice shelf. *Journal of Geophysical Research: Oceans*. 112(C10).

Payne, A.J., Vieli, A., Shepherd, A.P., Wingham, D.J. and Rignot, E. (2004). Recent dramatic thinning of largest West Antarctic ice stream triggered by oceans. *Geophysical Research Letters*. 31(23).

Petty, A.A., Feltham, D.L. and Holland, P.R. (2013). Impact of atmospheric forcing on Antarctic continental shelf water masses. *Journal of Physical Oceanography.* 43(5). pp.920-940.

Petty, A.A., Holland, P.R. and Deltham, D.L. (2014), Sea ice and the ocean mixed layer over the Antarctic shelf areas. *The Cryosphere.* 8. 761-783.

Pollard, D. and DeConto, R.M. (2012). Description of a hybrid ice sheet-shelf model, and application to Antarctica. *Geoscientific Model Development. 5*(5). p.1273.

Polvani, L.M. and Smith, K.L. (2013). Can natural variability explain observed Antarctic sea ice trends? New modeling evidence from CMIP5. *Geophysical Research Letters*. 40(12). pp.3195-3199.

Pritchard, H.D., Arthern, R.J., Vaughan, D.G. and Edwards, L.A. (2009). Extensive dynamic thinning on the margins of the Greenland and Antarctic ice sheets. *Nature*. 461(7266), p.971.

Pritchard, H.D., Ligtenberg, S.R.M., Fricker, H.A., Vaughan, D.G., van den Broeke, M.R. and Padman, L. (2012). Antarctic ice sheet loss driven by basal melting of ice shelves. *Nature.* 484. Pp. 502-505.

Rignot, E. (2008). Changes in West Antarctic ice stream dynamics observed with ALOS PALSAR data. *Geophysical Research Letters*. 35(12).

Rignot, E. and Jacobs, S.S. (2002). Rapid bottom melting widespread near Antarctic ice sheet grounding lines. *Science.* 296(5575). pp.2020-2023.

Rignot, E., Bamber, J.L., Van Den Broeke, M.R., Davis, C., Li, Y., Van De Berg, W.J. and Van Meijgaard, E. (2008). Recent Antarctic ice mass loss from radar interferometry and regional climate modelling. *Nature geoscience*. 1(2). p.106.

Rignot, E., Jacobs, S., Mouginot, J. and Scheuchl, B. (2013). Ice-shelf melting around Antarctica. *Science*. 341(6143). pp.266-270.

Rignot, E., Casassa, G., Gogineni, P., Krabill, W., Rivera, A.U. and Thomas, R. (2004). Accelerated ice discharge from the Antarctic Peninsula following the collapse of Larsen B ice shelf. *Geophysical Research Letters*. 31(18).

Rignot, E., Mouginot, J. and Scheuchl, B. (2011). Ice flow of the Antarctic ice sheet. *Science*. 333(6048). pp.1427-1430.

Rignot, E., Mouginot, J., Morlighem, M., Seroussi, H. and Scheuchl, B. (2014). Widespread, rapid grounding line retreat of Pine Island, Thwaites, Smith, and Kohler glaciers, West Antarctica, from 1992 to 2011. *Geophysical Research Letters.* 41(10), pp.3502-3509.

Rignot, E., Velicogna, I., van den Broeke, M.R., Monaghan, A. and Lenaerts, J.T.M. (2011). Acceleration of the contribution of the Greenland and Antarctic ice sheets to sea level rise. *Geophysical Research Letters*. 38. L05503.

Rintoul, S.R. and Trull, T.W. (2001). Seasonal evolution of the mixed layer in the Subantarctic Zone south of Australia. *Journal of Geophysical Research: Oceans.* 106(C12). pp.31447-31462.

Ritz, C., Durand, G., Edwards, T., Hellmer, H., Payne, T., Shannon, S. and Timmermann, R. (2012). Antarctic instability and possible associated contribution to sea-level rise. *In EGU General Assembly Conference Abstracts.* 14. pp. 12900.

Ritz, C., Edwards, T.L., Durand, G., Payne, A.J., Peyaud, V. and Hindmarsh, R.C., (2015). Potential sea-level rise from Antarctic ice-sheet instability constrained by observations. *Nature*. 528(7580), p.115.

Rodriguez, A.R., Mazloff, M.R. and Gille, S.T. (2016). An oceanic heat transport pathway to the Amundsen Sea Embayment. *Journal of Geophysical Research: Oceans*. *121*(5). pp.3337-3349.

Sallée, J.B., Shuckburgh, E., Bruneau, N., Meijers, A.J., Bracegirdle, T.J. and Wang, Z. (2013). Assessment of Southern Ocean mixed-layer depths in CMIP5 models: Historical bias and forcing response. *Journal of Geophysical Research: Oceans*. 118(4). pp.1845-1862.

Scheuchl, B., Mouginot, J., Rignot, E., Morlighem, M. and Khazendar, A. (2016). Grounding line retreat of Pope, Smith, and Kohler Glaciers, West Antarctica, measured with Sentinel-1a radar interferometry data. *Geophysical Research Letters.* 43(16). pp.8572-8579.

Schmidtko, S., Heywood, K.J., Tompson, A.F. and Aoki, S. (2014). Multidecadal warming of Antarctic waters. *Oceanography*. 346(6214). Pp. 1227-1230.

Schneider, D.P. and Reusch, D.B. (2016). Antarctic and Southern Ocean surface temperatures in CMIP5 models in the context of the surface energy budget. *Journal of Climate*. 29(5), pp.1689-1716.

Schoof, C. (2007). Ice sheet grounding line dynamics: Steady states, stability, and hysteresis. *Journal of Geophysical Research: Earth Surface*. 112(F3).

Schoof, C. (2010). Ice-sheet acceleration driven by melt supply variability. *Nature*. 468(7325). p.803.

Schoof, C. and Hindmarsh, R.C. (2010). Thin-film flows with wall slip: an asymptotic analysis of higher order glacier flow models. *Quarterly journal of mechanics and applied mathematics*. 63(1). pp.73-114.

Seroussi, H., Morlighem, M., Rignot, E., Mouginot, J., Larour, E., Schodlok, M. and Khazendar, A., (2014). Sensitivity of the dynamics of Pine Island Glacier, West Antarctica, to climate forcing for the next 50 years.

Shepherd, A., Ivins, E., Rignot, E., Smith, B., van den Broeke, M., Velicogna, I., Whitehouse, P., Briggs, K., Joughin, I., Krinner, G. and Nowicki, S. (2018). Mass balance of the Antarctic Ice Sheet from 1992 to 2017. *Nature*. *556*. pp.pages219-222.

Shepherd, A., Ivins, E.R., Geruo, A., Barletta, V.R., Bentley, M.J., Bettadpur, S., Briggs, K.H., Bromwich, D.H., Forsberg, R., Galin, N. and Horwath, M. (2012). A reconciled estimate of ice-sheet mass balance. *Science*. *338*(6111). pp.1183-1189.

Shepherd, A., Wingham, D. and Rignot, E. (2004). Warm ocean is eroding West Antarctic ice sheet. *Geophysical Research Letters*. 31(23).

Shu, Q., Song, Z. and Qiao, F., (2014). Assessment of sea ice simulations in the CMIP5 Models. *The Cryosphere Discussions*. 8. pp.3413-3435.

Smith, J.A., Andersen, T.J., Shortt, M., Gaffney, A.M., Truffer, M., Stanton, T.P., Bindschadler, R., Dutrieux, P., Jenkins, A., Hillenbrand, C.D. and Ehrmann, W. (2017). Sub-ice-shelf sediments record history of twentieth-century retreat of Pine Island Glacier. *Nature.* 541(7635), pp.77-80.

Spence, P., Griffies, S.M., England, M.H., Hogg, A.M., Saenko, O.A. and Jourdain, N.C., 2014. Rapid subsurface warming and circulation changes of Antarctic coastal waters by poleward shifting winds. *Geophysical Research Letters*, *41*(13), pp.4601-4610.

Steig, E.J., Ding, Q., Battisti, D.S. and Jenkins, A., 2012. Tropical forcing of Circumpolar Deep Water inflow and outlet glacier thinning in the Amundsen Sea Embayment, West Antarctica. Annals of Glaciology. 53(60). pp.19-28.

Steig, E.J., Schneider, D.P., Rutherford, S.D., Mann, M.E., Comiso, J.C. and Shindell, D.T. (2009). Warming of the Antarctic ice-sheet surface since the 1957 International Geophysical Year. *Nature.* 457(7228), p.459.

St-Laurent, P., Klinck, J.M. and Dinniman, M.S., 2013. On the role of coastal troughs in the circulation of warm Circumpolar Deep Water on Antarctic shelves. Journal of Physical Oceanography, 43(1), pp.51-64.

Sun, S., S. L. Cornford, Y. Liu, and J. C. Moore (2014). Dynamic response of Antarctic ice shelves to bedrock uncertainty. *The Cryosphere.* 8(4). pp. 1561–1576.

Swingedouw, D., T. Fichefet, P. Huybrechts, H. Goosse, E. Driesschaert, and M. Loutre, (2008). Antarctic ice-sheet melting provides negative feedbacks on future climate warming. *Geophysical Research Letters*. 35. L17705.

Talley, L.D. (2011). Descriptive physical oceanography: an introduction. Academic press

Taylor, K.E., Stouffer, R.J. and Meehl, G.A., (2012). An overview of CMIP5 and the experiment design. Bulletin of the American Meteorological Society, 93(4), pp.485-498.

Thoma, M., Jenkins, A., Holland, D. and Jacobs, S. (2008). Modelling circumpolar deep water intrusions on the Amundsen Sea continental shelf, Antarctica. *Geophysical Research Letters*. 35(18).

Timmermann, R. and Hellmer, H.H. (2013). Southern Ocean warming and increased ice shelf basal melting in the twenty-first and twenty-second centuries based on coupled ice-ocean finite-element modelling. *Ocean Dynamics*. *63*(9-10). pp.1011-1026.

Timmermann, R., Wang, Q. and Hellmer, H.H. (2012). Ice-shelf basal melting in a global finite-element sea-ice/ice-shelf/ocean model. *Annals of Glaciology*. *53*(60). pp.303-314.

Tinto, K.J. and Bell, R.E. (2011). Progressive unpinning of Thwaites Glacier from newly identified offshore ridge: Constraints from aerogravity. *Geophysical Research Letters*. 38(20).

Trusel, L.D., Frey, K.E., Das, S.B., Karnauskas, K.B., Munneke, P.K., Van Meijgaard, E. and Van Den Broeke, M.R. (2015). Divergent trajectories of Antarctic surface melt under two twenty-first-century climate scenarios. Nature Geoscience. 8(12). p.927.

Turner, J. (2004). The El Niño–Southern Oscillation and Antarctica. *International Journal of Climatology: A Journal of the Royal Meteorological Society*, *24*(1), pp.1-31.

Turner, J., Bracegirdle, T.J., Phillips, T., Marshall, G.J. and Hosking, J.S. (2013). An initial assessment of Antarctic sea ice extent in the CMIP5 models. *Journal of Climate.* 26(5), pp.1473-1484.

Turner, J., Orr, A., Gudmundsson, G.H., Jenkins, A., Bingham, R.G., Hillenbrand, C.D. and Bracegirdle, T.J. (2017). Atmosphere-ocean-ice interactions in the Amundsen Sea Embayment, West Antarctica. *Reviews of Geophysics*, 55(1), pp.235-276.

Vaughan, D.G. (2008). West Antarctic Ice Sheet collapse–the fall and rise of a paradigm. *Climatic Change,* 91(1-2), pp.65-79.

Vaughan, D. G., H. F. J. Corr, F. Ferraccioli, N. Frearson, A. O'Hare, D. Mach, J. W. Holt, D. D. Blankenship, D. L. Morse, and D. A. Young (2006). New boundary conditions for the West Antarctic ice sheet: Subglacial topography beneath Pine Island Glacier. Geophysical Research Letters (33)

Vieli, A. and Payne, A.J. (2005). Assessing the ability of numerical ice sheet models to simulate grounding line migration. *Journal of Geophysical Research: Earth Surface*. 110(F1).

Wåhlin, A.K., Kalén, O., Arneborg, L., Björk, G., Carvajal, G.K., Ha, H.K., Kim, T., Lee, S.H., Lee, J. and Stranne, C. (2013). Variability of warm deep water inflow in a submarine trough on the Amundsen Sea shelf. *Journal of Physical Oceanography*. *43*(10). pp.2054-2070.

Wåhlin, A.K., Yuan, X., Björk, G. and Nohr, C. (2010). Inflow of warm Circumpolar Deep Water in the central Amundsen shelf. *Journal of Physical Oceanography*. 40(6), pp.1427-1434.

Walker, D.P., Brandon, M.A., Jenkins, A., Allen, J.T., Dowdeswell, J.A. and Evans, J. (2007). Oceanic heat transport onto the Amundsen Sea shelf through a submarine glacial trough. *Geophysical Research Letters*. 34(2).

Walker, D.P., Jenkins, A., Assmann, K.M., Shoosmith, D.R. and Brandon, M.A. (2013). Oceanographic observations at the shelf break of the Amundsen Sea, Antarctica. *Journal of Geophysical Research: Oceans*. 118(6). pp.2906-2918.

Webber, B.G., Heywood, K.J., Stevens, D.P., Dutrieux, P., Abrahamsen, E.P., Jenkins, A., Jacobs, S.S., Ha, H.K., Lee, S.H. and Kim, T.W. (2017). Mechanisms driving variability in the ocean forcing of Pine Island Glacier. *Nature communications*. 8. p.14507.

Weertman, J. (1974). Stability of the junction of an ice sheet and an ice shelf. *Journal of Glaciology*. 13(67). pp.3-11.

Weigel, A.P., Knutti, R., Liniger, M.A. and Appenzeller, C. (2010). Risks of model weighting in multimodel climate projections. *Journal of Climate*. *23*(15). pp.4175-4191.

Whitworth, T. and Nowlin, W.D. (1987). Water masses and currents of the Southern Ocean at the Greenwich Meridian. *Journal of Geophysical Research: Oceans*. *92*(C6). pp.6462-6476.

Wingham, D.J., Wallis, D.W. and Shepherd, A. (2009). Spatial and temporal evolution of Pine Island Glacier thinning, 1995–2006. *Geophysical Research Letters*. 36(17).

Yin, J., Overpeck, J.T., Griffies, S.M., Hu, A., Russell, J.L. and Stouffer, R.J. (2011). Different magnitudes of projected subsurface ocean warming around Greenland and Antarctica. *Nature Geoscience*. *4*(8). p.524.

Appendix

As this investigation is interested in simulations of ocean temperature over the 400-700m layer, RMSE metrics were calculated for each model compared with observations at this depth (fig 3.5). The range of RMSE scores are consistent with those calculated for all depths, with the minimum mean RMSE being 1.66°C and the maximum being 2.30°C. For the models with the highest RMSEs, those calculated over the 400-700 m layer have a greater magnitude than those calculated over all depths.

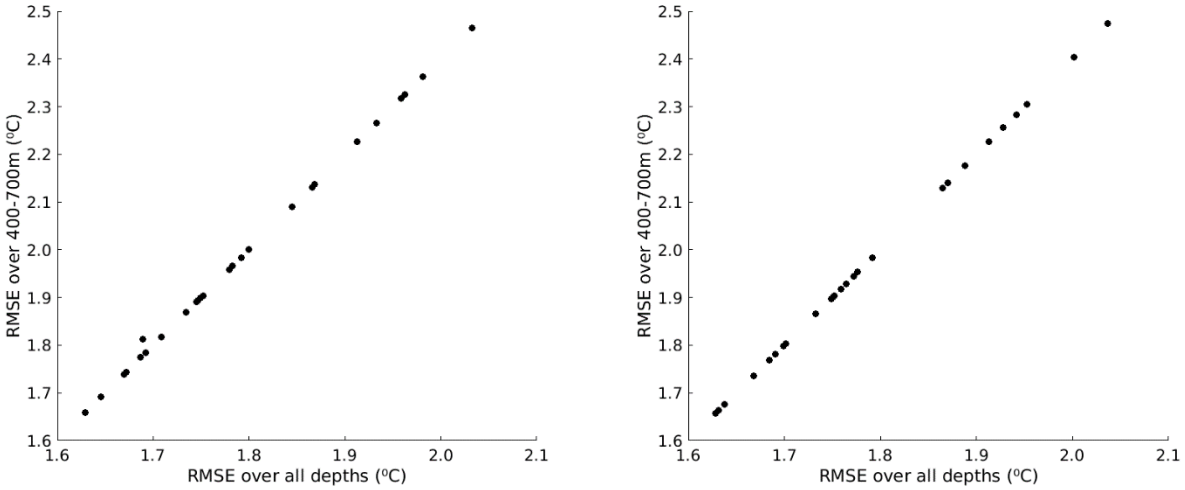

1A: *Correlation between CMIP5 modelled ocean temperature RMSE calculated over the 400-700m layer compared with RMSE calculated over all depths in the Southern Ocean from 1979-2016.*

Considering the observations exclusively to indicate the temperature trend observed on shelf (averaged over the 400-700 m layer) over the 37-year period demonstrates a negative trend of -0.0008°C per month which equates to -0.1°C per decade. However, this trend has a p-value of 0.28, indicating that the trend is not statistically significantly different from 0.

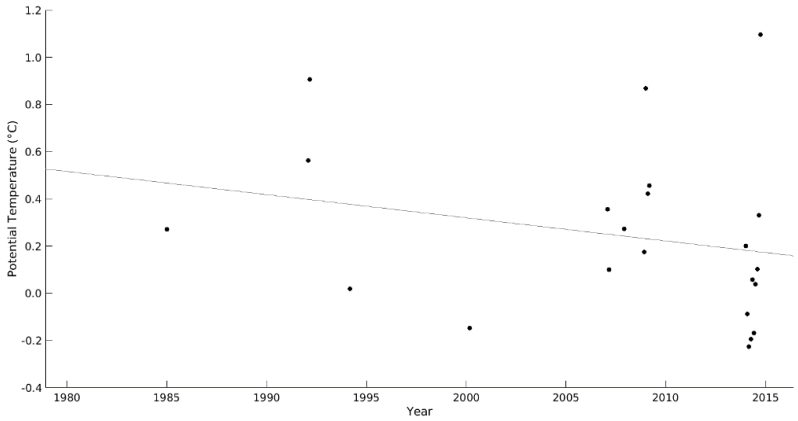

2A: *Ocean temperature observations on shelf in the ASE (400-700 m depth) with line of best fit.*

3A: *Southern Ocean temperature MBE for each model in the subset, in addition to GISS-E2-R, calculated using observations from 1979 to 2016.*

Model	**MBE (°C)**
bcc-csm1-1	-0.05
CanESM2	-0.37
CCSM4	0.96
CESM1-CAM5	1.57
GISS-E2-R	-0.77
MRI-CGCM3	2.04
NorESM1-ME	0.83

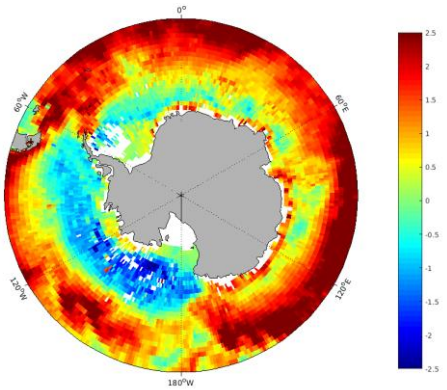

4A: *Ocean potential temperature MBE over the observational period (1979-2016) as projected by the GISS-E2-R model. The last decade of the observational period uses RCP8.5 projections.*

GISS-E2-R RMSE is 2.32 with RCP2.6 and 2.28 with RCP8.5. GISS-E2-R MBE is 1.09 with RCP2.6 and 1.03 with RCP8.5. Indicating that generally the model is warm biased over the Southern Ocean, this is supported by the map illustrated (fig. 8.3).

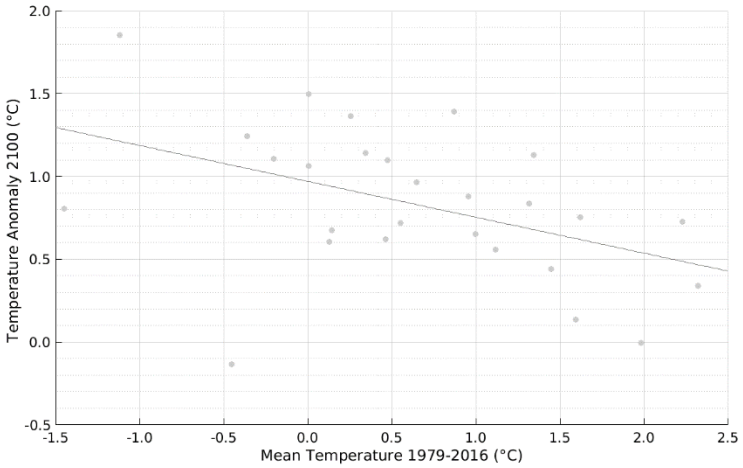

5A: *Correlation between the mean modelled temperature on shelf in the ASE and the equivalent temperature anomaly for each model projection in 2100 relative to present day (2006-2016 mean).*

Relationship between projected temperature change and temperature on shelf over the observational period has a negative, significant ($p = 0.019$) relationship. For every 1°C increase in observed temperature, there is a decrease in temperature change of -0.22°C. Models with higher means generally have lower projected temperature change. However the R2 is 0.2 indicating that there is a fair amount of variability.

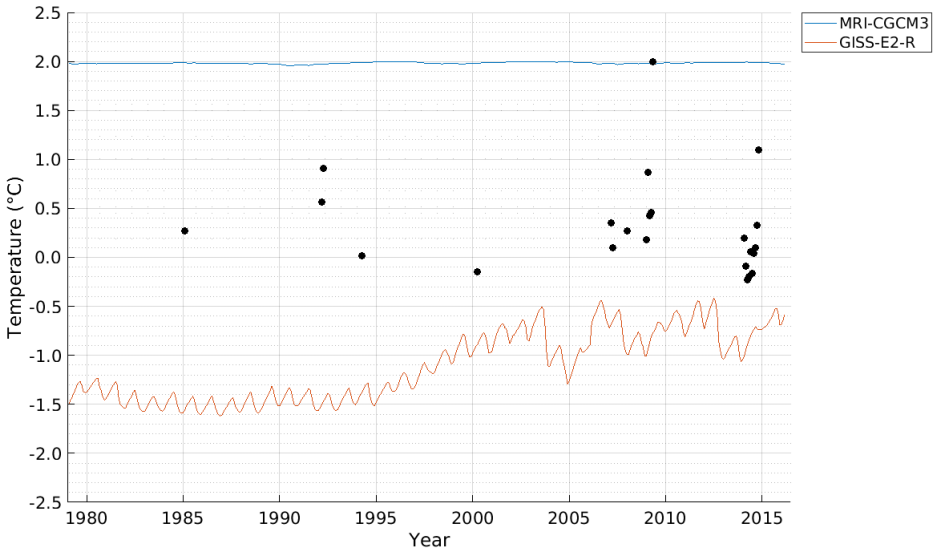

6A: *Modelled ocean temperature averaged over the 400-700 m layer in the ASE over the observational period (1979-2016) for models MRI-CGCM3 and GISS-E2-R. Black scatter indicates the observed ocean temperature from the EN4 Hadley Centre dataset over the same layer in the ASE.*

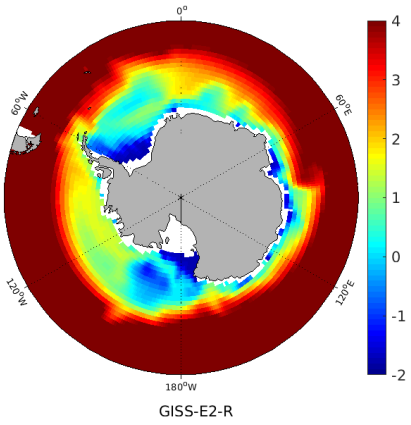

7A: *Projected 2100 (2091-2100 mean) temperature in the Southern Ocean over the 400-700 m forced with the GISS-E2-R model under the RCP8.5 forcing scenario.*

8A: *Location of the PIG transect.*

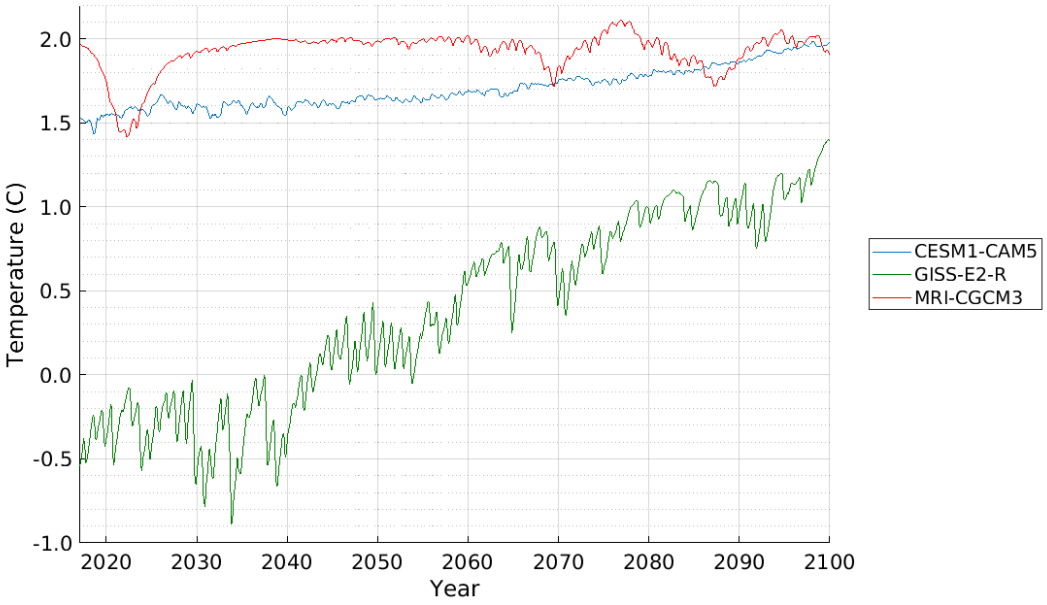

9A: *Projected ocean temperature averaged over the ASE 400-700 m layer over the 21st century. Projections for models CESM1-CAM5, GISS-E2-R and MRI-CGCM3 forced with RCP8.5.*

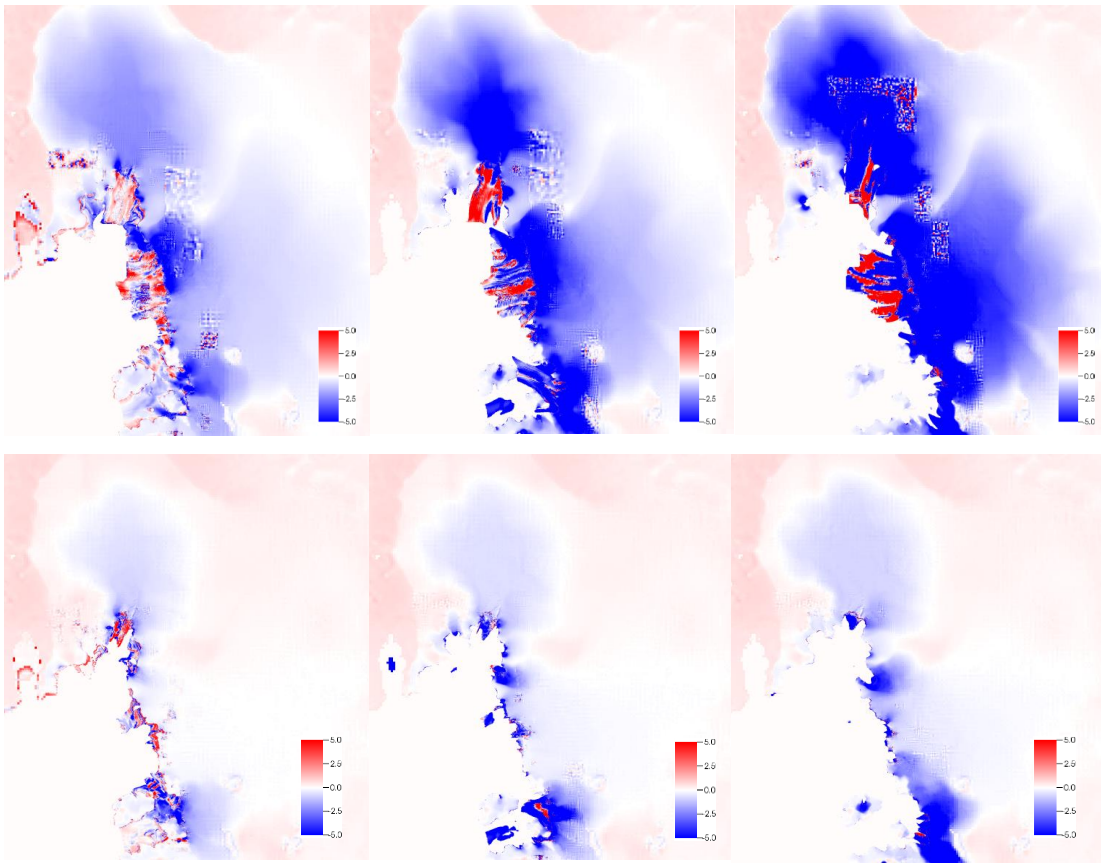

10A: *Rate of change of thickness in 2100 for MRI-CGCM3 (left), CESM1-CAM5 (middle) and GISS-E2-R (right) for the H parameter set (top) and L parameter set (bottom).*

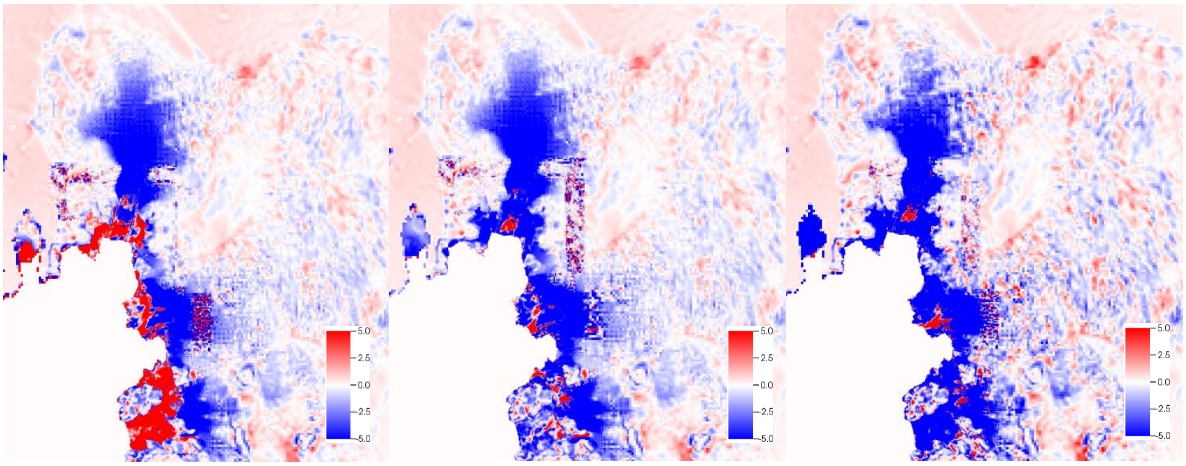

11A: *Rate of change of thickness in 2020 for MRI-CGCM3 (left), CESM1-CAM5 (middle) and GISS-E2-R (right) using the H parameter set.*

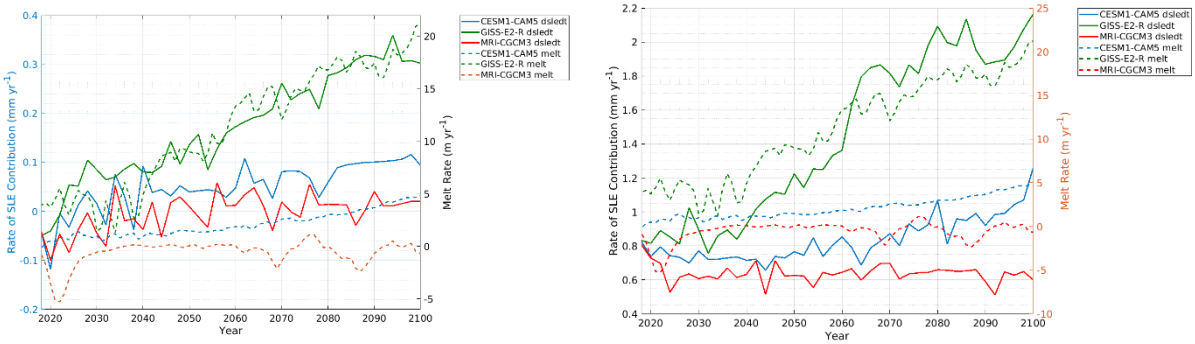

12A: *Projected melt rate forcing and resulting rate of SLE contribution from the ASE over the period from 2017 to 2100 for the L parameter set (left) and the H parameter set (right).*

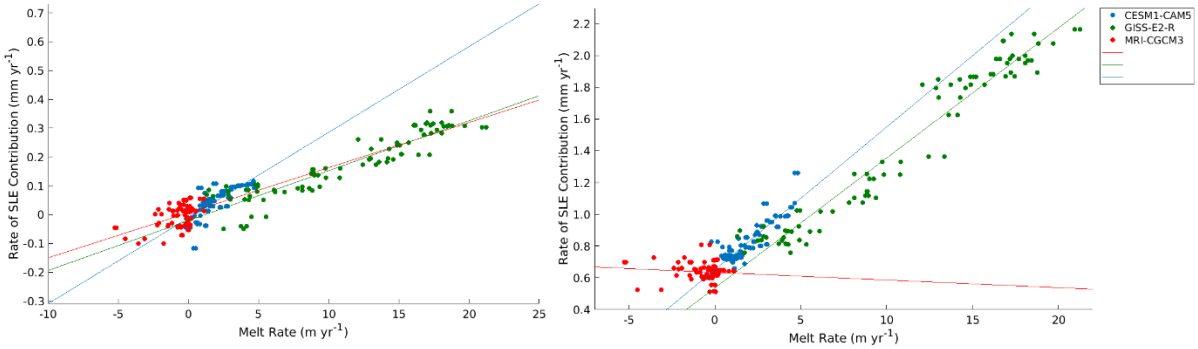

13A: *Rate of SLE contribution for each three CMIP5 models against the projected melt rate forcing applied from 2020-2100 using the H (left) and L (right) parameter sets.*